UNIVERSITÉ DE STRASBOURG

École Doctorale
des Sciences de la Vie
et de la Santé
STRASBOURG

ÉCOLE DOCTORALE DES SCIENCES DE LA VIE ET DE LA SANTE

Inserm U1114

THÈSE présentée par:

Tiago Manuel ROCHA FELIX

soutenue le: **20 juillet 2016**

pour obtenir le grade de: **Docteur de l'Université de Strasbourg**

Discipline/ Spécialité: Neurosciences

Inhibition Périsomatique dans les Oscillations Gamma et dans l'Apprentissage Auditif

THÈSE dirigée par :

M. Dr. PINAULT Didier	Prof. Dr., Université de Strasbourg
Mme BARTOS Marlene	Prof. Dr., Albert-Ludwigs-Universität Freiburg

RAPPORTEURS :

Mme DIESTER Ilka	Prof. Dr., Albert-Ludwigs-Universität Freiburg
M. EGERT Ulrich	Prof. Dr., Albert-Ludwigs-Universität Freiburg

AUTRES MEMBRES DU JURY :

M. ISOPE Philippe	Dr., Université de Strasbourg
M. AERTSEN Ad	Prof. Dr., Albert-Ludwigs-Universität Freiburg
M. LÜTHI Andreas	Prof. Dr., Universität Basel

1 Summary

The interplay between inhibition and excitation is a ubiquitous phenomenon in the nervous system that is thought to form the basis for complex cognitive functions. In the cortex, a subset of interneurons provides fast and strong inhibition to the perisomatic region of pyramidal neurons, thus greatly influencing the action potential output of these excitatory cells. Convergent evidence has attributed to perisoma-inhibiting interneurons (PIIs) a key role in the synchronization of neuronal activity and in the generation of high-frequency rhythms, namely gamma oscillations. However, no investigation has yet conclusively demonstrated that PIIs are necessary for gamma oscillations to occur, particularly in response to sensory stimuli. In this study, I optogenetically probe the effect of reduced perisomatic inhibition on gamma oscillations in the auditory cortex of freely behaving mice. Subsequently, I investigate the impact of diminished perisomatic inhibition on associative learning and on the conditioned neuronal responses to auditory stimuli. Contrary to expectations, I do not observe a reduction in gamma oscillations during inhibition of PIIs, but rather a strong increase in the amplitude of both ongoing and auditory-induced oscillations. The amplification of the auditory-evoked potential N15, together with the absence of an increase in synchrony between the cortex and the thalamus, suggests that decreased perisomatic inhibition disinhibits the auditory cortex and promotes the intracortical generation of gamma oscillations. In a different experiment, I show that inhibition of PIIs impairs learning and produces an experience-related reduction in the auditory-evoked potential N15. Lastly, I find that lowering the optogenetic inhibition delivered to PIIs and retraining mice enhances auditory-induced gamma oscillations. My findings confirm the contribution of perisomatic inhibition to cognition. In contrast, my results offer a radically new perspective on the participation of perisomatic inhibition in gamma oscillations and invite to consider alternative generators of fast rhythms.

2 Table of contents

3 Table of figures

4 Introduction

Neocortical inhibitory neurons constitute a remarkably heterogeneous cell population with disparate morphological, electrophysiological and molecular properties[1–4] (Fig. 4.1A). They use γ-amino butyric acid (GABA) as a neurotransmitter and target primarily local neurons[1], hence being commonly referred to as GABAergic interneurons[3,4]. Although inhibitory neurons represent a minor fraction of the total neuronal population in the neocortex[5] (≈ 20%), they exert a strong influence over target neurons[6]. Moreover, inhibitory neurons assume a pivotal role in keeping normal brain function, as inferred from the detrimental effects that occluded inhibition has on neuronal activity[7], sensory processing[8] and behaviour[9]. Neocortical excitatory neurons use glutamate as a transmitter and consist predominantly of pyramidal cells. Albeit excitatory neurons compose the majority of neocortical neurons (≈ 80%), their comparatively standard properties sharply contrast with the exuberant variety of features displayed by inhibitory neurons[2]. The higher complexity of the cellular substrate of inhibition allows for additional functional specialization and for controlling different features of the activity of pyramidal cells. Inhibitory interneurons show highly-specialized axonal arborizations with the ability to target specific compartments of pyramidal cells, thus acting separately on the input and output of the latter[1,2]. Importantly, the intricate connectivity among interneurons[10] mediates the bidirectional control of pyramidal cells through a number of mechanisms (Fig. 4.1B), namely inhibition and disinhibition[11–14]. Convergent experimental evidence is beginning to relate these connectivity-based mechanisms to particular aspects of sensory processing[15–17] and behaviour[12,18,19] (Fig. 4.1C).

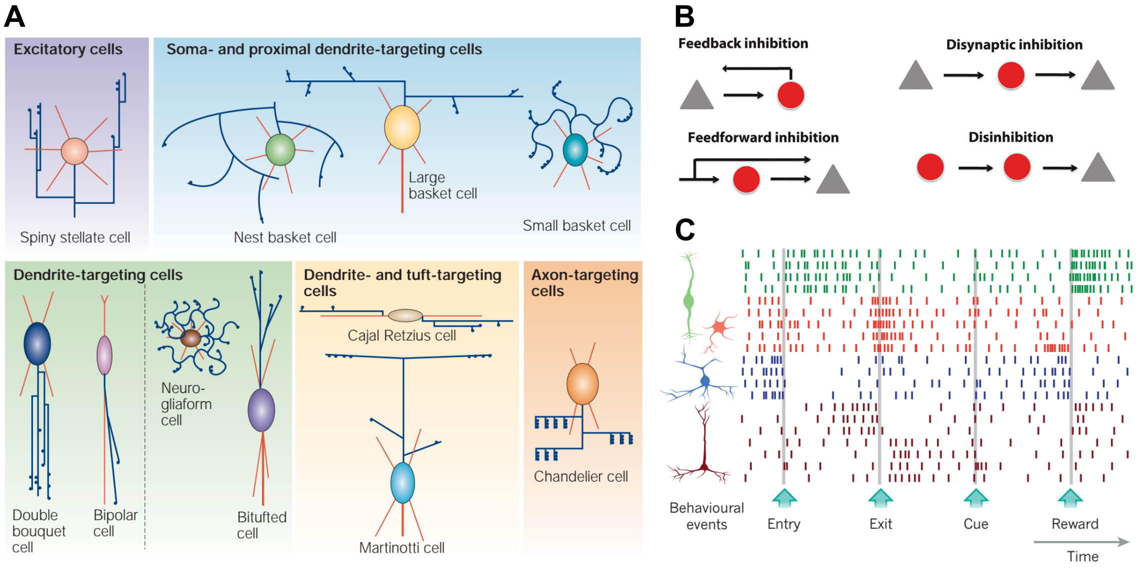

Figure 4.1 | Morphological and functional diversity of neocortical inhibitory neurons. A | Schematic representation of the neocortical interneuron types depicting their markedly diverse somatic, dendritic and axonal morphologies. The axonal arborisation allows to categorize them according to the specific domains of pyramidal cells they target. **B** | Schema of the motifs of neuronal connectivity involving inhibitory interneurons. These connectivity configurations allow inhibitory neurons to assume different functions. **C** | Schematic illustration of the firing of different neuron types relatively to behavioural events. Inhibitory interneurons can be sorted based on the correlation between their firing rates and behavioural events. Panel **A** adapted, with permission, from REF. 2 © (2004) Nature Publishing Group. Panel **B** adapted, with permission, from REF. 20 © (2013) SAGE Publications. Panel **C** adapted, with permission, from REF. 19 © (2014) Nature Publishing Group.

4.1 Perisoma-inhibiting interneurons of the neocortex

A major subset of inhibitory interneurons targets specifically the perisomatic domain of pyramidal cells. These neurons fall into two main morphological categories: basket cells and chandelier cells[2] (Fig. 4.2A). Basket cells comprise more than half of the GABAergic interneurons and target both the soma and the proximal part of the apical dendrites of pyramidal cells. Chandelier cells, also referred to as axo-axonic cells, consist of a small population of GABAergic interneurons that targets specifically the axon initial segment of pyramidal cells. The fact that the output synapses of perisoma inhibiting interneurons (PIIs) are located precisely at, or adjacent to, the region of action potential initiation, makes them particularly well suited to control the action potential output of pyramidal cells[1,2].

PIIs can modulate firing through shunting inhibition[21], which depends on the ionotropic $GABA_A$ receptor and results from a reversal potential of $GABA_A$ receptor-mediated synaptic currents that lies between the resting potential and action potential threshold[22]. Shunting perisomatic inhibition acts on the gain of pyramidal cells by increasing membrane conductance, and consequently by reducing the ratio between the excitatory input to these neurons and the ensuing firing output[23–25]. As a result of this divisive effect on excitatory input, perisomatic inhibition constitutes a biophysical mechanism that enables the brain to perform an arithmetic operation[24] (Fig. 4.2B, top graph). This operation forms the basis for a canonical neural computation—divisive normalization—which confers to neurons the ability to adapt their responses to excitatory input according to the ratio between that input and the summed activity of a set of neurons[25]. Normalization is hypothesized to serve several functions such as maximization of sensitivity to inputs[25].

An additional canonical neural computation modulates responses through a thresholding or ‘iceberg’ effect[26] and could rely on subtractive perisomatic inhibition[27] (Fig. 4.2B, bottom graph). In the auditory cortex this effect sharpens the frequency tuning width of receptive fields by reducing neurons activity and therefore narrowing the bandwidth of the excitatory input that is able to elicit a response above spike threshold[28–30] (Fig. 4.2C). A consequence of the ‘iceberg’ effect is that output suprathreshold responses are more sharply tuned than the underlying subthreshold deflections in the membrane potential, potentially improving the signal-to-noise ratio of population responses to auditory stimuli[31]. Another main, disparate role of PIIs is that of controlling the timing of firing. By providing fast, strong and reliable inhibition[18,32–34] PIIs can accurately narrow the input integration window, thus enhancing temporal precision of input coincidence detection[35] and synchronizing neuronal activity (see Sect. 4.3).

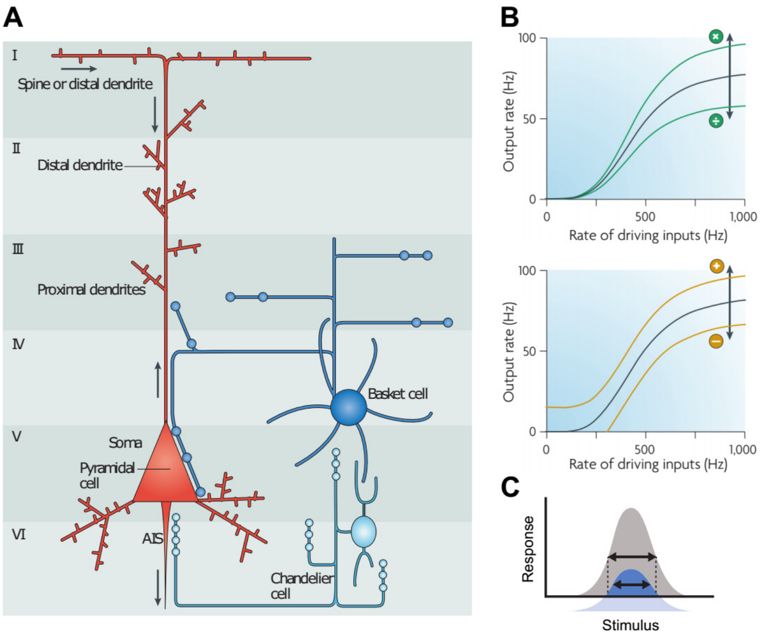

Figure 4.2 | Perisoma inhibiting interneurons (PIIs) control the output of pyramidal cells. A | Schematic illustration of the two main types of PIIs and the location of their synapses onto pyramidal cells. **B** | Schematic transformations of the input–output relationship of pyramidal cells by PIIs. These effects on the response to inputs underlie the arithmetic operations of division and subtraction (top and bottom graphs respectively). **C** | Schema of the tuning curve of a pyramidal cell with and without subtractive inhibition (blue and grey respectively). The downward shift acted by inhibition reduces the extent of stimulus able to elicit a response above the action potential threshold (*x*-axis). This outcome is referred to as 'iceberg' effect and allows PIIs to sharpen tuning of receptive fields. Panel **A** adapted, with permission, from REF. 36 © (2007) Nature Publishing Group. Panel **B** adapted, with permission, from REF. 24 © (2010) Nature Publishing Group. Panel **C** adapted, with permission, from REF. 27 © (2014) Nature Publishing Group.

4.2 Parvalbumin (PV) as a marker for perisoma-inhibiting interneurons

In the previous section, PIIs were described in terms of the anatomical specificity of their synapses. As indicated, these highly-specialized axonal arborizations enable a type of inhibition that affects the perisomatic region of pyramidal cells, and consequently directly modulates the output or response of these neurons. These considerations exclusively relate the morphology and function of PIIs, which are characteristics that can be substantially difficult to systematically and extensively assess[4] as compared to the molecular profile. Therefore, molecular markers are important research tools being recurrently used to define neocortical GABAergic interneuron types[1–4,37]. Moreover, a myriad of increasingly sophisticated genetic tools, most notably optogenetic tools, that rely on well-defined molecular alterations to living beings are commonly used in life sciences[38,39]. The principal marker of PIIs is the Ca^{2+}-binding protein parvalbumin (PV), which constitutes a specific marker of all PII morphological types and is expressed in at least half of neocortical basket cells[2]. Cortical PV-expressing (PV^{+}) cells originate in the medial ganglionic eminence[19] and compose a major portion of GABAergic interneurons[10,37] (36–40% in mice; Fig. 4.3A).

PV^{+} interneurons target mainly one another (Fig. 4.3B,C) and pyramidal cells[10,20] (but see REF. 40), whereas other molecular interneuron types send important inputs to PV^{+} interneurons[10–

[12,20,40] (Fig. 4.3C). Interneurons targeting PV$^+$-cells mediate disinhibition of pyramidal cells and are characterized by a soma sitting on layer I[11] or by the expression of neuropeptides, namely somatostatin[10,20,40] (SOM) or the vasoactive intestinal peptide[12] (VIP). These interneurons and PV$^+$ cells constitute largely non-overlapping interneuron types[2,37]. Similarly, their extensive networks of electrical synapses are restricted to cells of the same type[40].

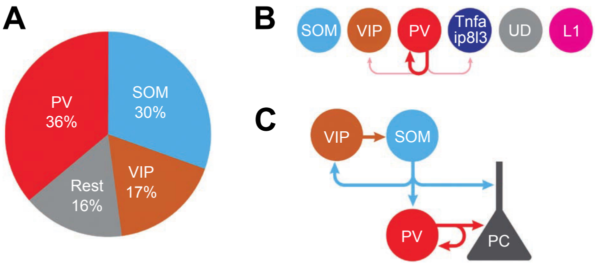

Figure 4.3 | Parvalbumin-expressing (PV$^+$) interneuron in perspective to other molecular types. A | Proportions of the main interneuron types indicate that PV$^+$ cells are the largest interneuron type. **B** | PV$^+$ cells show extensive mutual connections but only poorly target other interneurons. **C** | In contrast, other interneurons directly inhibit PV$^+$ cells. Adapted, with permission, from REF. 10 © (2013) Nature Publishing Group.

The functional relevance of parvalbumin remains a matter of debate. Evidence collected in PV knockout (PV–/–) mice shows that, in response to paired-pulse stimulation, PV can counteract facilitation and produce depression[41]. Accordingly, by acting as an endogenous Ca^{2+} buffer, PV can serve as an anti-facilitation factor in short-term plasticity. Such effect of PV has been shown to reduce repetitive release of GABA, thus impacting negatively on the amplitude of fast oscillations[42]. Computational modelling experiments have revealed that PV could regulate synaptic dynamics by shunting the local saturation of endogenous fixed buffers[43]. Taken together, these findings could explain why PV$^+$ cells have such distinct synaptic properties from those of other GABAergic interneurons types, i.e. why excitatory synapses onto PV$^+$ cells and other interneurons are depressing and facilitating respectively[44–46], and why inhibitory output synapses from PV$^+$ cells and other interneurons are strongly depressing and weakly facilitating or depressing respectively[44,45].

4.3 Involvement of perisomatic inhibition in the generation of gamma oscillations

Several signalling properties of PIIs set them as the foremost candidate for the synchronization of neuronal activity[33,47–50] and for the generation of fast rhythmic activity (30–80 Hz) termed gamma oscillations[49–51]. First, PIIs can be recruited and effect inhibition in submillisecond timescales[34]. The fact that PIIs receive rapid excitation[52] and provide fast, strong and reliable inhibition[18,32–34] makes them particularly apt for controlling the timing of action potential firing both in pyramidal cells and other PIIs. Furthermore, PIIs generally display the ability to continuously discharge action potentials at high frequencies (> 150 Hz at 34 °C[34]) during depolarizing-current injection, as defined by the considerable overlap between the populations of PV$^+$ and fast-spiking interneurons[2,53] (but see Fig. 2j of REF. 54). A beneficial consequence of the electrophysiological signature of PIIs is that the fast-spiking action potential phenotype is associated to a brief action potential[55], which can be used to identify putative interneurons in extracellular in vivo recordings[11]. Finally, neurons displaying this fast-spiking action potential phenotype[55], in response to dynamic input currents, show high resonance specifically in the gamma-band frequency range[56,57]. The foregoing considerations, together with the abundance of PIIs (see Sect. 4.1) and the high divergence of their output to pyramidal cells[58,59], have led to the so-called fast-spiking-gamma hypothesis, which attributes to fast-spiking PV$^+$ PIIs a critical role in the generation of gamma oscillations[60].

Correlative evidence is consistent with the contribution of PIIs to gamma oscillations. Gamma-band activity is accompanied by the spatial overlap between the perisomatic region of principal cells and alternating current sources and sinks[61–63]. Importantly, PIIs are very active during gamma activity and, contrary to other neurons, not only fire action potentials precisely phase-locked to the gamma rhythm but also the frequency rate lies exactly in the gamma range[61–65]. Specific causal evidence in favour of the fast-spiking-gamma hypothesis has been obtained only with the advent of optogenetics. Optogenetic excitation of neocortical PV$^+$ cells reveals that these interneurons are sufficient to entrain oscillations restricted to the gamma frequency range[60,66–68]. Moreover, when systematically probing oscillation induction at several different frequencies[60,67] and amplitudes[60] of optogenetic stimulation, the gamma rhythm manifests itself a resonant property of the neural circuit. Interestingly, enabling feedback perisomatic inhibition by focal stimulation of PV$^+$ interneurons in response to pyramidal cell firing entrains the gamma rhythm in the firing activity[66]. A dissimilar type of causal evidence indicates that a reduction in perisomatic inhibition, resulting from the optogenetic inhibition of PV$^+$ cells, leads to a decrease in gamma power[66].

Three distinct mechanisms support the generation gamma oscillations[51]. First, rhythmic activity can be simply conveyed via feedforward projections[69,70]. Second, reciprocally connected networks of pyramidal neurons and GABAergic interneurons could entrain the gamma rhythm via the pyramidal-interneuron gamma (PING) mechanism[49,51,71] (Fig. 4.4, left schema). Third, networks of mutually connected GABAergic interneurons could impose the gamma rhythm on pyramidal cells via the interneuron gamma (ING) mechanism[49,51,71] (Fig. 4.4, schema on the right). The ING model is motivated by the extensive interconnectivity between GABAergic interneurons[10], particularly among PIIs[10,33,48,49,72], and network models implementing such connectivity can robustly generate gamma oscillations via either PING[73] or ING[33,74]. A fundamental difference between the PING and ING lies in the degree of dependence on fast excitation to activate interneurons—whereas ING requires no excitation, PING is extensively reliant on it—and therefore transition between the two mechanism can at least conceptually be implemented by regulating the excitation of pyramidal cells[49,71]. The accuracy of these models is still debated and even the aforementioned experiments where the involvement of PII has been causally validated[60,66–68] cannot conclusively differentiate PING from ING (as reviewed in REF. 51).

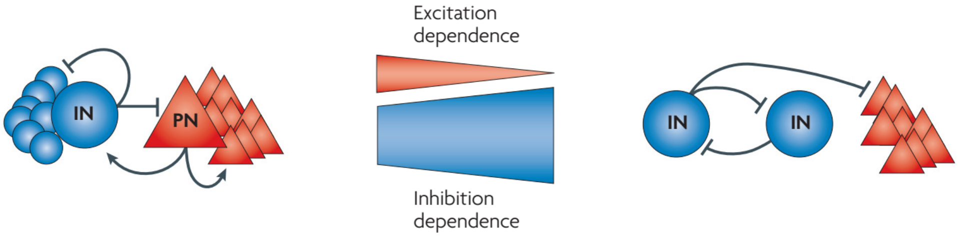

Figure 4.4 | Mechanisms of interneuron-dependent gamma oscillations. Schemas of the pyramidal-interneuron gamma (PING; left) and interneuron gamma (ING; right) models. These mechanisms show different levels of dependence on excitation and inhibition (centre). Adapted, with permission, from REF. 49 © (2007) Nature Publishing Group.

4.4 Participation of perisomatic inhibition and gamma oscillations in cognition

Neural oscillations have been proposed to participate in memory [75,76] and information processing[77,78] by coordinating the formation of ensembles of synchronously active neurons and the sequence of activation of different ensembles. A key notion related to such coordination of neuronal activity is that features of both sensory and cognitive information are encoded, decoded and processed according to the temporal order of cell activation. Conceptually, this temporal code can be implemented via a reference, rhythmic inhibitory signal that restricts neuron discharge to periodic windows of opportunity. Two mechanisms have been proposed to describe the interplay between rhythmic inhibition and particular signalling properties of neuronal assemblies[79]. One of such mechanisms is the communication through coherence hypothesis[80], which attributes exclusively to coherently oscillating cell ensembles the ability to communicate and thus to contribute to information processing. As stated by this hypothesis, the phase of oscillations in the excitability of pyramidal cells dictates which cell ensembles, at a given time, are most excitable and consequently expected to fire together (Fig. 4.5A). The second mechanism relies on phase coding, i.e. on information processing according to the timing of spikes in relation to the phase of the oscillation. Phase coding can be implemented by networks of GABAergic interneurons oscillating within the gamma-band range[78,81]. This coding strategy enables information processing within a gamma cycle based on a simple rule: the higher the intensity of a stimulus, the earlier a neuron will be able to overcome the inhibition peak and generate a response (Fig. 4.5B).

Evidence gathered in the auditory cortex shows that rhythmic signals are hierarchically organized, as observed in the cross-frequency coupling between different frequency bands: the phase of the delta rhythm modulates theta power and the phase of the theta rhythm modulates gamma power[82]. Invasive recordings collected in humans have allowed to relate this oscillatory hierarchy with the cognitive hierarchy by revealing that gamma and slow rhythms privilege respectively bottom-up and top-down information propagation[83]. Theta-gamma coupling is a particularly well studied type of coupling[84,85] that is thought to provide a range of input integration windows to support information processing at multiple temporal[86] and spatial[84] scales. Experiments in freely moving knockout mice lacking synaptic inhibition specifically in PV^+ interneurons revealed that

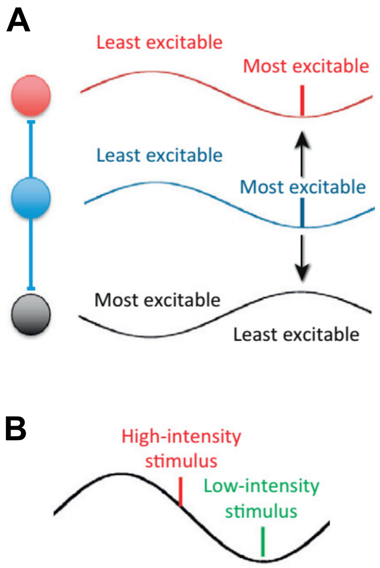

Figure 4.5 | Mechanisms of temporal coding by rhythmic inhibition. **A** | Schema depicting the communication through coherence hypothesis. Firing of blue neuron can only lead to firing of red, but not black neuron. **B** | Schema of phase coding of two stimuli of different intensities within a wave cycle. Adapted, with permis-sion, from REF. 79 © (2015) Elsevier.

theta-gamma coupling requires fast inhibition onto PIIs[87]. Pioneering work combining optogenetics with information theory has observed that perisomatic inhibition to pyramidal cells not only increases gamma-band power of action potential firing but also improves the efficiency of rate coding[66]. Moreover, the same study showed that gamma oscillations improve mutual information of the input to pyramidal cells relative to its output and also reduce noise in these cells.

Perisomatic inhibition contributes to sensory processing via feedforward inhibition of pyramidal cells. Experimental evidence collected in the auditory[17], visual[88] and somatosensory[46] cortices of transgenic mice shows that sensory or thalamic stimulation evokes activation of PV$^+$ interneurons at latencies comparable to or smaller than those of pyramidal cells[17,88], and much shorter than those of other interneurons[17,46]. Additional evidence indicates that optogenetic activation of PV$^+$ cells increases functional connectivity of vertical thalamorecipient and intracolumnar circuits but not of horizontal intralaminar circuits, thus suggesting that perisomatic inhibition favours the contribution of bottom-up sensory inputs to perception over top-down feedback inputs[31]. Optogenetic in vivo experiments in the neocortex of mice have further elucidated the role of PII-mediated gamma oscillations in sensory processing[60,68]. In these experiments the gamma rhythm was entrained by optogenetically activating PV$^+$ cells and sensory stimulation was provided at different phases of the gamma cycle (Fig. 4.6A). The findings from these studies reveal that gamma phase regulates sensory processing and that, by delivering the sensory stimulus precisely 12.5 ms after the optogenetic pulse, spike precision (Fig. 4.6B) and behavioural performance can be improved.

Gamma oscillations are disrupted in mental disorders[89], most notably in schizophrenia[90–94]. Aberrant gamma activity is present both in knockout mice lacking the N-methyl-D-aspartate (NMDA) receptor subunit NR1 specifically in PV$^+$ cells[67,95] and following the application of NMDA receptor antagonist[96–98]. Extensive experimental evidence has demonstrated that the application of NMDA receptor antagonists not only induces schizophrenia-related neuronal states in the cortex[99–104], but also that these states are characterized by hypofunction of inhibitory interneurons[105,106], particularly PIIs[107]. In contrast, an enhancement of cognition (fluid intelligence) has been observed after providing gamma-modulated rhythmic stimulation to healthy subjects via transcranial alternating current stimulation (tACS)[108].

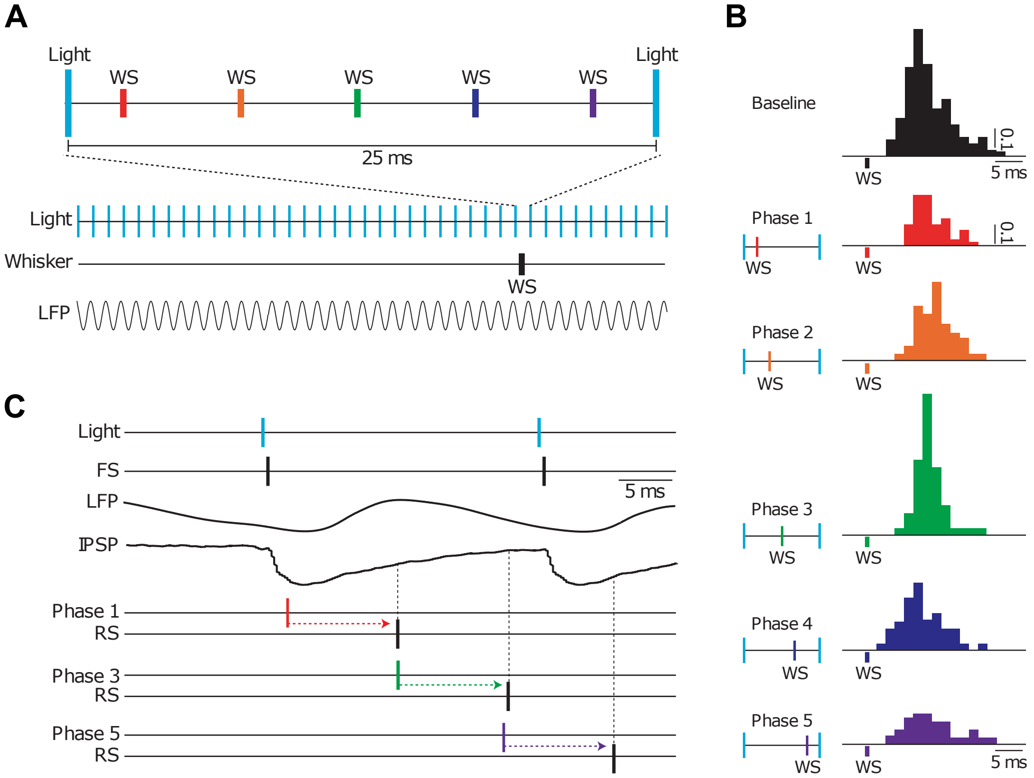

Figure 4.6 | **Perisomatic inhibition and gamma oscillations regulate sensory responses. A** | Diagram of the experimental protocol. Fast-spiking (FS) PV⁺ were activated at 40 Hz by light and a whisker stimulus (WS) was delivered at one of five phases of the 40-Hz cycle. **B** | Spike responses of a regular spiking (RS) neuron to the WS. **C** | The phase that resulted in the highest firing precision corresponded to the one that elicited spiking in the RS neuron during the trough of inhibition. Adapted, with permission, from REF. 60 © (2009) Nature Publishing Group.

4.5 Aims of this research project

The involvement of perisomatic inhibition in the generation gamma oscillations is supported by several anatomical and signalling properties of PIIs (see Sect. 4.3). Furthermore, a plentiful supply of evidence from numerous studies has demonstrated that gamma oscillations are tightly coupled, both spatially and temporally, to the activity of PIIs. The advent of optogenetics permitted stablishing a specific causal relationship between perisomatic inhibition and gamma oscillations by showing that periodic recruitment of PIIs is sufficient to amplify the gamma rhythm. However, despite many scientific attempts to assert the necessity of perisomatic inhibition for this fast rhythm, most notably by optogenetically inhibiting PV⁺ interneurons[66], it remains unclear whether perisomatic inhibition is indeed required for neocortical gamma oscillations[109], particularly those induced in response to sensory stimuli. Furthermore, notwithstanding copious evidence for the participation of perisomatic inhibition and gamma oscillations in sensory processing (see Sect. 4.4), there little evidence for the contribution of perisomatic inhibition and fast rhythms to learning of associations between sensory stimuli. Here, I present local field potential (LFP) recordings collected in the auditory cortex of freely behaving mice. Optogenetic inhibition of PV⁺ cells was effected in the auditory cortex of these mice to uncover the effects of perisomatic inhibition both on spontaneous and auditory-induced gamma oscillations. Finally, the effects of perisomatic inhibition on auditory fear conditioning were assessed by inhibiting PV^+ cells specifically during simultaneous delivery of acoustic and noxious stimulus. This study will hopefully contribute to our understanding of the role of perisomatic inhibition in the generation of gamma oscillations and the contribution of these neural phenomena to auditory learning.

5 Results

In the auditory cortex (ACx), alterations in the gamma rhythm constitute a hallmark of mental disorders[89] such as schizophrenia[92–94]. Similarly, dysfunctional perisomatic inhibition in the neocortex is also associated to schizophrenia[91,110–112]. While the functional relevance of perisomatic inhibition and gamma oscillations is further supported by their contribution to network synchronization[33,47–50] and sensory processing[60,68,113–117] respectively, the cellular substrate of fast oscillatory activity and sensory learning remains elusive. The present work provides direct insight into the role of perisomatic inhibition in the generation of gamma rhythms and in auditory learning. I here report on 3 key sets of data consisting of (a) electrophysiological recordings in the ACx of naive mice, (b) behavioural measurements in these mice upon fear conditioning and (c) electrophysiological recordings taken during those same behavioural measurements. Accordingly, this chapter is divided in 3 main parts: (a) first, in Sect. 5.1, I discuss the fast-spiking-gamma hypothesis (see Sect. 4.3) and I address the question of whether gamma activity requires perisomatic inhibition; (b) second, in Sect. 5.2, I elaborate on the control that perisomatic inhibition exerts on associative learning; I ask whether the strength of an association between stimuli can be improved by modulating perisomatic inhibition and enhancing the gamma rhythm; (c) finally, in Sect. 5.3, I relate the goals of the 2 previous sections by probing learning-induced alterations in gamma activity.

To address the foregoing aims, transgenic PV-Cre mice were infected bilaterally in the ACx with a Cre-dependent recombinant adeno-associated virus (rAAV) to express the light-gated chloride-pump enhanced halorhodopsin[118] (eNpHR2.0) specifically in PV$^+$ cells[66] (Fig. 5.1A). These mice received optogenetic stimulation, at the virus injection sites, through an optrode and an optical fibre implanted in the left and right auditory cortices respectively (Fig. 5.1C–F). The optrode, composed of an optical fibre and a tetrode, not only served to deliver light to inhibit PV$^+$ cells, but also allowed recording the LFP signal from the optogenetically manipulated neuronal population[119] (Fig. 5.1E). To avoid undesired excitation of PV$^+$ cells upon eNpHR photoactivation[120,121], reported electrophysiological effects pertain to data recorded either during optogenetic stimulation or in a different experimental session, but never directly after optogenetic stimulation. Electrophysiological recordings targeted layers IV and V (Fig. 5.1B) owing to the easiness of post-hoc identifying the ACx through inspection of the conspicuous potentials evoked by acoustic stimulation[122–124] in these layers.

Experiments were performed in a sound-attenuated semi-anechoic environment (Fig. 7.1) and acoustic stimulation was delivered free-field to mice. Acoustic stimuli consisted of broadband sounds (5–80 kHz bandwidth), covering most of the hearing range of mice[125–127]. This type of acoustic stimulus was selected over narrow-band stimuli (e.g. tones) not only for its ability to elicit physiological responses more consistently than narrow-band stimuli[128], but also because it can initiate larger cortical responses at suprathreshold sound levels[129,130] (i.e. well above the hearing threshold). Therefore, using broadband sounds, one can effectively activate the ACx with less dependence on the particular location of the recording electrode relatively to the tonotopic map[127].

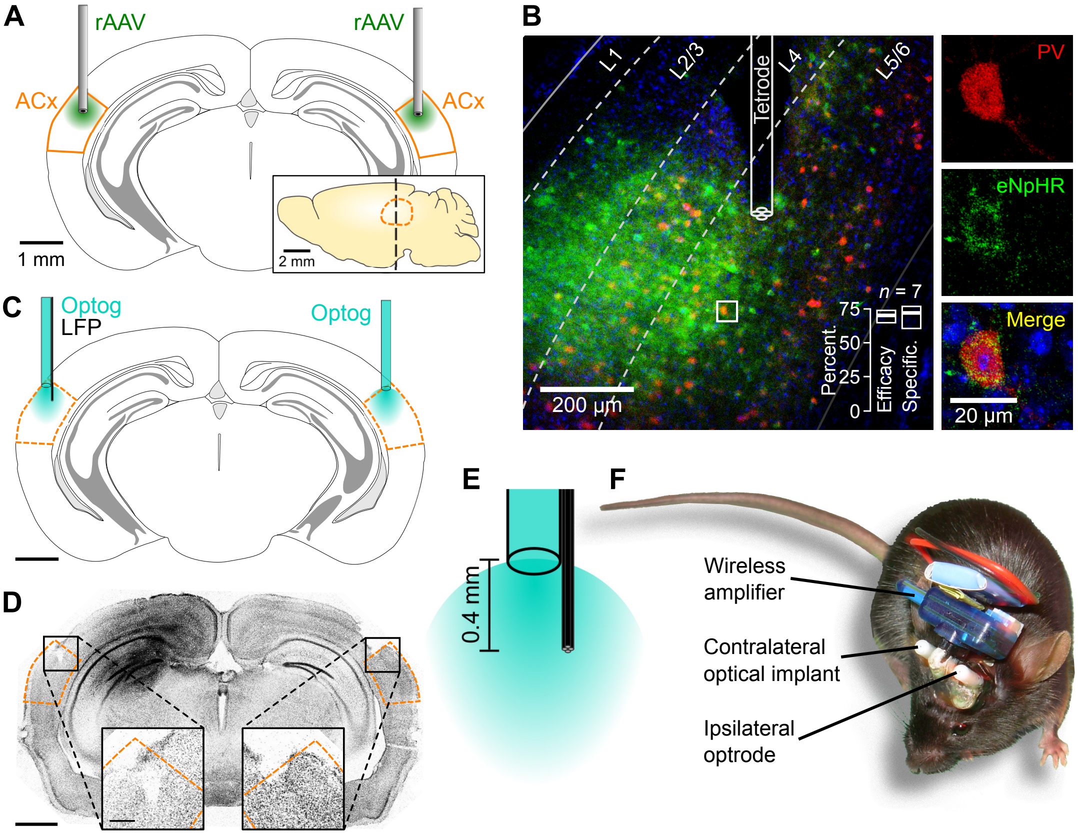

Figure 5.1 | Expression of recombinant viruses (rAAVs) for optogenetic manipulation of the ACx. **A** | Bilateral stereotactic injection of rAAVs (green) for expression of enhanced halorhodopsin (eNpHR) or green fluorescent protein (GFP) in parvalbumin-expressing (PV$^+$) cells in ACx (orange) of mice. Inset | Sagittal view of the ACx (orange). **B** | Epifluorescent image of the profile of eNpHR (green) and PV (red) expression across layers (dashed lines) of the ACx ipsilateral to the implanted tetrode. Layering determined with DAPI staining (blue). Right | Confocal images show expression of eNpHR in PV$^+$ cells. Inset | Virus transduction efficacy and specificity (n = 7) as calculated from the detected degree of co-expression of eNpHR and PV. Values are median and interquartile range (IQR). Statistical analysis in text. **C** | Light (blue) delivery through optical fibres implanted above the ACx. Local field potentials (LFP) were recorded with a tetrode, implanted into the left ACx, attached to the optical fibre (together composing the optrode). **D** | Reconstruction of DAPI-stained coronal slice shows that implants have correctly targeted the ACx. **E** | The ≈ 0.4-mm offset between the tips of the optical fibre and tetrode improves illumination of recorded neuronal population and reduces photovoltaic artefacts. **F** | Mouse, after surgery, connected to the wireless amplifier. Implants were fixed with dental cement that was purposely darkened to contain light. Scale bars: **C** and **D** 1 mm; **D** inset 200 µm.

5.1 PV$^+$ cells reduce gamma oscillations by reducing intracortical excitation

PV$^+$ interneurons have been hypothesized to directly generate the gamma rhythm (see Sect. 4.3). In vivo experimental verifications of such hypothesis have attributed causative power to these interneurons in the emergence of gamma activity in the prefrontal[66] and somatosensory[60,67,68] cortices. Furthermore, one of these scientific enquiries, employing similar tools to those here used (same mouse line and viral vector), has shown that inhibition of these cells leads to a reduction in gamma oscillations[66]. However, neither of them has investigated the effects of PV$^+$-cell inactivation on sensory-induced gamma activity, thus conclusively demonstrating the necessity of these cells to the generation of gamma activity.

I recorded the LFP in the ACx of freely moving mice during acoustic stimulation and examined the impact that suppression of perisomatic inhibition has on gamma activity (Fig. 5.2A). Removal of perisomatic inhibition was achieved by optogenetically inhibiting PV^+ interneurons at 2 different intensities: strong inhibition was realized through stimulation with green light (561-nm wavelength), close to the peak of the action spectrum of eNpHR (≈ 580 nm), and weak inhibition was delivered by stimulating with blue light (473-nm wavelength), taking advantage of the 2.5–6-fold lower activation of eNpHR at this wavelength[119,131–133]. Blue-light stimulation served as an internal control for heating of brain tissue by light absorption and for possible visual stimulation of the mouse caused by optogenetics (albeit most light was contained by the head implant; see mitigation measure in Sect. 7.2.3.b). Such control benefits from the virtually identical absorption of blue light, compared to green light, by the only 2 mouse retinal pigments excitable at these wavelengths[134–137] (i.e. M-opsin in cone cells and rhodopsin in rod cells). Equalling the intensity of blue light to that of green light (see Sect. 7.2.6.c) should further decline to 3–8 fold the activation of eNpHR by blue light compared to green light, as a consequence of the lower photon flux of blue light[138] (as described by the Planck–Einstein relation).

5.1.1 Auditory-induced gamma oscillations are decreased by PV^+ cells

To demonstrate the interplay between auditory processing and gamma oscillations, I started by replicating the previously reported induction of long-lasting gamma activity in response to short (50–100 ms) acoustic stimulation[124,139]. I presented a sound (Fig. 5.2B) to mice and observed the emergence of high-frequency oscillatory activity that considerably outlasted the stimulus (by up to 1 s; Fig. 5.2C–F, condition *acou*). This auditory response was described by a significant increase in gamma-band power compared to baseline (1.66 ± 1.06 dB, $n = 8$; one-sample Student's t-test ascribed a significant difference to 0 dB, $t_{(7)} = 4.44$, $p = 0.009$ after Šidák correction, $m = 3$, two-sided; details of statistical analysis in Sect. 7.2.10.g). In line with previous findings[123,124,139], gamma oscillations were not phase-locked to stimulus onset but rather stochastically emerged in the form of bouts of variable phase and duration (Fig. 5.2C). As a result, throughout this work, I will refer to this activity as *induced gamma* (e.g. auditory-induced gamma) to distinguish it from *evoked gamma*, the latter term referring to stimulus-locked responses falling in the gamma-band frequency range[140–143] (not assessed here).

I next focused on the modulation of auditory-induced gamma activity by perisomatic inhibition. Accordingly, I optogenetically inhibited PV^+ interneurons with green light during acoustic stimulation (condition *acou + optog⁺*). The current hypothesis attributes a key role to PV^+ cells in the generation of fast brain rhythms, thus predicting the reduction of gamma oscillations following removal of inhibition provided by these cells to local neurons. However, to great surprise, despite corroborating a major influence of perisomatic inhibition on gamma amplitude, inhibition of PV^+ cells resulted in the effect opposite to expectations—specifically, it robustly boosted auditory-induced gamma activity (by ≈ 6.4 dB relative to condition acou, $n = 8$; post-hoc pairwise Tukey's test revealed significantly increased normalized gamma power in condition acou + optog^+ compared to acou, $p < 0.001$; Fig. 5.2C–F). Consistent with results previously reported[139,144] for acoustic stimulation alone, auditory-induced gamma power is particularly high from 150–400 ms during reduced PV$^+$-cell inhibition (Fig. 5.2D).

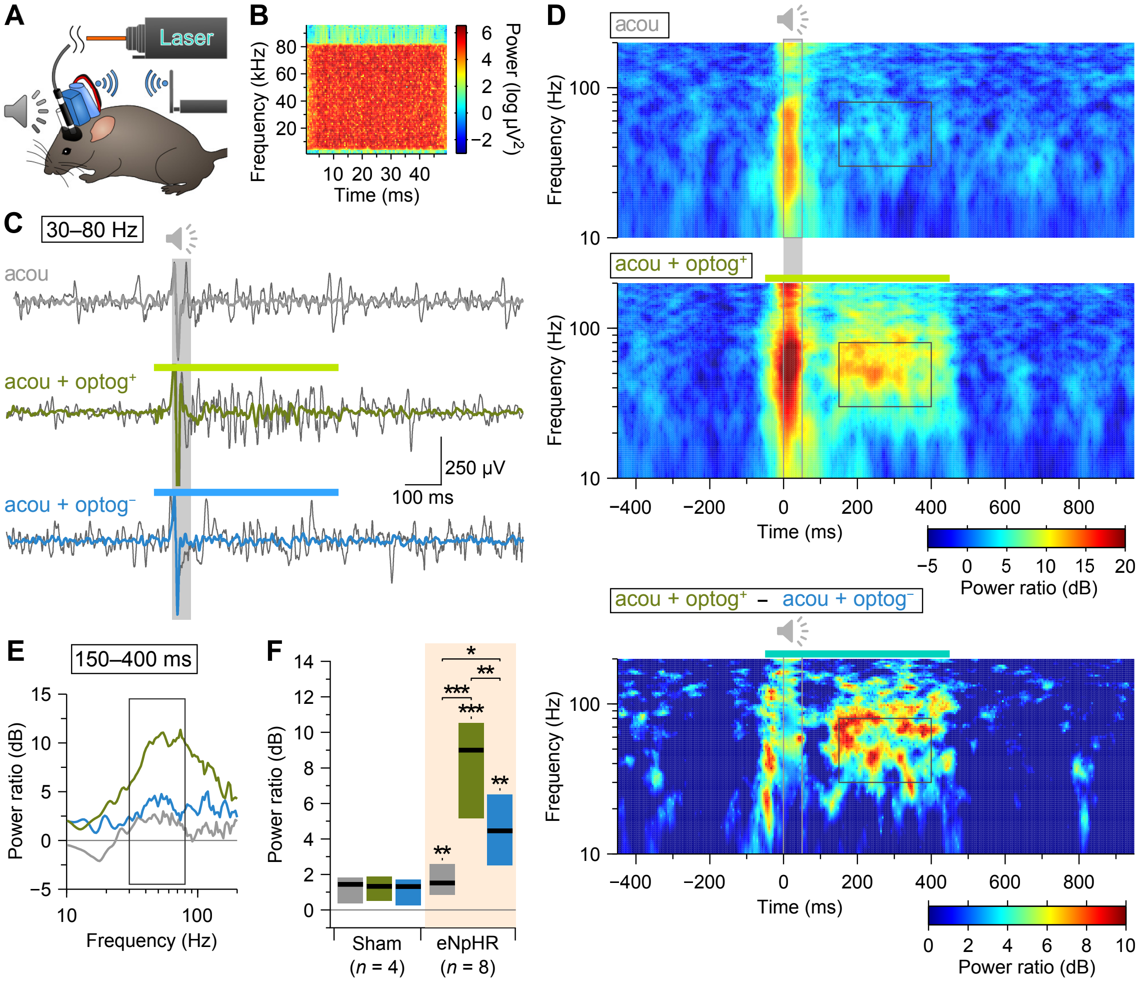

Figure 5.2 | Inhibition of PV$^+$ cells boosts auditory-induced gamma activity. A | LFP responses to acoustic and light stimulation were recorded in the ACx of freely moving mice wearing a wireless amplifier. **B** | Spectrogram of the broadband Gaussian white noise (GWN) used as acoustic stimulus (50 ms, 5–80 kHz). **C** | Representative gamma-band-filtered traces (dark grey) show a small increase in oscillatory activity upon acoustic stimulation alone (acou; grey shade). An increase in auditory-induced gamma activity is also visible during optogenetic inhibition of PV$^+$ cells with blue light and, particularly, with green light (acou + optog$^-$ and acou + optog$^+$ respectively; 500-ms-long horizontal bars). This gamma activity was not phase locked to stimuli as averages from 20 repetitions (thick coloured lines) display no periodic activity (the conspicuous wavelet during sound is an expected artefact of the sizable auditory-evoked potential N15; this wavelet was clipped in condition acou + optog$^+$). **D** | Top | Spectrograms normalized to baseline (–450 to –200 ms) with average responses (20 repetitions) to acoustic stimulation alone and combined acoustic and green-light optogenetic stimulation. Rectangle at the centre specifies the time window used to compute the power spectral density (PSD). Bottom | Differential spectrogram resulting from subtraction of the average non-normalized spectrogram of condition acou + optog$^-$ to the analogous one of condition acou + optog$^+$. **E** | PSDs from 150–400 ms normalized to baseline. Colour code is the same as in **C**. **F** | Baseline-normalized gamma power from 8 eNpHR-expressing mice reveals significantly increased oscillatory activity during inhibition of PV$^+$ interneurons (unbalanced two-way ANOVA showed main effects for both light stimulation, $F_{(2,30)} = 5.80$, $p = 0.007$, and eNpHR expression, $F_{(1,30)} = 23.4$, $p < 0.001$, and detected interaction between factors, $F_{(2,30)} = 5.46$, $p = 0.010$). Colour code is the same as in **C**. Additional statistical results in text. $^*p < 0.05$, $^{**}p < 0.01$, $^{***}p < 0.001$. Values are median and IQR. Traces, spectrograms and PSDs display data from the same mouse as in previous figure.

The effect of PV^+ interneurons on auditory-induced gamma oscillations proved to be specifically explained by the activation of eNpHR in PV^+ cells owing to the significantly greater gamma power during green-light stimulation (by ≈ 3.2 dB, $n = 8$) in comparison to the control optogenetic manipulation with blue light (Fig. 5.2C–F, condition *acou + optog*$^-$; post-hoc pairwise Tukey's test detected a significant difference in normalized gamma power between conditions, $p = 0.006$). This difference is particularly evident in the differential average spectrogram (Fig. 5.2D) of the 2 conditions. The foregoing time window of intensified gamma activity—from 150–400 ms—resurfaces in the difference between these conditions. Notwithstanding the markedly smaller auditory-induced gamma power resulting from the control optogenetic manipulation, it likewise increased gamma activity (by ≈ 3.2 dB, $n = 8$, compared to acou; post-hoc pairwise Tukey's test ascribed significance to this difference, $p = 0.021$).

The specificity of the optogenetic manipulation was further validated in a separate group of PV-Cre mice injected with a Cre-dependent rAAV vector for expression of green fluorescent protein (GFP) in PV^+ cells (Fig. 5.2F, sham conditions). These sham-injected mice did not reveal an effect of light stimulation on auditory-induced gamma activity (post-hoc pairwise Tukey's test attributed no significance to the difference in normalized gamma power between conditions acou and acou + optog$^+$, $p = 0.973$, $n = 4$). Taken together, the within-subject control (i.e. blue-light optogenetic manipulation) and the between-group control (i.e. sham injection) provide strong causal evidence for an effect of inhibition of PV^+ cells on the augmentation of auditory-induced gamma activity.

5.1.2 Ongoing gamma oscillations are likewise diminished by PV$^+$ cells

Similarly to the effect on auditory-induced gamma, perisomatic-inhibition removal also acted on fast oscillations without acoustic stimulation—more precisely, inhibition of PV^+ interneurons with green light resulted in the augmentation of ongoing gamma activity (Fig. 5.3A–D, condition *optog*$^+$; 5.44 ± 3.65 dB, $n = 8$; one-sample Student's *t*-test attributed a significant difference to 0 dB in normalized gamma power, $t_{(7)} = 4.22$, $p = 0.008$ after Šidák correction, $m = 2$, two-sided; supplementary statistical results in the legend of the figure). This outcome indicates that the effect of perisomatic inhibition on the network dynamics is not fundamentally connected to auditory processing, but rather relates to an intrinsic property of the neural circuitry affecting synchronicity among neurons. The data pertaining to this condition confirm the fast (< 10 ms) onset and offset kinetics of eNpHR-mediated inhibition[120,133] (Fig. 5.3A,B). Furthermore, the above-mentioned differential spectrogram (Fig. 5.2D) also displays evidence of optogenetically increased ongoing gamma oscillations (−50–0 ms period of light stimulation preceding sound).

The specificity of green-light stimulation on inhibition of PV^+ cells was validated by 2 controls (Fig. 5.3A–D, conditions *optog*$^-$ *Sham optog*$^+$) analogous to the ones described in the previous section. Control blue-light stimulation resulted in significantly smaller gamma power (by ≈ 2.5 dB, $n = 8$) compared to green-light stimulation (paired Student's *t*-test revealed significantly increased normalized gamma power in condition optog$^+$ compared to optog$^-$, $t_{(7)} = 3.90$, $p = 0.006$, two-sided). Despite leading to a much smaller amplification of ongoing gamma oscillations, the control optogenetic manipulation also produced a significant increase in these oscillations (2.93 ± 2.62

dB, $n = 8$; one-sample Student's t-test indicated a significant difference between optog$^-$ and 0 dB, $t_{(7)} = 3.16$, $p = 0.032$ after Šidák correction, $m = 2$, two-sided). Sham-injected mice did not reveal any effect of light stimulation on ongoing gamma oscillations (one-sample Student's t-test did not indicate a significant difference between optog$^+$ and 0 dB, $t_{(3)} = 3.15$, $p = 0.100$ after Šidák correction, $m = 2$, two-sided).

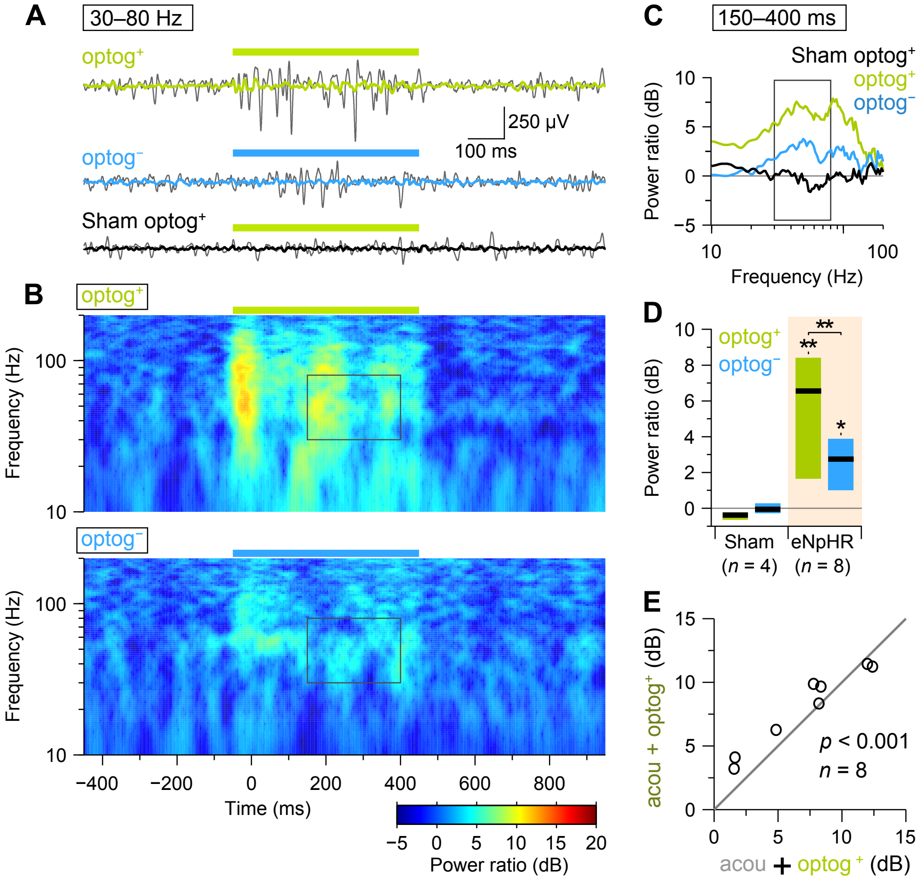

Figure 5.3 | Inhibition of PV$^+$ cells intensifies ongoing gamma activity. A | Representative gamma-band-filtered traces (dark grey) show a drastic increase in oscillatory activity of an eNpHR-expressing mouse during green-light stimulation (optog$^+$; 500-ms-long green bar). In contrast, the same mouse shows only a small increase in ongoing gamma activity during blue-light stimulation (optog$^-$; 500-ms-long blue bar). Green light stimulation has no effect on a sham-injected mouse (Sham optog$^+$). This gamma activity was not phase locked to stimuli as averages from 20 repetitions (thick lines) display no periodic activity. **B** | Spectrograms normalized to baseline (–450 to –200 ms) with average responses (20 repetitions) to green-light and blue-light optogenetic stimulation. Rectangle at the centre specifies the time window used to compute the PSD. **C** | PSDs from 150–400 ms normalized to baseline. **D** | Baseline-normalized gamma power from 8 eNpHR-expressing mice reveals significantly increased oscillatory activity during inhibition of PV$^+$ interneurons (unbalanced two-way ANOVA showed a main effect for eNpHR expression, $F_{(1,20)} = 14.5$, $p < 0.001$, but not for light stimulation, $F_{(1,20)} = 0.82$, $p = 0.375$; no interaction detected between factors, $F_{(1,20)} = 1.62$, $p = 0.217$). Additional statistical results in text. **E** | Additive effect of acoustic and optogenetic stimulation on normalized gamma power. *$p < 0.05$, **$p < 0.01$. Values are median and IQR. Traces, spectrograms and PSDs display data from the same mouse as in previous original figures.

In the light of the capability of the ACx circuitry to induce gamma oscillations in response to both acoustic and optogenetic stimulation, I decided to assess the additivity of the corresponding effects by comparing the combined effect of the 2 types of stimulation with the sum of the individual effects (Fig. 5.3E). In terms of influence over normalized gamma power, the ratio of the joint contribution of acoustic and green-light stimulation to the sum of individual contributions revealed to be unitary (β = 1.04, linear regression model of condition acou + optog$^+$ was significantly predicted by the sum of acou and optog$^+$, $t_{(7)}$ = 15.0, p < 0.001; ANOVA of regression also indicated that the sum of acou and optog$^+$ explained a significant proportion of variance, R^2 = 0.884, $F_{(1,7)}$ = 226, p<.001). In other words, delivery of both stimuli resulted in an increase of the gamma rhythm identical to the mathematical sum of increases induced by the 2 stimuli alone. The additive combination of stimulation modalities implies that the effect of providing an auditory input to the ACx does not interact with the effect evoked by PV$^+$-interneuron inhibition—possibly indicating that these manipulations modulate gamma activity in the ACx by means of a common neural mechanism (see Table 4 of REF. 145). This common process could simply begin with excitation of the local neuronal population, as it is the case upon acoustic stimulation[11,139,146–148], and would indicate that gamma activity could be seen as a proxy for the amount of excitation received by the local population. I tested this hypothesis and describe the corresponding outcome in the next section.

5.1.3 PV$^+$ cells prevent over-excitation of the auditory cortex by acoustic stimulation

Metherate and Cruikshank (1999), followed by Brosch, Budinger and Scheich (2002), have presented clear evidence for the simultaneous increase in discharge rate and gamma amplitude in the ACx succeeding the recruitment of thalamocortical afferents and acoustic stimulation respectively. Moreover, Adesnik and Scanziani (2010) have convincingly demonstrated in vivo, through a precise optogenetic activation of neocortical pyramidal cells, that tonic excitation is sufficient to generate gamma activity. Consequently, I attempted to ascertain if optogenetically magnified auditory-induced gamma activity is indeed accompanied by an overexcited cortical state, as one would also expect from removing a sizable portion of inhibition within the ACx. I first analysed the transient population activity time-locked to the acoustic stimulus (Fig. 5.4A). Together with histological evidence (see Sect. 7.2.10.f), the shape of the middle-latency auditory-evoked potentials (AEPs) confirmed the location of the recording sites as lying deep in the ACx[122–124] (in layers IV and V). The AEP that was consistently the most prominent one across mice and conditions displayed negative polarity and a latency of 15 ms (N15) relatively to the onset of the stimulus, slightly lower to what has been reported in awake[124] and anaesthetized rats[150,151] (20 ms). This stimulus-locked trough in the LFP has been shown to reflect both subthreshold[17,123] and suprathreshold[17,124,146,147,150,151] excitation of the local neuronal population by thalamocortical[123,152–154] and cortico-cortical[122,152,154–158] connections. A study reporting the optogenetic recruitment of pyramidal cells has provided further causal evidence for the generation of negative deflections in the LFP as a result of excitation of the local neuronal population[66].

According to expectations, inhibition of PV$^+$ interneurons amplified the AEP N15, suggesting that the local recorded population is in a more excited state when perisomatic inhibition to pyramidal cells is reduced, i.e. the decrease of perisomatic inhibition disinhibited pyramidal cells in the ACx (Fig. 5.4B; condition acou + optog$^+$ shows above-unit mean ratios of the amplitude of N15 to both the amplitude with acou, ≈ 154%, and with acou + optog$^-$, 134 ± 13%, n = 8; paired Student's t-

tests presented significant differences between acou + optog$^+$ and both acou + optog$^-$ and acou, respectively, $t_{(7)} = 7.49$, $p < 0.001$, and $t_{(7)} = 5.91$, $p = 0.002$, after Šidák correction, $m = 3$, two-sided; supplementary statistical results in the legend of figure). The control blue-light manipulation did not have an effect on N15 (paired Student's *t*-test did not result in any significant difference between acou and acou + optog$^-$, $t_{(7)} = 1.36$, $p = 0.517$ after Šidák correction, $m = 3$, two-sided). These results were validated in the sham-injected group of mice, which did not reveal an effect of light stimulation on the amplitude of N15 (paired Student's *t*-tests did not show any significant difference between the amplitude ratios of acou + optog$^+$ and both acou + optog$^-$ and acou, respectively, $t_{(3)} = 0.057$, $p = 1.00$, and $t_{(3)} = 0.027$, $p = 1.00$, after Šidák correction, $m = 3$, two-sided). The latency of N15 remained unchanged by light stimulation and eNpHR expression (Fig. 5.4C; 14.2 ± 1.1 ms, $n = 36$; supplementary statistical results in the legend of the figure).

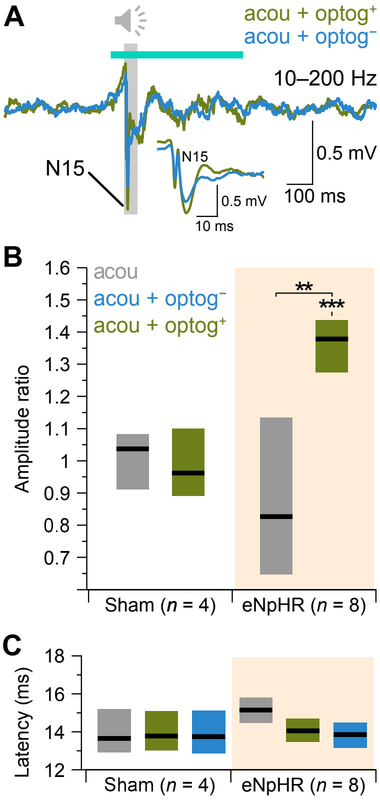

Figure 5.4 | Inhibition of PV$^+$ cells amplifies auditory-evoked potential. A | Average broadband (10–200 Hz) LFP traces from 20 repetitions of the acoustic stimulus (acou; grey shade; GWN, 50 ms, 5–80 kHz) evidence a more excited local neuronal population, through the amplification of auditory-evoked potential (AEP) N15, upon inhibition of PV$^+$ cells in the ACx with blue and green light (optog$^-$ and optog$^+$ respectively; bright-blue 500-ms-long horizontal bar). Traces display data obtained in the same mouse as in all previous original figures. **B** | N15 AEPs from 8 eNpHR-expressing mice indicates significantly increased amplitudes (normalized to the response in condition acou + optog$^-$) when PV$^+$ interneurons are inhibited (unbalanced two-way ANOVA showed a main effect of light stimulation, $F_{(2,30)} = 5.96$, $p = 0.007$, but not of eNpHR expression, $F_{(1,30)} = 1.55$, $p = 0.222$; and detected interaction between factors, $F_{(2,30)} = 6.11$, $p = 0.006$.). **C** | The latency of N15 in 8 eNpHR-expressing mice was not significantly altered by inhibition of PV$^+$ interneurons (unbalanced two-way ANOVA did not reveal any effect of either light stimulation, $F_{(2,30)} = 1.01$, $p = 0.375$, or eNpHR expression, $F_{(1,30)} = 0.48$, $p = 0.496$). $^{**}p < 0.01$, $^{***}p < 0.001$. Additional statistical results in text. Values are median and IQR.

Interestingly, a slow long-latency AEP, consisting of a small-amplitude bipolar wave, was consistently observed across mice during green-light stimulation at a latency of approximately 100 ms (Fig. 5.4A). This slow AEP is remarkably similar to those preceding gamma oscillation reported by Franowicz and Barth (1995) and Brosch et al. (2002), during acoustic stimulation, and by Metherate and Cruikshank (1999) upon thalamic stimulation. In fact, this potential directly precedes the time window of maximum auditory-induced gamma power that I observed during inhibition of PV$^+$ cells (see previous section). Metherate and Cruikshank (1999), Brosch et al. (2002) and Talwar, Musial and Gerstein (2001) attribute an excitatory nature to this slow potential and the first study further demonstrates its necessity for the occurrence of gamma oscillations. Taken together, these findings support the above-mentioned optogenetic disinhibition of the ACx.

The next question I posed was whether the optogenetically induced gamma activity would be produced in the cortex itself or whether it would be merely explained by an overexcited ACx amplifying rhythmic thalamocortical input. The fact that the manipulation here applied was specifically administered to the ACx, and not to any of its relays in the auditory system, favoured the former hypothesis. The scrutiny of this issue is addressed in the next section.

5.1.4 Overexcited auditory cortex does not amplify thalamic gamma oscillations

Previous studies have shown that gamma activity in the auditory cortex is modulated by its preceding relays in the auditory system[159], particularly the medial geniculate body[123,160–162] (MGB). What is more, Minlebaev, Colonnese, Tsintsadze, Sirota and Khazipov (2011) have specifically demonstrated transmission of gamma oscillations from the thalamus to the cortex. Therefore, it was imperative to check whether the inhibition of PV^+ cells could induce an overexcited cortical network that, in turn, would amplify gamma activity coming from its thalamic relay. I first confirmed the exact location in the MGB of cells projecting to the recorded cortical site by injecting a retrograde tracer (RetroBeads) into the ACx (Fig. 5.5A) and subsequently localizing the origin of its thalamic afferents (Fig. 5.5B). In the same set of animals where I collected the data reported in preceding sections, I also recorded the LFP from a microelectrode implanted into the previously identified source of projections from the MGB to the ACx (Fig. 5.5C–E).

I attempted to detect synchrony between the instantaneous amplitudes of gamma oscillations in the ACx and MGB (Fig. 5.5F) and, additionally, to determine the lag between these brain areas (Fig. 5.5G). Metherate and Cruikshank (1999) have electrically stimulated the MGB and registered a transmission lag measures approximately 3 ms. Similarly, Minlebaev et al. (2011) report gamma-coupled multiunit-activity cross-correlation lags around 5 ms. In all conditions I experimentally tested, I detected no lag significantly different from zero (results not shown; lag measured as the average maximum in the cross-correlogram of gamma-band amplitude from the ACx and MGB). Moreover, I did not detect any increase in the synchrony of the gamma rhythm between the 2 brain regions following acoustic and/or optogenetic stimulation (Fig. 5.5H; supplementary statistical results in the legend of the figure). To account for phase coupling I reanalysed the data using an all-encompassing measure of synchrony, namely coherence (the previous measure was specific for amplitude comodulation). In the same way, this analysis did not reveal any intensification of synchrony upon stimulation (Fig. 5.5I; supplementary statistical results in the legend of the figure).

I demonstrated the influence of perisomatic inhibition on fast rhythmic activity and neural network excitability and excluded the possibility of a thalamocortical transmission of fast rhythmic activity. Next, I asked whether the perturbation of perisomatic inhibition and gamma rhythm would impact on behaviour and, in turn, if changes in behaviour would be associated to changes in fast periodic activity. The forthcoming sections describe an experiment I devised to specifically tackle those matters.

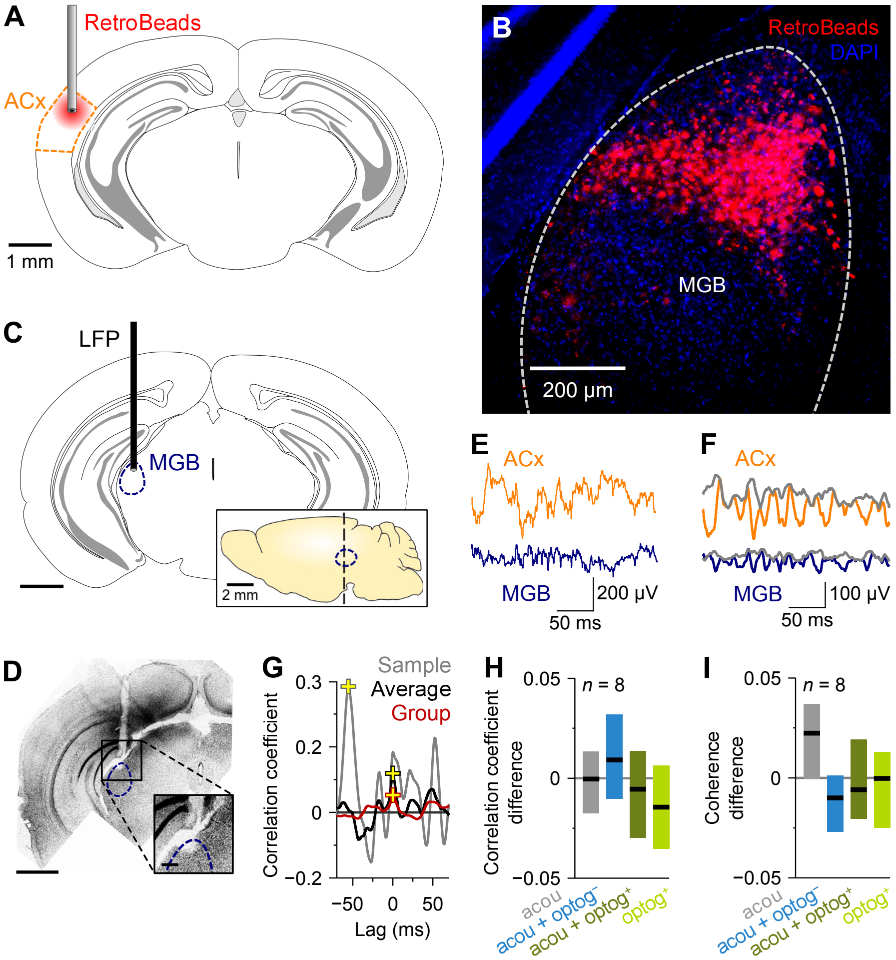

Figure 5.5 | Gamma rhythm is not conveyed to the ACx from its thalamic relay. A | Stereotactic injection of a retrograde tracer (red RetroBeads) into the left ACx (orange) of mice for labelling the previous auditory relay, the medial geniculate body (MGB). **B** | Epifluorescent image of the distribution of cells (red) in the left MGB (demarcated by dashed lines) projecting to the ipsilateral ACx. Identification of the limits of the MGB was aided by the DAPI staining (blue). **C** | Local field potentials (LFP) were recorded from a microelectrode implanted into the MGB (blue) ipsilateral to the recorded ACx. Inset | Sagittal view of the MGB (blue). **D** | Reconstruction of coronal slice confirms the adequate placement of the microelectrode in the MGB. **E** | Representative broadband (10–200 Hz) LFP traces of simultaneous responses in the ACx (orange) and MGB (blue) to the acoustic stimulus (acou; GWN, 50 ms, 5–80 kHz) extracted from 150–400 ms after sound onset. **F** | The instantaneous amplitudes (grey) of the gamma-band filtered traces illustrate how the instantaneous amplitudes of auditory-induced gamma oscillations change over time in the ACx (orange) and MGB (blue). **G** | Sample cross-correlogram of the previously illustrated instantaneous amplitudes (grey), average cross-correlogram of gamma amplitudes from 20 repetitions of the acoustic condition (black) and average cross-correlogram of gamma amplitudes from 8 mice (red). The plus signs (yellow) indicate the maxima of the cross-correlograms. **H** and **I** | Difference of gamma-amplitude cross-correlation and gamma-band coherence between the post-stimulus period (150–400 ms after sound onset or equivalent moment) and baseline in 8 eNpHR-expressing mice does not significantly increase upon acoustic stimulation nor during inhibition of PV$^+$ interneurons in the ACx with blue and green light (optog$^-$ and optog$^+$ respectively; repeated measures ANOVAs did not display an effect of optogenetics on either cross-correlation, $F_{(3,21)} = 0.95$, $p = 0.434$, or coherence, $F_{(3,21)} = 2.27$, $p = 0.110$; one-sample Student's *t*-tests did not ascribe significance to differences to 0 in both cross-correlation and coherence, each $p > 0.05$ after Šidák correction, $m = 4$, two-sided). Additional statistical results in text. Values are median and IQR. Whole-slice coronal reconstruction and voltage traces display data acquired in the same mouse as in all previous original figures.

5.2 Fear learning requires contribution of PV$^+$ cells

To study the role of PV$^+$ interneurons in auditory processing and learning I employed a behavioural paradigm, auditory fear conditioning, whose underlying neural circuit is well defined[11,163,164]. This paradigm of Pavlovian conditioning typically consists of conditioning a subject's fear response to an initially neutral acoustic stimulus by stablishing an association between that stimulus and an unpleasant stimulus (here a foot shock). After pairing these stimuli (i.e. simultaneous stimulus delivery) mice learn to associate the occurrence of the acoustic stimulus to the unpleasant stimulus and manifest the learned association by standing still (i.e. *freezing*, an endogenous defence response in rodents). The relevance of this learning process stems from the fact that it allows mice to use the conditioned stimulus (CS, i.e. the sound) as a predictor of the aversive unconditioned stimulus (US, i.e. the foot shock).

I devised a differential conditioning protocol whereby 2 similar acoustic stimuli are differently conditioned to foot shock (Fig. 5.6A). Whereas one of these sounds was paired to the shock (CS$^+$), the other would always follow the shock with some variable delay (CS$^-$). As a result of the disparate order of presentation of the two acoustic stimuli (relative to shock), they are expected to be conditioned differently: the CS$^+$ should act as a strong predictor of the US, whereas CS$^-$ should only be a weak predictor of the US[11,165,166]. This difference in conditioning is here exploited with the intent of doubling the conditions (i.e. CSs) available to test fear learning, thus mitigating the impact that possible ceiling and floor effects might have on the interpretation of experimental results. Other domains of the auditory system, besides the ACx, have been implicated in fear learning such as the medial MGB[166–169]. As a result, I carefully chose 2 acoustic stimuli that are considerably similar to each other (identical specifications except for reversed time course; Fig. 5.6B) in an attempt to force their discrimination to require the ACx and its markedly superior ability to distinguish fine differences between complex sounds[170–172] and to associate meaning with these sounds[173,174].

Letzkus et al. (2011) have shown that the majority of layer-II/III PV$^+$ interneurons in the ACx are inhibited during US delivery and that counteracting this inhibition impairs learning. While Aizenberg, Mwilambwe-Tshilobo, Briguglio, Natan and Geffen (2015; in their Supplementary Fig. 13) displayed additional evidence for the significance of that epoch of inhibition in learning, it remains nevertheless unreported an attempt to enhance learning by promoting both gamma oscillations and the natural disinhibition of the ACx specifically in response to the US. I here describe the behavioural results obtained in 2 separate conditions related to distinct manipulations of the ACx during the US: in one condition, I interfered with the association between CS$^+$ and US by providing strong optogenetic inhibition to PV$^+$ cells with green light (*optog$^+$* condition); in the other condition, this association was manipulated via weak optogenetic inhibition of PV$^+$ cells with blue light (*optog$^-$* condition). The latter condition was deliberately used as a between-group control ensuing its earlier validation (Figs. 5.2F, 5.3D and 5.4B). To ensure that gamma oscillations were amplified during the optogenetic manipulation, I reproduced the results reported in Sect. 5.1.1 using acoustic stimuli more similar to those employed in fear conditioning (i.e. up- and down-chirps instead of GWN, see Sect. 7.2.4.b; results not shown).

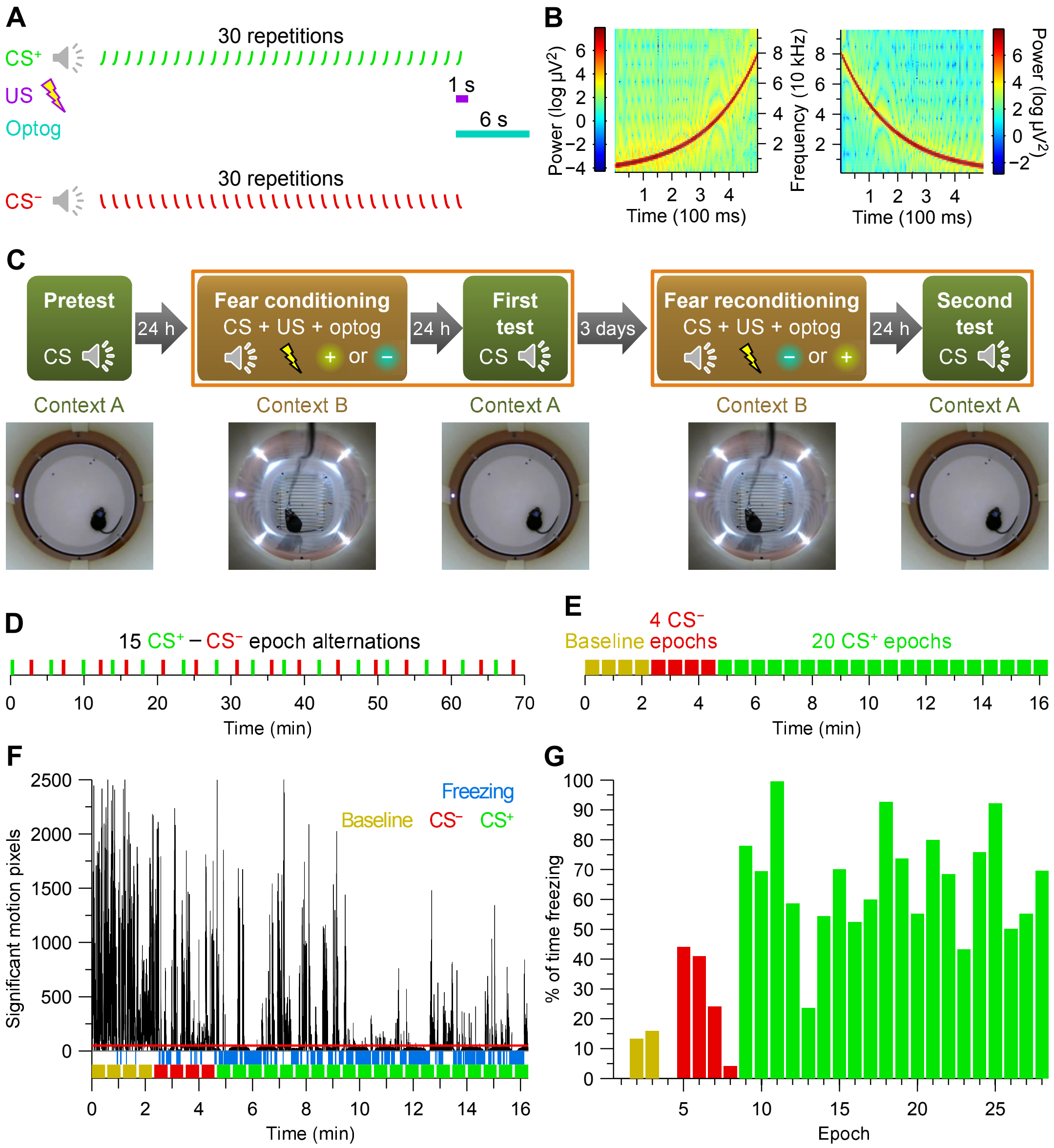

Figure 5.6 | Auditory fear conditioning as a behavioural paradigm for studying learning in mice. A | Differential fear conditioning protocol with 6-s optogenetic stimulation (optog; blue bar) starting at the pairing of conditioned stimulus (CS^{+}; green ticks) with the 1-s foot shock used as unconditioned stimulus (US; purple bar). Presentations of 30 CS^{+} were followed, with variable delay, by 30 repetitions of a similar stimulus not paired to the US nor optogenetically manipulated (CS^{-}; red ticks). **B** | Spectrograms of the broadband up- and down-chirps used, respectively, as CS^{+} and CS^{-} (0.5 s, 5–80 kHz). **C** | Full behavioural protocol commenced with a pretest on CS-induced freezing in naive mice (green block). For the next 2 days, mice underwent fear conditioning (brown block), accompanied by inhibition of PV^{+} cells in the ACx with either green or blue light (optog^{+} or optog^{-} respectively), and, after that, retrieval of learned fear with CS (2nd green block). 3 days later, mice were reconditioned while being manipulated with a different light (2nd brown block) and, 1 day later, tested again with CS for learned fear (3rd green block). **D** | Fear conditioning and reconditioning protocols comprised 15 alternations of epochs (i.e. 30 repetitions) of CS^{+} and CS^{-} (green and red respectively). **E** | Fear pretest and test protocols consisted entirely of 4 epochs for retrieval of baseline freezing levels (yellow), followed by 4 CS^{-} epochs (red) and finally by 20 CS^{+} epochs (green). **F** | Automated measurement of movement (black graph) and detection of freezing (blue) during a test session preceded by fear conditioning and manipulation with blue light. Freezing was detected whenever movement was below threshold (red line) for at least 2 s. **G** | Fraction of time spent freezing on each epoch of that test session.

All data reported here were collected strictly after fear conditioning mice, i.e. while testing mice for fear responses to the conditioned stimuli (Fig. 5.6C). Fear testing was carried out without optogenetic stimulation, in a different context (changed visual, haptic and olfactory cues) and employing a protocol, unlike the one used in conditioning (Fig. 5.6D), especially suited for fear retrieval (Fig. 5.6E). The tested fear response, expressed as freezing, was measured in terms of the extent of movement (Fig. 5.6F,G). In order to supplement the experiment with a within-subject control, mice were thereafter reconditioned (*recond* condition) and optogenetically manipulated with the alternative light (Fig. 5.6C). Finally, the animals were retested for fear responses. From the data sampled during the fear test session that followed reconditioning, I will here report only those pertaining to mice whose PV^+ cells—during initial conditioning—were strongly inhibited with green light (optog^+).

Mice submitted to control optogenetic stimulation (optog^-) during fear conditioning displayed high freezing levels throughout presentation of both CS^+ and CS^- (Fig. 5.7A). In these mice, fear extinction was observable only after a few CS^+ epochs, whereas in mice submitted to strong PV^+-cell inhibition (optog^+) fear extinction would occur after a single CS^+ epoch (Fig. 5.7B). Reconditioning of the latter group of mice (recond) effectively prolonged fear extinction (Fig. 5.7C). Taken together, and considering that stimuli did not elicit a fear response before conditioning (Fig. 5.7D; median freezing level of 2.88%, IQR = 1.66–4.10%, $n = 10$, for CS^+ in naive mice; results of statistical analysis in the legend of Fig. 5.7D), these results indicate that fear conditioned mice not only exhibited a learning-induced response to the CS, but also saw these responses impacted by manipulations (Fig. 5.7E; two-way ANOVA revealed main effects of both test phase, $F_{(2,36)} = 24.8$, $p < 0.001$, and manipulation, $F_{(2,36)} = 5.80$, $p = 0.007$; these effects were not qualified by an interaction between factors, $F_{(4,36)} = 0.72$, $p = 0.585$). In other words, stimuli that were equally neutral to naive animals, not only were be perceived differently after fear conditioning, but also perception of these stimuli was altered by disinhibition of pyramidal cells in the ACx.

Contrary to the expectations of promoting learning by contributing to gamma oscillations (see Sect. 5.1.1) and to the disinhibition of the ACx[11], results indicate an impairment of fear learning when inhibiting PV^+ interneurons during CS–US pairing, manifested in a reduced fear response to the CS^+ (≈ 28% reduction in mean freezing levels with optog^+ in comparison to optog^-, $n = 5$; results of statistical analysis in the legend of Fig. 5.7E). Reconditioning with control optogenetic manipulation (optog^-) could not fully recover fear levels (in spite of a ≈17% mean increase of freezing levels with recond relatively to optog^+, $n = 5$, a paired t-test failed to attribute significance to this difference, $t_{(4)} = 2.83$, $p = 0.135$ after Šidák correction, $m = 3$, two-sided; nonetheless, an independent-samples t-test did not reveal a significant difference between recond and optog^-, $t_{(8)} = 0.93$, $p = 0.760$ after Šidák correction, $m = 3$, two-sided). Next, I attempted to collect evidence for changes in the gamma rhythm during fear retrieval; such changes would provide a much sought-after link between behavioural deficits and disturbed gamma activity.

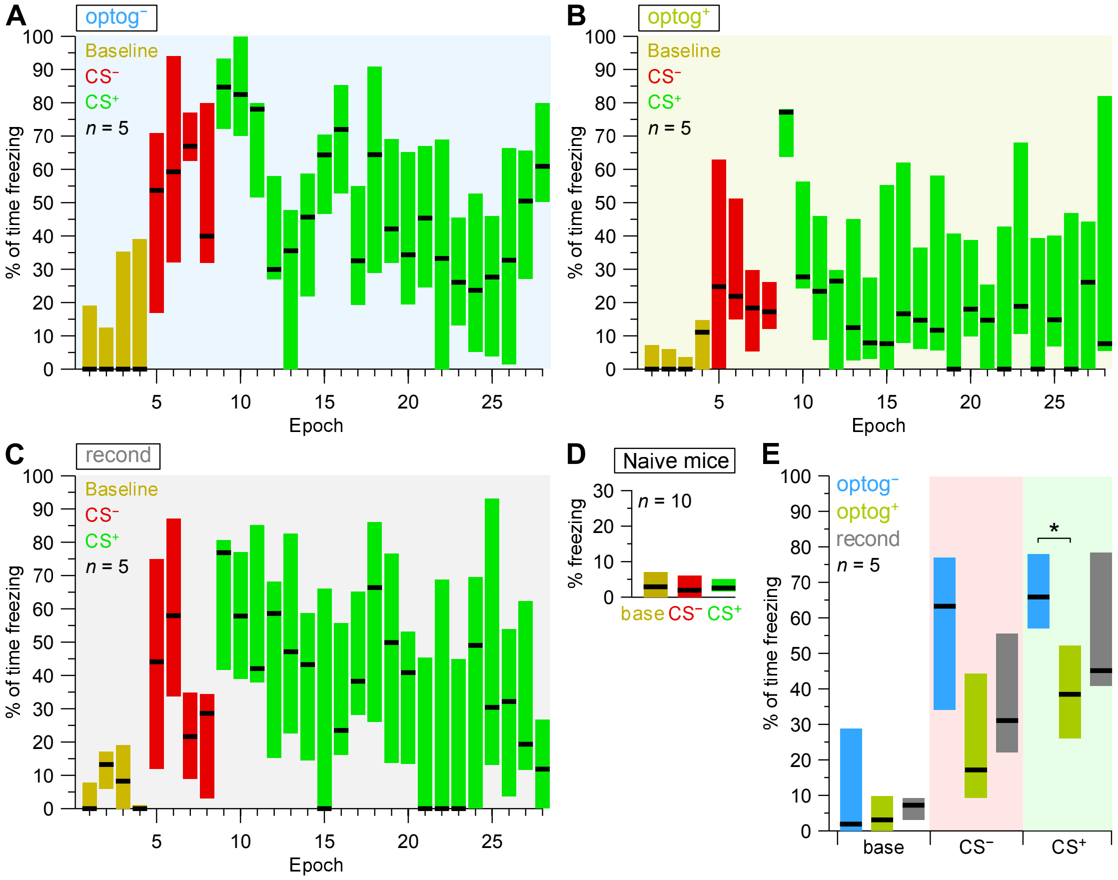

Figure 5.7 | Disinhibition of the ACx reduces learning of conditioned fear responses. A and **B** | Freezing without light stimulation one day after fear conditioning and inhibiting PV$^+$ cells with, respectively, blue light (optog$^-$) or green light (optog$^+$) in two groups of identically treated, eNpHR-expressing cage mates (n = 5 each). Despite low baseline freezing (yellow), responses to both CS$^-$ (red) and CS$^+$ (green) were considerably high in the optog$^-$ condition and appreciably lower with optog$^+$. **C** | Freezing without light stimulation in the reconditioned (recond) group of mice. Reconditioning was performed on the previous day while stimulating with blue light the mice initially conditioned together with green-light stimulation. Freezing responses are the intermediate between the 2 other conditions (optog$^-$ and optog$^+$). **D** | Naive mice displayed trivial freezing levels and no significant difference across test phases (non-parametric Friedman test did not identify any effect, $X^2_{(2,\, n\,=\,10)} = 0.065$, $p = 0.968$). **E** | Compared to the blue-light manipulated mice (optog$^-$), mice where PV$^+$ interneurons were strongly inhibited (optog$^+$) suffered a significant decrease in fear learning (independent-samples t-test presented a significant difference between these 2 conditions in response to CS$^+$, $t_{(8)} = 3.17$, $p = 0.039$ after Šidák correction, $m = 3$, two-sided). $^*p < 0.05$. Additional statistical results in text. Values are median and IQR.

5.3 Stimulus relevance dictates electrophysiological response

Headley and Weinberger (2011) have shown that alterations of gamma power in the ACx correlate with behavioural changes. On a later paper[177], the same authors provide causal evidence for changes in gamma activity in the ACx following fear conditioning. These studies suggest that auditory-induced gamma oscillations reflect the learned relevance of stimuli. Accordingly, I investigated whether impairments in auditory fear conditioning, upon decreased perisomatic inhibition, might be accompanied by changes in CS-induced gamma activity. In effect, my results indicate that fear reconditioning recovered CS$^+$-induced gamma activity (from 0.39 ± 0.78 to 1.29 ± 0.56 dB, n = 5) to levels similar to those observed in the control condition (1.18 ± 0.93 dB, n = 5; Fig. 5.8A–C; two-way ANOVA revealed a main effect of test-phase, $F_{(2,24)} = 4.85$, $p = 0.038$, but failed to detect a significant effect of manipulation, $F_{(1,24)} = 2.79$, $p = 0.082$; no interaction detected between factors, $F_{(2,24)} = 0.39$, $p = 0.680$; independent-samples *t*-test did not attribute significance to the difference between optog⁻ and recond, $t_{(8)} = 0.22$, $p = 0.995$ after Šidák correction, $m = 3$, two-sided; further statistical results in the legend of the figure). In spite of a considerable decrease in CS$^+$-induced gamma power following inhibition of PV$^+$ cells during CS$^+$–US pairing (≈ 0.79 dB), an independent-samples *t*-test failed to attribute significance to this difference (between optog$^-$ and optog$^+$, $t_{(8)} = 1.47$, $p = 0.451$ after Šidák correction, $m = 3$, two-sided).

Alterations to the amplitude of AEPs, in the neural circuit underlying fear conditioning, have been described upon stimulation of the auditory thalamus[169]. I probed similar changes in the ACx and found out that the amplitude of the CS$^+$-evoked potential N15 was significantly altered by inhibition of PV$^+$ interneurons (Fig. 5.8D,E; two-way ANOVA showed a main effect of manipulation, $F_{(2,24)} = 7.60$, $p = 0.003$, but not of test-phase, $F_{(1,24)} = 0.070$, $p = 0.793$; the effect was not qualified by an interaction between factors, $F_{(2,24)} = 0.77$, $p = 0.476$). Specifically, disinhibition of the ACx during CS$^+$–US pairing resulted in a diminished CS$^+$-evoked N15 (≈ 50% reduction in mean amplitude with optog$^+$ in comparison to optog$^-$, $n = 5$; results of statistical analysis in the legend of Fig. 5.8E). Reconditioning with control optogenetic manipulation (optog$^-$) could not fully recover the amplitude of N15 (≈ 38% raise in mean amplitude in recond relatively to optog$^+$, $n = 5$; paired *t*-test did not indicate a significant difference between these conditions, $t_{(4)} = 2.21$, $p = 0.250$ after Šidák correction, $m = 3$, two-sided; independent-samples *t*-test revealed no significant difference between recond and optog$^-$, $t_{(8)} = 1.74$, $p = 0.318$ after Šidák correction, $m = 3$, two-sided). The latency of the CS-evoked potential N15 remained unchanged by manipulations (Fig. 5.8F; 15.4 ± 1.3 ms, $n = 30$; results of statistical analysis in the legend of the figure).

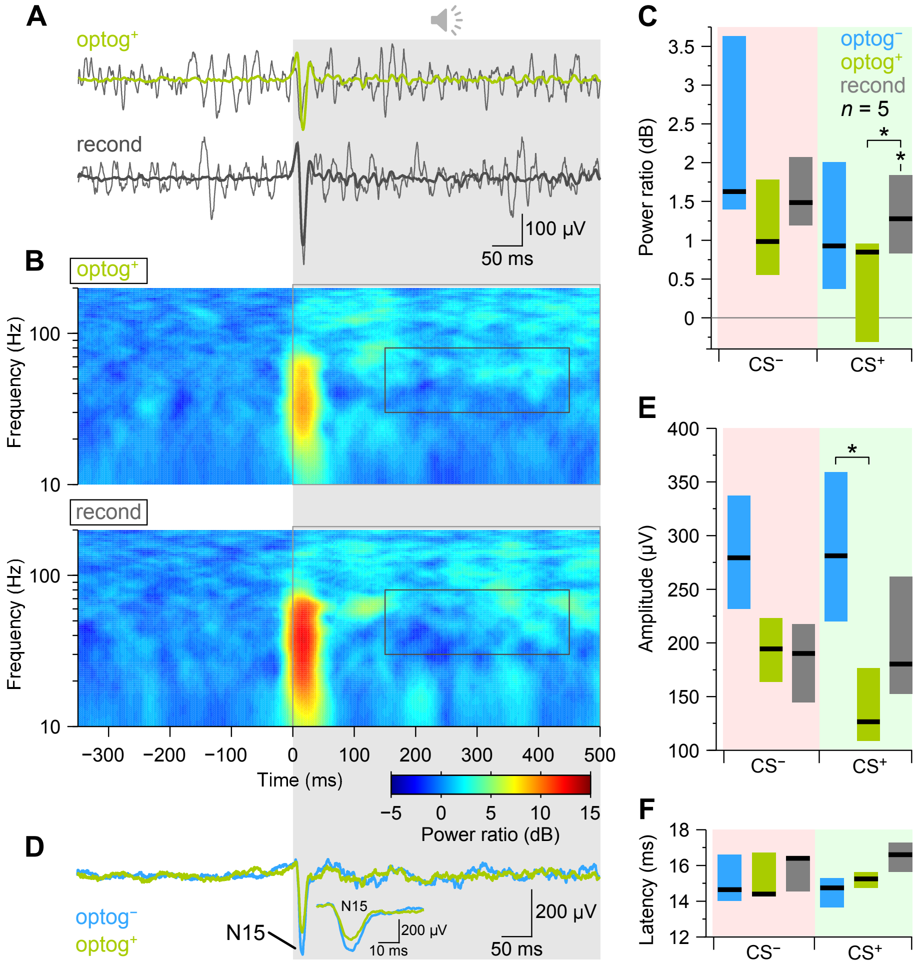

Figure 5.8 | Learning shapes responses in the ACx to fear-conditioned stimuli. A | Representative gamma-band-filtered traces (light grey), obtained during fear tests, show oscillatory activity before and during a repetition of the CS$^+$ (grey shade). The upper trace was obtained one day after both fear conditioning and inhibiting PV$^+$ cells with green light (optog$^+$). The lower trace was recorded one day after both reconditioning and stimulating with blue light the same mouse (recond). This gamma activity was not phase locked to stimuli as averages from 90 repetitions (thick lines) display no periodic activity (the wavelet visible during sound is an artefact of the large AEP N15). **B** | Spectrograms normalized to baseline (−350 to −50 ms) with average responses to CS$^+$ (90 repetitions). Gamma-band power was determined from 150–450 ms (inner rectangle). **C** | Baseline-normalized gamma power in two groups of identically treated, eNpHR-expressing cage mates ($n = 5$ each). One group underwent conditioning together with blue-light stimulation (optog$^-$); the other group was subjected to conditioning together with green-light stimulation (optog$^+$) and, afterwards, to reconditioning together with blue-light stimulation (recond). Reconditioning significantly increased response to CS$^+$ compared to the optog$^+$ condition (paired t-test, $t_{(4)} = 5.72$, $p = 0.014$ after Šidák correction, $m = 3$, two-sided). **D** and **E** | Average broadband (10–200 Hz) LFP traces from 90 repetitions of the CS$^+$ suggest a less excited ACx through the reduction of the AEP N15 in condition optog$^+$ relative to optog$^-$ (difference validated by independent-samples t-test on pooled data, $t_{(8)} = 3.11$, $p = 0.042$ after Šidák correction, $m = 3$, two-sided). **F** | The latency of N15 was not significantly different among conditions (two-way ANOVA of pooled data revealed no effect of either test-phase, $F_{(1,24)} = 0.064$, $p = 0.803$, or manipulation, $F_{(2,24)} = 1.95$, $p = 0.164$). $^*p < 0.05$. Additional statistical results in text. Values are median and IQR. Traces and spectrograms display data obtained in the same mouse as in Fig. 5.6F,G.

6 Discussion

Perisomatic inhibition is regarded as intimately linked to gamma oscillations by a voluminous body of literature (see Sect. 4.3). Causal evidence for its sufficiency[60,66–68] for the generation of gamma oscillations has been reported in preceding in vivo studies. Consistent with those results, in one of those studies, gamma oscillations have been attenuated by a reduction in perisomatic inhibiton[66]. However, so far, no study had investigated the necessity of PIIs for sensory-induced fast rhythmic activity, in particular, for auditory-induced gamma oscillations. Furthermore, amid a profusion of literature describing the contributions both of perisomatic inhibition to network synchronization[33,47–50] and of synchrony to sensory processing[60,68,113–117], there is a noteworthy scarcity of studies probing the role of perisomatic inhibition in sensory learning—only 3 studies provide some insight into the impact of manipulations of PV$^+$ interneurons on associative learning[11,67,175]—and these few enquiries present substantial limitations and even impose pitfalls upon the interpretation of findings. The first of such studies[11], does not make use of a specific manipulation; instead, perisomatic inhibition is tonically boosted, which likely silenced the ACx[174,178–180] and consequently precluded the conclusive identification of a specific circuit in the ACx necessary for learning. Another study[67], not only tests learning with tones, thus disregarding the propensity of the ACx to process complex sounds[170–174,181], but also does not confine the manipulation (i.e. gene knockout) to the ACx. Finally, the remainder study[175] also probes learning with tones and reports deficits in learning either with PII-mediated silencing of the ACx or with attenuation of perisomatic inhibition during a period not directly related to associative learning, but rather to auditory processing.

I have described results from an experiment devised to answer the overriding questions of whether perisomatic inhibition is indeed necessary for induction of the gamma rhythm and for learning in the ACx. The manipulation I applied consisted of the temporally well-resolved and reversible optogenetic occlusion of perisomatic inhibition in the ACx. The LFP and behaviour were examined in freely-moving mice submitted to acoustic and optogenetic stimulation. Expression of the light-gated chloride-pump eNpHR was considerably efficacious in and specific to PV$^+$ cells (both ≈ 70%), albeit specificity could have been underestimated as a result of incomplete diffusion of the anti-PV antibody into the 50-µm brain slices immunohistochemically analysed post mortem.

6.1 Generation of gamma oscillations in the neocortex

6.1.1 Role of perisomatic inhibition in the generation of gamma oscillations

Contrary to vast previous evidence, I have shown that perisomatic inhibition is not necessary to the generation of gamma oscillations. In fact, PII silencing has drastically increased gamma activity. Even though this finding directly challenges both the ING model[51] and the fast-spiking-gamma hypothesis (see Sect. 4.3) it does confirm the involvement of perisomatic inhibition in the modulation of the gamma rhythm. Whether this effect of PIIs on gamma activity is a result of perisomatic inhibition reducing synchrony among pyramidal cells, or whether it is a consequence of decreasing overall activity in pyramidal cells (Fig. 6.1A,B) cannot be unequivocally ascertained based on the experimental evidence reported here. Nevertheless, an attempt to reconcile the fast-spiking-gamma hypothesis with my findings suggests that the former proposition is false and the latter is correct—i.e. copious evidence supports the notion of perisomatic inhibition offering a window of opportunity for pyramidal cells to spike and, in turn, leading to synchronization of activity within a cell population; my results do not necessarily constitute evidence of the contrary, but rather indicate that perisomatic inhibition prevents overexcitation of pyramidal cells. These findings are consistent with the contribution of inhibition[6,7,9,28,182,183], notably perisomatic inhibition[27,184–186], to the excitation–inhibition (E/I) balance and with the contribution to the gamma rhythm resulting from biasing this balance towards excitation[9,66,149,187] as reported in preceding studies. It should be mentioned that is implausible that the amplification of the gamma rhythm reported here is due to spike contamination of the LFP[188], considering the low upper bound of gamma band (80 Hz) and the clear peak observed in this band (Fig. 5.2E). Moreover, the reported amplification of the gamma rhythm should not be a spectral artefact deriving from AEPs or any other non-oscillatory activity in the LFP since the average of voltage traces during the time window considered in spectral analysis is not visibly different from that during baseline.

At this point, it is opportune to discuss a study whose findings constitute probably the most relevant discrepancy between my results and the literature. Sohal, Zhang, Yizhar and Deisseroth (2009) have likewise optogenetically inhibited PV$^+$ cells (using the same mouse line and viral vector) and yet reported a decrease in optogenetically evoked gamma oscillations (and no effect on ongoing gamma oscillations). The cause for the discrepancy may lie in several experimental differences between studies: (a) the type of gamma-rhythm induction paradigm utilized by Sohal et al. (2009) is artificial and at least conceptually distinct from sensory stimulation (as suggested by the principal author in a later publication[109]), since it consisted of recruiting exclusively pyramidal cells in a single brain region; (b) the authors report event-evoked as opposed to event-induced gamma activity[140–142], i.e. spectral analysis was performed on data collected upon stimulation (1 ms after light pulse) which contrasts greatly with the much later window (100–350 ms after sound) analysed in the current study; (c) data was not collected in awake mice, as here, but instead in animals anaesthetized with a ketamine/xylazine mixture; (d) oscillatory properties of the probed neural circuit, the prefrontal cortex, may differ from those of the ACx. It is worthy of note that the authors did not observe a decrease in the ongoing gamma rhythm which calls into question the effect they reported for evoked-gamma oscillations.

Increased ongoing gamma activity has been reported before both in knockout mice lacking the NMDA receptor subunit NR1 specifically in PV$^+$ cells[67,95] and following the application of NMDA receptor antagonist[96–98]. Extensive experimental evidence has demonstrated that the application of NMDA receptor antagonists not only induces schizophrenia-related neuronal states in the cortex[99–104], but also that these states are characterized by overexcitation of pyramidal cells and hypofunction of inhibitory interneurons[105,106], particularly PIIs[107]. Those findings indicate that NMDA receptor inhibition mediates cortical excitation by disinhibition of pyramidal neurons and that schizophrenic phenotypes are associated to a PII-dependent shift in the E/I balance towards excitation; additional evidence attributed such imbalance to alterations specifically in PV$^+$ interneurons[91,110–112]. Consistent with such interpretations, augmented ongoing gamma power has been observed in schizophrenic patients[94]. Investigation of the effect of NMDA receptor inhibition and schizophrenia on sensory-induced gamma activity is, however, less conclusive in view of an existing discrepancy in the literature with some studies evidencing a decline[92,95] and others augmentation[94,98] (note that in REF. 98 a decrease is emphasised but its Fig. 4A2 clearly shows the opposite at latencies later than the middle-latency sensory-evoked potentials).

The inference that gamma activity resulting from reduced perisomatic inhibition relies chiefly on pyramidal cell overexcitation is far from being trivial. In fact, NMDA receptor antagonist-mediated intensification of the gamma rhythm and firing rate is accompanied by diminished synchronization of action potential discharge[97], which is indicative of the direct involvement of PII strictly in network synchronization (and balancing excitation with inhibition) rather than in rhythmic activity. As the experimental evidence I provided does not contradict the solid notion that perisomatic inhibition synchronizes discharge among pyramidal cells, these cells would be expected to be significantly desynchronized following the reduction of perisomatic inhibition I have optogenetically induced. Given that this desynchronization would have to be counteracted (Fig. 6.1C) by a major increase in overall neural activity to produce the large amplification of gamma activity I observed, it is likely that a ceiling effect or sublinearity would have been detected in the combined contribution of acoustic and optogenetic stimulation to gamma power, which did not happen (Fig. 5.3E). As a result, it is conceivable that other components of the neural circuitry are able to contribute to network synchronization and to compensate for the disruption to perisomatic inhibition (Fig. 6.1D).

Interestingly, previous work about the effect of cholinergic modulation on gamma oscillations and perisomatic inhibition points to the same relationship between these the neural aspects as the one reported here. Two studies[189,190] have shown that activation of basal forebrain cholinergic projections to the cortex increases sensory-induced gamma activity. Subsequently, Letzkus et al. (2011) have revealed a microcircuit in the ACx whose cholinergic activation disinhibits pyramidal cells by layer I interneuron-mediated inhibition of PV$^+$ interneurons. Taken together, these studies seem to indicate that silencing PIIs amplifies gamma oscillations, consistently with my findings. Surprisingly, one of these studies[190] demonstrated that such cholinergic modulation of cortical activity is accompanied by increased synchronization of neuronal discharge, which further supports the involvement of neuron types other than PIIs in network synchronization.

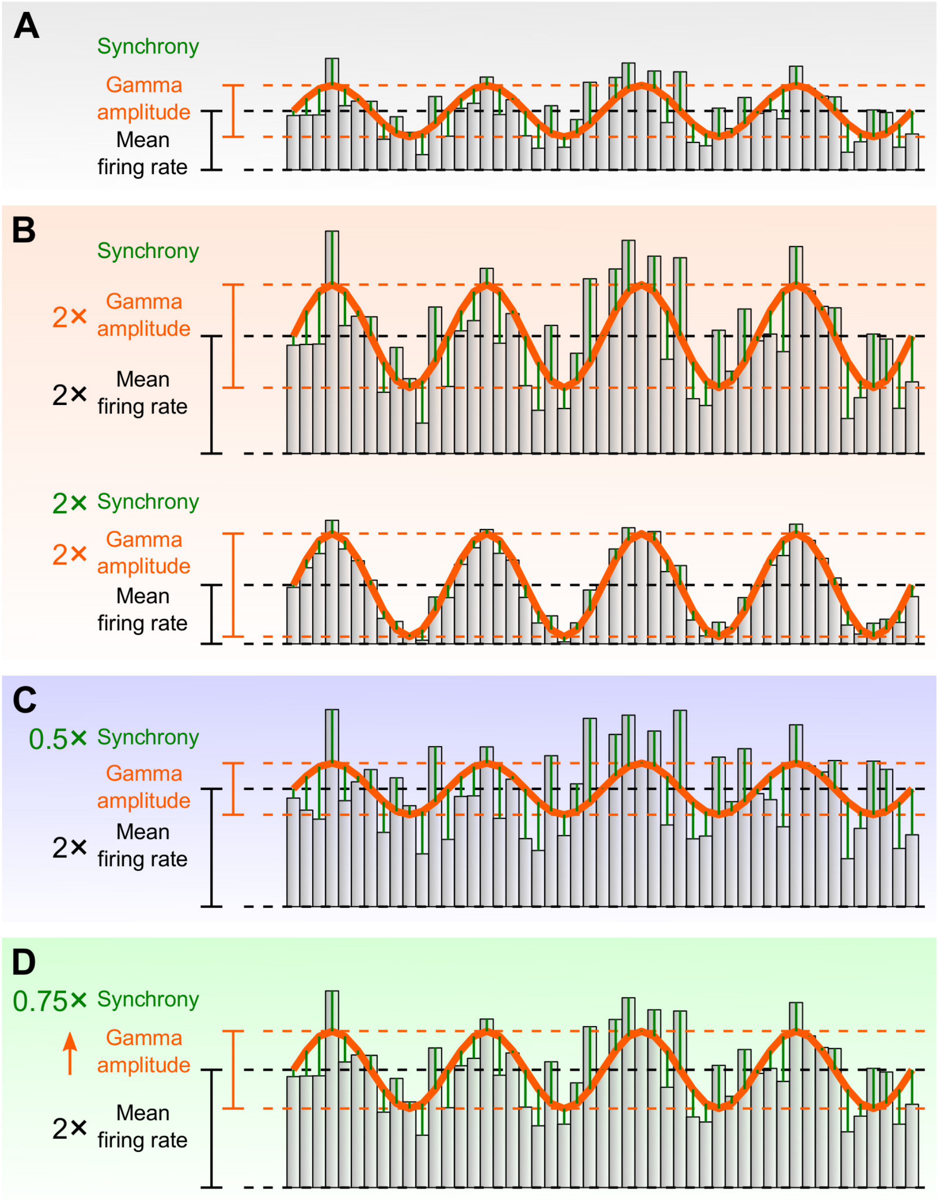

Figure 6.1 | Contribution of the network E/I balance and synchrony to the gamma rhythm. For illustrative purposes, a schematic gamma wave of constant amplitude and period (orange) is superimposed on and aligned to fictitious multiunit activity (MUA, grey). The greater the synchrony, the smaller the differences (green) between the gamma wave and MUA. A | Initial state. B | Doubled gamma amplitude could result from doubling either the mean firing rate or the synchrony. C | The effect of doubling the mean firing rate is counteracted by halving synchrony; as a result, gamma amplitude remains unchanged. D | Increased gamma amplitude resulting from doubled mean firing rate and a minor reduction in synchrony.

6.1.2 Alternative intracortical generators of gamma oscillations

The observation of an optogenetically amplified AEP N15 and unchanged synchrony in gamma waves from the ACx and MGB amounts to the conclusion that the optogenetic induced gamma oscillations are generated intracortically. First, considering that the AEP N15 arises both from thalamocortical[123,152–154] and cortico-cortical projections[122,152,154–158] and that the optogenetic manipulation was limited to the ACx, it is unconceivable that a change in such a short-latency response would be caused by the thalamocortical loop[161,162,191–194], which excludes the possibility of an optogenetic alteration to the thalamocortical projections. The optogenetic amplification of gamma oscillations constitutes a novel finding—even though earlier work has demonstrated that an increase in GABAergic inhibition in the ACx can reduce the N15 AEP[150], to my knowledge, no study hitherto had reported the reciprocal. It is worth mentioning that the enlargement of the N15 AEP should not be an outgrowth of optogenetically evoked gamma since the optogenetic stimulation alone does not evoke a potential (in average traces; Fig. 5.3A) and the visible AEPs seem to be composed only of episodic deflections and not of oscillatory activity (Fig. 5.4A). It is also improbable that the change in the amplitude of N15 is due to a light-induced artefact[195] (resulting from the photovoltaic effect) as the same effect on N15 was evident in data pertaining to a mouse whose recording tetrode was painted black to avoid that artefact (Fig. 5.4A); additionally, any low-frequency event such as a light-induced artefact would have been filtered out by the band-pass filter applied to the data. Second, the lack of an increase in synchronization between the ACx and the MGB during weakened cortical perisomatic inhibition, implies that the augmentation of gamma activity in the absence of perisomatic inhibition cannot be explained by the elementary amplification of fast thalamic rhythms within the ACx. This is in keeping with preceding work showing that sensory-induced gamma-band oscillations in neuronal firing rate do not depend on rhythmic input from the thalamus but rather result from an intracortical mechanism[113].

I propose 2 possible mechanisms of intracortical rhythmogenesis that could explain my results and provide alternative sources of gamma oscillations in the absence of perisomatic inhibition: (a) a mechanism, in support of the PING model[51], could consist of an overexcited network of reciprocally connected pyramidal cells and non-PIIs (i.e. GABAergic interneurons lacking PV; Fig. 6.2A); (b) a different mechanism could rely on single-cell properties that would support gamma-band rhythmicity and the ability of a neuron type to act as a *pacemaker*; such neuron could allow the overexcited local circuit to amplify the gamma wave transmitted from another brain region without requisite inhibition (Fig. 6.2B). The possibility that the optogenetic amplification of gamma oscillations stemmed from volume conduction[147,196,197] must be ruled out before proceeding with the interpretation of results. Given that the manipulation I applied induced an increase in gamma power, for this change to result from gamma activity being passively transmitted from distant non-optogenetically stimulated circuits in the ACx, the local gamma-band signal should be anti-correlated to the transmitted signal before manipulation; in this way, the destructive interference between these signals could be cancelled by an hypothetical reduction of the local rhythmic activity. In reality, to the best of my knowledge, no such anti-correlation of gamma waves within the ACx has been reported to date.

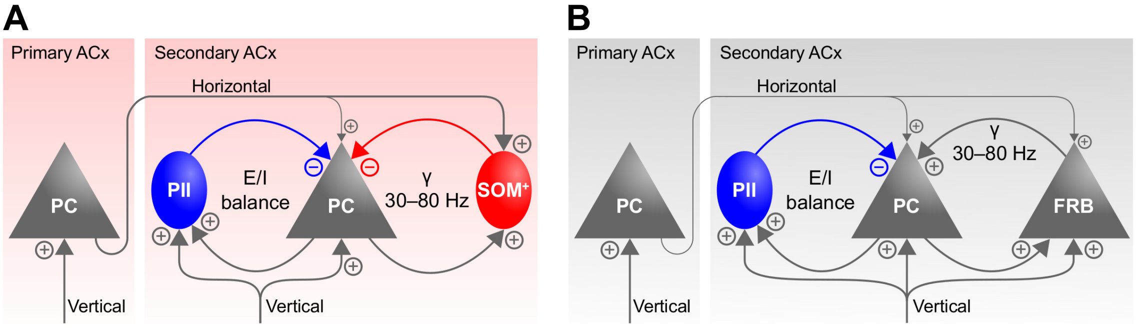

Figure 6.2 | Alternative motifs of neuronal connectivity underlying gamma oscillations. A | Schematic illustration of a PING-based[51] mechanism for generation of gamma oscillations (γ). Excitatory drive is conveyed either by horizontal projections arising from layer II/III in the neocortex or by vertical projections from layer IV[15]. The E/I balance[6] is controlled by PIIs and the gamma rhythm emerges from interaction between another inhibitory interneuron type—presumptively SOM⁺ interneurons—and the pyramidal cells (PC). The slow depolarizing wave initiating gamma activity[123] could be explained by the weak horizontal input to pyramidal cells[15]. B | Schematic of a mechanism of gamma oscillations that comprises fast rhythmic bursting (FRB) pyramidal cells able to act as a pacemaker[198–202]. The strong output of these neurons synchronizes the rest of the pyramidal-cell population.

6.1.2.a Pyramidal–interneuron gamma propagation without perisomatic inhibition

A comprehensive documentation of intracortical transmission of gamma activity has been laid out in the ACx of rats by Franowicz and Barth (1995) and Barth and MacDonald (1996)—with acoustic stimulation—and by Metherate and Cruikshank (1999) upon thalamic stimulation. Franowicz and Barth (1995) have observed that gamma activity propagates intracortically independently of the AEPs and Barth and MacDonald (1996) established the direction of propagation to be from the primary to secondary ACx. Metherate and Cruikshank (1999) specifically have demonstrated that stimulus-induced gamma oscillations, at long latencies such as the one displayed here, is the product of a series of events: (a) starting with focal glutamatergic activation of layer-IV neurons by thalamocortical afferents, (b) progressing through polysynaptically generated gamma-band fluctuations (depending on ionotropic excitatory and inhibitory receptors) and, ultimately, (c) spreading polysynaptically throughout the rest of the ACx. Taken together, these reports suggest that a slow wave of excitation propagates from the primary to secondary ACx activating mutually connected pyramidal cells and GABAergic interneurons, which eventually produces gamma waves.

The foregoing conclusion is in keeping not only with the fact that my recordings were quite likely performed in the dorsal secondary ACx, but also with the appreciable similarity between the latency of optogenetically amplified auditory-induced gamma activity (150 ms; Fig. 5.2D) and the lag of transmission that Metherate and Cruikshank (1999; in their Fig. 8) determined for the slow-potential-dependent transmission of gamma waves across the ACx. The fact that Barth and MacDonald (1996) have found the gamma wave spread within the ACx to be described by a lag of 2–4 ms indicates that, despite the slow velocity of transmission of the depolarizing wave initiating gamma activity[123] (0.022 m/s), gamma oscillations are actually transmitted much faster (≈ 1 m/s). In this context, my observations would be explained by an enhanced PING mechanism of transmission of gamma from the non-optogenetically manipulated primary ACx to the optogenetically disinhibited dorsal secondary ACx. An obvious implication of this hypothesis is that another GABAergic interneuron type would have to be able to contribute to gamma oscillations instead of PIIs. The accuracy of this hypothesis could easily be evaluated if GABAergic interneurons in the ACx of GAD67-Cre mice would be inhibited by optogenetically stimulating eNpHR in these cells.

SOM^+ cells are a major candidate for an interneuron type able to contribute to the PING mechanism owing to the high connection probability of their reciprocal synaptic contacts to pyramidal cells[203]. These cells have been shown to participate in lateral inhibition[204,205] through a sequence of events comprising cortico-cortical excitation of layer-II/III SOM^+ cells by horizontal projections from layer-II/III pyramidal cells and subsequent inhibition of local layer-II/III pyramidal cells[15,206]. The same anatomical motif has been identified in layer V of the neocortex[207]. This disynaptic inhibition of pyramidal cells by feedback cortical projections[51] is consistent with the delayed input to SOM^+ interneurons observed in the ACx[17]. Evidence put forward by Adesnik and Scanziani (2010) suggests that the recruitment of lateral inhibition is able to generate gamma oscillations. In addition, excitatory synapses on these cells display short-term potentiation, as opposed to short-term depression in PIIs[44–46], which could not only explain the long duration of the time window of elevated gamma power (hundreds of milliseconds), but also the ability of these cells to participate in the generation of high-frequency oscillations.

The discrepancy between my results and those reported by Sohal et al. (2009) could lie in the fact that these authors performed their experiments in anaesthetized mice: anaesthesia has been reported to strongly inhibit neocortical SOM^+ cells and to have only a marginal effect on pyramidal and PV^+ cells (Supplementary Fig. 1 of REF. 15). An additional finding from the present work could be directly explained from a gamma rhythm entrained by SOM^+ interneurons, and from the propagation of the rhythm through horizontal connections: the intriguing period of moderate gamma activity, between the acoustic stimulus and the epoch of highest gamma power (Fig. 5.2D), could result from the initial tonic recruitment of SOM^+-cell-mediated inhibition by strong horizontal input; the succeeding slow wave initiating gamma oscillations[123,139,144] (Fig. 5.4A) could correspond to the excitation of pyramidal cells by weak horizontal input[15]. This hypothesis could as well be straightforwardly tested by inhibiting specifically SOM^+ cells in the ACx of SOM-Cre mice via eNpHR-dependent optogenetic stimulation.

6.1.2.b Gamma wave transmission by pacemaker excitatory cell

Evidence for the existence of pacemaker cells in the neocortex[198–200,202], including the ACx[201], has been provided by a number of studies both in vitro and in vivo. These cells consist mostly of pyramidal cells that, once depolarized above threshold, are able to rhythmically discharge bursts of action potentials at gamma-band frequencies, hence being often referred to as fast rhythmic bursting (FRB) neurons or ‘chattering’ cells. This potent output has been postulated to be necessary for the generation of gamma oscillations, because pharmacologically induced gamma activity is abolished upon blockade of repetitive Na^+-dependent firing[200,201]. Furthermore, two studies have demonstrated in vivo the ability to induce rhythmic activity—restricted to the gamma band—by stimulating pyramidal neurons. Sohal et al. (2009) have observed transient gamma oscillations upon delivering single pulses of optogenetic stimulation to pyramidal cells. Later, Adesnik and Scanziani (2010) have induced a sharp increase specifically in gamma waves by continuously exciting pyramidal cells with monotonically increasing optogenetic stimulation. I suggest that these findings could be attributable to the entrainment of gamma oscillations by FRB neurons. Furthermore, I propose that these neurons could contribute to gamma oscillations when either excited by the acoustic stimulus or disinhibited by optogenetic stimulation of eNpHR in PV^+ cells. A straightforward way of testing this hypothesis could be implemented by inhibiting FRB-neuron burst firing through local perfusion of the ACx with a blocker of persistent Na^+-dependent firing (e.g. phenytoin[200,201]). Such pharmacological manipulation is expected to cancel the magnified gamma power I have observed when optogenetically inhibiting PIIs.

Notwithstanding the intrinsic ability of FRB neurons to present fast rhythmic suprathreshold responses to constant current injection[198–200,202], later evidence has conjectured that FRB neurons could be involved not in the generation of the gamma rhythm, but rather in the amplification of such fast periodic activity generated somewhere else[202]. That argument is founded on the observation that gamma-band deflections in the membrane potential of these cells are not attenuated even when hyperpolarizing them to avoid suprathreshold responses to sensory stimulation. Such finding suggests that FRB cells receive fast rhythmic synaptic input during sensory stimulation. A direct implication of that conjecture is that one should be able to amplify gamma activity by feeding a gamma-modulated excitatory input into pyramidal cells. Cardin et al. (2009) have attempted to optogenetically recruit pyramidal cells at gamma-band frequencies and reported no amplification of the LFP at these frequencies. I suggest that short-term depression at the terminals of pyramidal cells[208] could explain why these authors reported no induction of gamma oscillations upon optogenetically exciting pyramidal cells. The considerably high light intensity used could have recruited pyramidal cells too strongly, leading to the depletion of resources within the terminals of pyramidal cells for high frequencies of stimulation (the recovery time constant is one order of magnitude larger than the period of the gamma rhythm[208]). The results from Adesnik and Scanziani (2010) corroborate my proposition as these authors, in contrast, have successfully induced gamma-frequency activity by tonically exciting pyramidal cells at considerably lower light intensities. To ascertain the accuracy of this hypothesis, one could provide gamma-modulated optogenetic stimulation to pyramidal cells, while inhibiting GABAergic interneurons, and verify if any of several stimulus intensity levels would be able to increase gamma power.

Taking the foregoing findings into consideration, I propose that the following mechanism could underlie my observations: (a) gamma oscillations could be generated at non-optogenetically-manipulated primary areas within the ACx[160]; (b) next, a slow wave of excitation[123] could be transmitted to the manipulated region where it would promptly recruit optogenetically disinhibited FRB neurons; (c) these cells would eventually amplify the gamma wave being conveyed to the overexcited auditory region where they sit.

6.2 Contribution of perisomatic inhibition to learning

In contrast to what was expected from the findings of Letzkus et al. (2011), disinhibition of pyramidal cells in the ACx during CS–US pairing damaged fear learning instead of improving it. This outcome suggests that the US-evoked disinhibition observed by these authors is not sufficient to learn an association during auditory fear conditioning. More importantly, in the present work I have disentangled auditory processing from associative learning by applying a manipulation exclusively during CS–US pairing. As a result, this study offers the first causal evidence that perisomatic inhibition in the ACx is required specifically for associative learning. The use of complex sounds is expected to have contributed to the effect resulting from interfering with the ACx, since this auditory region is critical for fear conditioning to complex stimuli[167,172,209] (despite some contrary evidence for it[210]). There are a number of experimental findings laid out by Letzkus et al. (2011) that could explain the detrimental contribution that disinhibiting the ACx acted on learning in my experiment. These authors (in their Supplementary Fig. 9) identified 2 populations of L2/3 PV^+ interneurons in the ACx in terms of their response to foot shock, namely a large population (88%) of PV^+ cells that is inhibited by the foot shock and a small population (12%) that gets excited in response to the same stimulus. The results being reported in the present work could be explained by unspecific optogenetic inhibition of PV^+ cells, potentially inhibiting not only the fraction of L2/3 PV^+ cells that is naturally excited by the foot shock, but also any other PV^+ interneurons from deeper layers in the ACx that could also get excited by the shock. Moreover, optogenetic inhibition could be too strong and completely abolish the firing activity that, in natural circumstances, remains in the major fraction of PV^+ cells (inhibited upon foot shock delivery). Finally, the same authors (in their Supplementary Fig. 11) show that even L2/3 PV^+ interneurons inhibited by foot shock are briefly (< 20 ms) excited at shock onset. This excitation is most likely countered by the optogenetic inhibition provided in my experiment.

The fear levels here reported during presentation of CS^- are appreciably higher than those observed by Letzkus et al. (2011). This greater fear response is an indicator of fear generalization and could be explained by the fact that the authors used older mice than those employed in the current study[211]. Alternatively, such high fear generalization could suggest that the animals were anxious during the my experiment[163,165,212], probably due to the use of anaesthesia before the beginning of conditioning and reconditioning sessions. Despite the fact that similar levels of fear in response to CS^- have already been reported[165,166], future work should attempt to adopt strategies to reduce anxiety such as lowering the intensity of the shock[213], avoiding the use of anaesthesia before conditioning and mitigating any other stress-inducing sources.

In previous sections, I have described the effect of optogenetically reduced perisomatic inhibition on gamma oscillations. From this effect it follows that the association between CS and US should have been accompanied by an increase in auditory-induced gamma activity. In the light of the evidence for the role that the gamma rhythm plays in sensory processing[60,68,113–117], it is also surprising that promoting gamma oscillations did not facilitate but rather impaired learning. Two implications of this result are the following: gamma oscillations are not sufficient for associative learning in auditory fear conditioning; higher gamma activity does not necessary result in greater learning. To my knowledge, it is the first time that a study evidences an impairment in associative learning following artificially augmented sensory-induced gamma oscillations. These results could be explained by reduction of synchronicity among pyramidal cells, during diminished perisomatic inhibition, rather than overexcitation of the network. A study that offers some support for that hypothesis has shown that the recruitment of PIIs could improve sensory processing, whereas inhibition of pyramidal cells did not have an effect on sensory processing[185].

6.3 Role of the auditory cortex in perception

Fear conditioned mice displayed distinct electrophysiological responses to the CS according to the manipulations they were submitted to. These findings support the involvement of the ACx in perception and recognition of stimulus meaning[11,67,175,214,215], since these changes in neural activity were accompanied by alterations in behaviour associated to sensory processing and learning. However, it is difficult to determine, from the experimental evidence presented here, whether these experience-related differences in neural response indicate that the circuits encoding the association between US and CS lie within the ACx itself or somewhere else. That follows from the fact that, despite restricting the manipulation to the ACx, the resulting modified output of the ACx could have induced plasticity in other circuits controlling expression of fear to the CS. These circuits outside the ACx, undergoing plastic changes during fear conditioning, could conceivably modulate the response of the ACx to the CS. In fact, complementary evidence suggests that these two possible loci of plasticity could coexist.

The hypothesis that the circuit assigning meaning and relevance to complex sounds lies in ACx is supported by previous work, which proposes a role for the ACx that transcends that of merely auditory processing, to also encompass that of auditory categorization[214,216–219]. The short latency of the AEP N15 should not be taken as evidence that responses result exclusively from cortical processing of stimuli directly transmitted across the auditory system to the ACx, because AEPs were computed from a long sequence of closely repeated stimuli. Auditory perception during that epoch of stimulation could in theory be shaped in a number of ways, e.g. by attentional mechanisms[220,221]. Vast evidence indicates that attention modulates both AEPs[222–225] (note that REF. 224 refers to a AEP as ’40-Hz transient response’) and gamma oscillations[226–228] in the neocortex. A few neural circuits[229] have been found to mediate sensory attention, most notably the prefrontal cortex[227,230,231]. Such circuits could have acted on the auditory responses to the CS, in which case the decrease could be interpreted as a reduction in attention. This interpretation would favour the hypothesis involving a circuit, external to the ACx, acting on the perception of complex sounds. The interplay between learning and attention could provide a mechanistic explanation for the lower fear levels displayed in mice whose PIIs were strongly inhibited by optogenetic stimulation. In this context, decreased fear expression, accompanied by lower AEP and gamma amplitude, could be at least partially explained by reduced attention to a CS whose association with the US was made weaker.

The recovery in gamma power observed after reconditioning mice is in line with preceding work showing that repeated fear conditioning increases gamma oscillations induced by the CS[177]. The attenuation of the AEP N15 following impaired learning is likewise supported by previous evidence for the amplification of AEPs after fear conditioning[232,233]. An insufficient number of analysed animals could have been responsible by the absence of a significant difference in fear levels between mice subjected to strong suppression of perisomatic inhibition and those which were not. A similar reason could explain the lack of a difference in the amplitude of AEP N15 between conditioned and reconditioned mice.

6.4 Concluding remarks

Much scientific progress in the last two centuries has contributed to our understanding of the role of inhibition and rhythmic activity in perception and learning. The dominant hypothesis postulates that perisomatic inhibition is *sufficient* for entraining the gamma rhythm in pyramidal cells. I attempted to find conclusive evidence of the *necessity* of perisomatic inhibition for the entrainment of the gamma rhythm. To my great surprise, I found that this type of inhibition not only is not required for the induction of fast rhythms in the brain, but also prevents this activity from growing excessively. This outcome raises many questions, such as which other cortical generators of fast rhythms ought to be investigated? Could other types of inhibition contribute gamma oscillations? If so, then how do the different kinds of inhibition interact with each other? Is inhibition necessary at all for generating fast cortical rhythms or could pyramidal cells be sufficient for producing them?

I have also found that associative auditory learning is influenced by perisomatic inhibition, and that a weakened association results in a reduced response to auditory stimuli. Given that numerous sensory and cognitive processes have been related to the occurrence of gamma oscillations, the fact that an increase in gamma activity—during decreased perisomatic inhibition—did not enhance learning questions the functional relevance of gamma oscillations. Furthermore, the failure to improve the strength of an association between stimuli by enhancing a condition similar to the one that naturally occurs during learning, leads to the question of what are the features of inhibition necessary for sensory learning?

In summary, this work offers a novel perspective on the control of brain rhythms by inhibition and invites to revisit the widespread notion that perisomatic inhibition is at the origin of gamma oscillations. Such reassessment of the cause of gamma oscillations could yield important insight into the relevance of rhythms in cognition. Furthermore, related work could potentially pave the way not only for the treatment of mental disorders associated to abnormal rhythmic activity, but also for strategies to enhance cognitive abilities of normal subjects.

7 Materials and methods

7.1 Materials

Table 7.1 – Devices (sorted by category).

Category	Device	Variety	Model	Manufacturer
Surgical	Stereotaxic frame		Kopf 1900	David Kopf Instruments, Tujunga, USA
	Micromanipulators	Linear Encoders	Acu-Rite SENC 50 and 200S	Heidenhain Corporation, Schaumburg, Germany
	Isoflurane vaporizer		Vapor 19.3	Drägerwerk AG, Lübeck, Germany
	O_2 concentrator		EverFlo	Respironics Deutschland, Herrsching, Germany
	Heating pad		ThermoLux	Witte + Sutor GmbH, Murrhardt, Germany
	Intracerebral injection kit	Syringe, stainless steel needle	7635-01 and 7803-05	Hamilton Bonaduz AG, Bonaduz, Switzerland
	Precision pump	Programmable, syringe driver	AL-1000	WPI Germany GmbH, Berlin, Germany
Acoustic	Speaker system	Free-field electrostatic speaker, driver, power supply	ES1, ED1 and ZB1PS	Tucker-Davis Technologies, Alachua, USA
	DAC	USB-powered audio interface	Quad-Capture UA-55	Roland Germany GmbH, Nauheim, Germany
Electrophysiological	Amplifier system	Wireless 4-channel headstage, receiver and USB interface	W4-System	Multi Channel Systems MCS GmbH, Reutlingen, Germany
	Impedance meter and tuner		Ωmega-Tip-Z	WPI Germany GmbH, Berlin, Germany
Optogenetic	Optical power meter	Integrating-sphere-based design	S140C and PM100D	Thorlabs GmbH, Dachau, Germany
	Optical coupler	2×2 male–male FC/PC to ferrules	FCMH2-FCF	
	Lasers	Blue (473 nm), DPSS	Ike-473-100-OF	IkeCool Co., Anaheim, USA
		Blue (473 nm), LD	LDM laser series	LASOS Lasertechnik GmbH, Jena, Germany
		Green (561 nm), DPSS	YLK 6175 TFM01 laser set	
	Beam combiner	Mini cube, wavelength division	DMC_1×2w_473/532_FC	Doric Lenses Inc., Quebec, Canada
	Beam splitter	Micro splitter, intensity division	DMS_1x2i_200/220/900-0.37_FC_ZF2.5(F)	
	Rotatory joints	1×1 optical	FRJ_1×1_FC-FC	
		1×1 optical and electrical	HRJ-OE_FC-FC_12_HARW	
Behavioural	Camera	IP, surveillance	TL-SC3130	TP-Link Deutschland GmbH, Hofheim am Taunus, Germany
Perfusion and IHC	Pump	Peristaltic	2115 multiperpex	LKB, Bromma, Sweden
	Vibratome	Analogue	D.S.K. DTK-1000	Dosaka Em Co. Ltd., Kyoto, Japan
Imaging	Microscope system	Confocal laser scanning	LSM710 and Axio Examiner.Z1	Carl Zeiss AG, Oberkochen, Germany
Information technology	Personal computers	Standard		
	Microcontrollers	Single-board	UNO R2 and R3	Arduino LLC
Miscellaneous	Electronic components			Omega electronic GmbH, Freiburg, Germany

Table 7.2 – Software.

Name and version	Purpose(s)	Developer
Arduino 1.0.5/1.6.6	Equipment synchronization, all-purpose device controller	Arduino LLC
Windows Media Player 12.0		Microsoft Corporation
VLC media player 2.0.0/2.2.1	Video acquisition	VideoLAN
Matlab 8.3.0.532 (R2014a)	Programming all-purpose device drivers for equipment synchronization, development and processing of data-analysis and graphic-design algorithms	The MathWorks, Inc.
MC_Rack 4.5.3/4.6.2	Electrophysiological data acquisition	Multi Channel Systems MCS GmbH, Reutlingen, Germany
MC_DataTool 2.6.10	Electrophysiological data format conversion	
Zen 2012 SP1	Histological image acquisition	Zeiss
ImageJ 1.50g	Image processing	Wayne Rasband, NIH, USA
Inkscape 0.91	Graphic design	inkscape.org

Table 7.3 – Consumable mechanical, electrical and optical components (sorted by category).

Category	Purpose(s)	Component	Catalogue #	Manufacturer
Surgical	Implant cement	Denture acrylic	Paladur 64707938 and 64707957	Heraeus Kulzer GmbH, Hanau, Germany
	Implant anchoring to skull	Stainless steel jeweller's screws	DIN 84 A2 M1×2	SAM Screws and more GmbH, Burscheid, Germany
	Non-compressible injection medium	Medicinal grade white oil	Marcol 82	Exxon Mobil Corporation, Irving, USA
Electrophysiological	Tetrode	Tungsten wire, Formvar coating, 55-gauge	100211	California Fine Wire Co., Grover Beach, USA
		Polyimide tubing	0.007" ID	Amazon.com, Inc.
	Microelectrode	Stainless steel wire	SS31605	WPI Germany GmbH, Berlin, Germany
	Electrical and optical insulator	Black opaque nail polish	p2 Color Victim	p2 Kosmetik GmbH, Wien, Austria
	Headstage connector	Male pin header	SLR 1 025 Z	Fischer Elektronik GmbH & Co. KG, Lüdenscheid, Germany
Optogenetic	Optical implant	Multimode optical fibre	FT200EMT	Thorlabs GmbH, Dachau, Germany
		Ceramic ferrules	CF230-10	
		Fast-curing epoxy adhesive	UH45705	UHU GmbH & Co. KG, Bühl, Germany
	Optical insulator	Black pastel	17 099 069 D	H. Schmincke & Co. GmbH & Co. KG, Erkrath, Germany

Table 7.4 – Pharmacological substances (in alphabetical order).

Generic/trade name (concentration and chemical name)	Purpose	Catalogue #	Distributor/supplier
Buprenorphine/Temgesic (0.3 mg/mL)	Analgesic		Reckitt Benckiser Healthcare (UK) Ltd., Hull, UK
Isoflurane/Forene (100% 1-chloro-2,2,2-trifluoroethyl difluoromethyl ether)	Anaesthetic for chronic procedures	B506	AbbVie Deutschland GmbH & Co. KG, Ludwigshafen, Germany
Urethane (99% ethyl carbamate)	Anaesthetic for terminal procedures	U2500	Sigma-Aldrich Chemie GmbH, Taufkirchen, Germany
VISMED GEL (0.30% sodium hyaluronate)	Eye drops		TRB Chemedica AG, Haar, Germany

Table 7.5 – Recombinant adeno-associated viruses (rAAVs), antibodies and fluorescent dyes.

Description	Specification	Dilution	Laser λ (nm)	Catalogue #	Distributor/supplier
rAAV	pAAV-double floxed-eNpHR-EYFP-WPRE-pA		488	20949	Addgene
	pAM-FLEX-GFP				Murray et al. (2011)
Primary polyclonal antibody	Rabbit anti-parvalbumin	1:1000		PV 27	Swant, Marly, Switzerland
	Guinea pig anti-GFP			132 004	Synaptic Systems GmbH, Göttingen, Germany
Secondary antibody	Goat anti-rabbit Cy3		543	111-165-003	Dianova GmbH, Hamburg, Germany
	Goat anti-guinea pig Alexa Fluor 647		633	Invitrogen A-21450	Thermo Fisher Scientific Inc., Rockford, USA
Fluorescent dye	DAPI dihydrochloride		405	D9542	Sigma-Aldrich Chemie GmbH, Taufkirchen, Germany
	Rhodamine (in latex retrograde-tracer microspheres)	No dilution used	543	Red RetroBeads IX	Lumafluor Inc., Durham, USA

Table 7.6 | Aqueous solutions prepared in-house (in alphabetical order). Milli-Q water used as solvent.

Description	Purpose(s)	Content
1% acetic acid	Odorant, disinfectant	1% v/v acetic acid
Artificial cerebrospinal fluid (ACSF)	Craniotomy humectant, urethane-anaesthesia excipient	125 mM NaCl, 25 mM $NaHCO_3$, 2.5 mM KCl, 1.25 mM NaH_2PO_4, 25 mM glucose, 2 mM $CaCl_2$ and 1 mM $MgCl_2$
4% depolymerized paraformaldehyde (PFA)	Tissue fixative in transcardial perfusions and whole-brain resection	4% m/v PFA in PBS
20% mannitol	Viral transduction enhancer	20% m/v mannitol in ACSF
Mowiol solution	IHC mounting medium	6.0 g glycerol, 2.4 g Mowiol 4-88, 6.0 mL water, 12.0 mL tris buffer
0.15 M phosphate-buffered saline (PBS)	Mannitol-solution excipient, blood-draining medium in transcardial perfusions, stock buffer solution for various purposes in staining	0.15 M NaCl in 0.1 M PB
0.4 M phophate buffer (PB)	Stock buffer solution for preparing PBS and 4% depolymerized PFA	0.4 M NaH_2PO_4 added to 0.4 M Na_2HPO_4 until a pH of 7.35 is reached
0.2 M tris buffer	Stock buffer solution for preparing Mowiol solution	1 M HCl added to 0.2 M tris until a pH of 8.5 is reached

Table 7.7 | Chemicals (in alphabetical order).

Name	Purpose(s)	Formula	Catalogue #	Distributor/supplier
70% ethanol	Odorant, disinfectant	C_2H_6O	T913.3	Carl Roth GmbH + Co. KG, Karsruhe, Germany
Gold non-cyanide	Tetrode plating solution			Neuralynx Inc., Dublin, Ireland
Isopropanol	Optical cleaner	C_3H_8O	6752.1	Carl Roth GmbH + Co. KG, Karsruhe, Germany
Normal goat serum	IHC blocking reagent		005-000-121	Dianova GmbH, Hamburg, Germany
Paraffin wax	Craniotomy sealant		327204	Sigma-Aldrich Chemie GmbH, Taufkirchen, Germany
Triton-X100	IHC permeabilization reagent	$C_{14}H_{22}O(C_2H_4O)_n$	X100-100ML	

7.2 Methods

7.2.1 Animals

Maximization of reproducibility of behavioural results entailed the restriction of mouse usage to solely male animals so as to avoid interference of the oestrous cycle with behaviour[235]. 14 male PV-Cre mice (5–14-week old; used in electrophysiological and behavioural experiments; The Jackson Laboratory, http://jaxmice.jax.org/strain/008069.html) and 2 female PV-Cre mice (11–12-week old; used in retrograde tracer experiment) were housed under a 12 h light/dark cycle with food and water *ad libitum*. Every mouse was housed with at least one cage mate (that was always a same-gender littermate) in order to avoid additional anxiety caused by isolation[236,237]. All procedures involving the use of animals were carried out in agreement with national legislation (Tierschutzgesetz der Bundesrepublik Deutschland 1972 §7, 7a, 8, and 9 [2015]).

At any given day, all mice used in ongoing bioacoustic experiments would be brought together to the experimental room 30 min to 3 hours before the end of the light phase. Animals were allowed to habituate to the room, inside of their cages, for at least 30 min before starting any experiment or handling procedure. Prior to experimenting with a mouse for the first time, the experimenter would habituate the animal to handling 2–5 times (typically 5 times) for 1–5 days (usually 5 days) by allowing it to walk for a few minutes on the experimenter's hands. During bioacoustic experimentation, just one mouse at a time would be inside the operant-conditioning chamber; all the remainder mice and the experimenter would stay outside the sound booth (for details on the set-up of the acoustic equipment see Sect. 7.2.4.a).

7.2.2 Solutions

Aseptic employment of solutions in surgical procedures was safeguarded by partially sterilizing solutions with a clean filter prior to applying them to brain tissue. ACSF solution was used for both wetting craniotomy sites and preparing urethane-based anaesthesia. When used in craniotomies, the solution was filter sterilized. PBS solution was used both for preparing mannitol-based vehicle solutions (for virus injections) and for preparing the circulatory system of mice for transcardial perfusion with depolymerized PFA solution. 20% mannitol solution was prepared by briefly assisting with heat the dissolution of mannitol in PBS and then filter sterilizing it. 4% depolymerized PFA solution was prepared through the heat-assisted dissolution of PFA in Milli-Q water (at 60–70 °C) and subsequent addition of 0.3 M PBS. Solutions were stored at 4 °C and in part prepared by Karin Winterhalter and Kerstin Semmler.

7.2.3 Surgery

Precise intracerebral injections and implantations were executed by keeping mice fixed, during the whole surgical procedure, in a stereotactic frame (Kopf 1900) under isoflurane anaesthesia (animals were kept warm on a heating pad with 6 W thermal output). Anaesthesia was initially induced with 3% isoflurane (in pure O_2) by inhalation and maintained on 0.5–1.5% throughout the surgery. After anaesthesia induction, mice received a subcutaneous injection of analgesic (buprenorphine, 0.01 mL per 10 g of body weight; Temgesic, Reckitt Benckiser). Prior to performing an incision in the skin above the head and exposing the skull, pain reflexes were confirmed to have been abolished by the anaesthesia, the fur around the incision site was shaved and the skin, surgical tools and gloves disinfected with a 70% ethanol solution. The position of the skull was adjusted consistent with the following specifications: bregma and lambda were in the same plane (error no greater than 0.1 mm in the dorsoventral axis and 0.2 mm in the mediolateral axis); the anatomical horizontal plane was perpendicular to the dorsoventral axis (error between the two points, on the upper surface of the skull, 2 mm lateral to bregma no greater than 0.1 mm in the dorsoventral axis). Surgical marking and interventions were performed with the assistance of a mouse brain atlas[238] (for selecting the coordinates) and 3 individual micromanipulators (one per anatomical axis; Acu-Rite SENC 50). In order to have access to the brain and to implant anchoring screws in the skull, small holes (1–1.5-mm diameter) were drilled into the bone with an electric drill equipped with round drill bits (1-mm diameter). Once drilling was complete, the exposed surface of skull (of mice receiving an implant) was scratched with the drill to enhance adhesion of the dental cement. The holes in the skull used to access the brain further required total removal of the thinned bone flap and dura mater. These craniotomy sites were kept wet with ACSF and, after completion of intracerebral injections and implantations, closed with melted wax (53–57-°C melting point). Intracerebral injections were executed with the aid of a manual syringe (needle with 0.21-mm outer diameter; catalogue # 7803-05, Hamilton) fixed to the stereotaxic frame by the micromanipulators. Before conclusion of surgery, those mice used for tracer injection, which did not receive any implant, had their surgical wounds closed and covered with contact adhesive.

7.2.3.a Virus injection

For optically controlling PV^+ cells, 10 mice with 5–7 weeks of age were bilaterally injected (for 18–30 min; 7635-01 and 7803-05, Hamilton) with 1 µL of rAAV used to deliver a plasmid for conditional, Cre-dependent expression of eNpHR2.0[66,118] (pAAV-double floxed-eNpHR-EYFP-WPRE-pA; catalogue # 20949, Addgene) into the ACx (2.6 mm posterior of bregma, 4.1 mm lateral of midline; tip of syringe lowered vertically 1.2–1.25 mm below surface of the skull; Fig. 5.1A,B). Validation of this optogenetic tool has been previously realized in the same mouse line by my colleagues Elgueta, Kohler and Bartos (2015, their Fig. 2), who demonstrated PV^+ cells to be inhibited during light stimulation of eNpHR. The same methodology was used for obtaining the sham-injection control group of 4 mice injected bilaterally with a conditional rAAV allowing for expression of GFP[234] (pAM-FLEX-GFP) in PV^+ interneurons in the ACx. To maximize transduction efficiency and spread, viruses were co-infused with sterile mannitol solution[239] (20% mannitol in PBS), both in the group of animals expressing eNpHR (2 parts of virus to 1 part of mannitol solution) and in the sham control group (1 part of virus to 1–1.5 parts of mannitol solution to 1–1.5 parts of PBS). Experiments were performed after 3–5 weeks of expression.

7.2.3.b Implantations

To record LFPs and provide optogenetic stimulation, several electrical and optical components were chronically fixed to the skull of mice. The implantation procedure was carried out during the same surgical intervention as virus injections, immediately after these. As a preparation for implantations, a total of 7 small holes were drilled into the skull of the animal according to the following arrangement and requirements: 4 burr-holes (leaving mostly intact the dura mater) near the rim of the skull (2 into both parietal bones and 2 into the interparietal bone over the cerebellum) for implanting 4 minute jeweller's screws (1-mm diameter) used to secure the implant; 2 of these screws were also used as reference and ground electrodes (screws respectively on the left and right side of the interparietal bone); 2 craniotomies above the dorsal part of both auditory cortices (2.6 mm posterior of bregma, 4.1 mm lateral of midline) for implanting the optrode (left hemisphere; tip of tetrode lowered vertically 1.3 mm below surface of the skull; Fig. 5.1C–F) and the optical implant (right hemisphere; tip of optical fibre lowered vertically 0.9 mm below surface of the skull); one craniotomy over the left primary visual cortex (3 mm posterior of bregma, 2 mm lateral of midline) for implanting an electrode in the MGB (tip lowered vertically 3 mm below surface of the skull; Fig. 5.5C,D). Electrical components were connected to a 6×1 male pin header (via soldered copper wires) implanted vertically, along the midline, above the skull. Implants were fixed with dental cement (Paladur, Heraeus) and, in the case of the optrode and optical implant, the dental cement incorporated 2% of black pastel to darken the implant and contain most of light escaping the brain.

7.2.3.c Tracer injection

For labelling neurons in the MGB projecting to the ACx (Fig. 5.5B) mice received, at 11 weeks of age, a unilateral injection (for 15 min) of 1.5 μL of retrograde tracer (Red RetroBeads IX, Lumafluor) into the right ACx (2.7 mm posterior of bregma, 4.5 mm lateral of midline; tip of syringe lowered perpendicularly to the skull, 1 mm below its surface; Fig. 5.5A). The injection was performed with a glass pipette and the assistance of a programmable syringe pump (AL-1000, WPI). The pipette was connected to the pump through oil-filled tubing for improved control over the injected volume. Animals were sacrificed 5 days later.

7.2.4 Acoustic stimulation

7.2.4.a Equipment set-up

To maximize reproducibility of results, several measures were taken to reduce interference with the acoustic stimulation. Experiments were carried out in a small operant-conditioning chamber (0.25-m inner diameter, 0.5-m height; Fig. 7.1) placed inside a large sound booth (i.e. a sound-attenuated semi-anechoic chamber). Both chambers were especially designed and built with the purpose of ensuring a quiet acoustic environment. The sound booth was made of wooden double stud walls and ceiling filled with batt insulation to attenuate sounds coming from the exterior[240]. Its interior was lined with acoustic foam for attenuating reverberation. The operant-conditioning chamber was built from polyvinyl chloride (PVC) piping and was also lined with foam to attenuate reverberation. On top of it was installed an electrostatic speaker (4–110-kHz bandwidth; model ES1 from TDT) to deliver free-field high-frequency acoustic stimulation to freely moving mice.

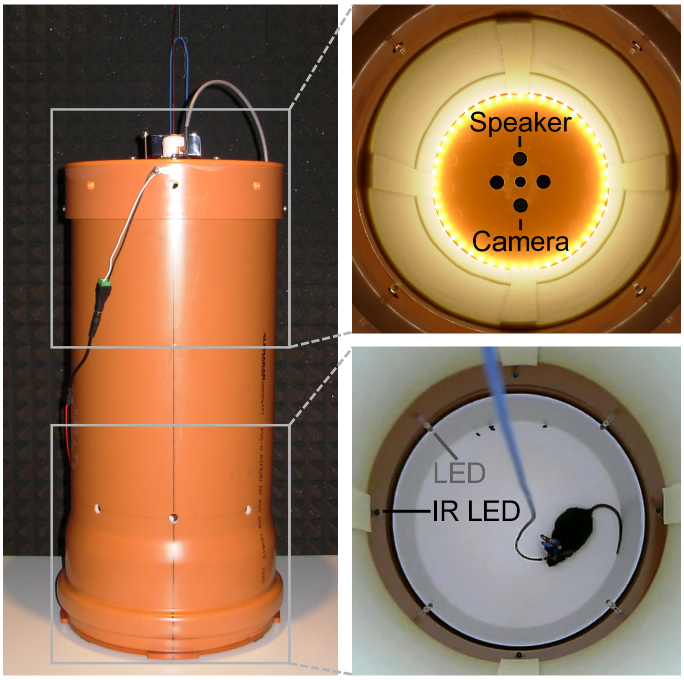

Figure 7.1 | Experimentation in a quiet acoustic environment. Left | Side view of the custom-made operant-conditioning chamber inside the sound booth. Top right | Perspective of the built-in speaker and camera at the top of the chamber. Bottom right | Snapshot of the arena taken with the built-in camera during a non-behavioural experimental session (see next section). The mouse has an optical patch cable connected to the optrode implanted in the head (see Sect.7.2.6.c). The infrared (IR) LEDs allow temporal registration of video frames (see Sect. 7.2.7.a).

Highly precise sub-millisecond synchronization between acoustic stimulation and the rest of the experimental apparatus was achieved by including triggers in the stereophonic track being played back (Fig. 7.2; Windows Media Player, Microsoft Corporation). The signal encoded in this audio file, after conversion to an analogue signal (by an audio interface DAC with 192-kHz playback rate; Quad-Capture, Roland), would be split into its two constituent channels: one channel would contain the acoustic stimuli, which would be played back by the speaker system; the other channel would contain the triggers that would be fed into a downstream microcontroller (Arduino Uno), used as an all-purpose device controller able to interpret the triggers (via pulse-amplitude modulation) and generate TTL pulses for activating other equipment. The runtime of the interpreter (period between input and output) is 0.2 ms (as measured on an oscilloscope), i.e. it takes 0.2 ms to read a trigger and produce the corresponding TTL pulse. The amplitude of the acoustic signal (i.e. the volume) was controlled by software (in terms of the root mean square [RMS] amplitude of the signal encoded in the 8-bit WAV audio file containing the stimuli) and all hardware was set to maximum gain.

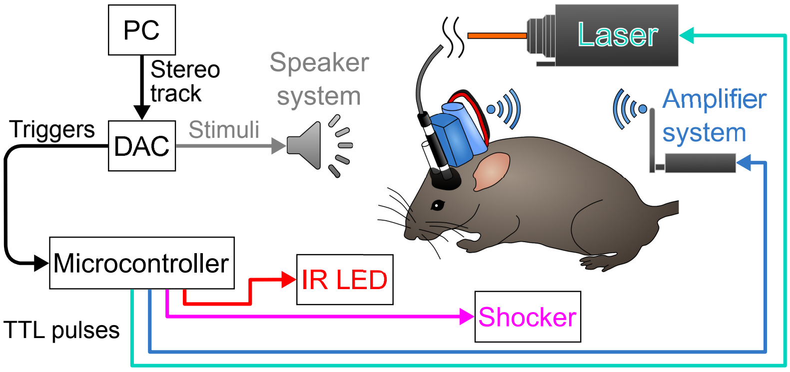

Figure 7.2 | Precise timing and synchronization of experimental devices. A custom-made system safeguarded the correct timing of acoustic stimulus delivery and device activation by including triggers in the stereo track played back by a personal computer (PC). After conversion of the stereo track to an analogue signal by a digital-to-analogue converter (DAC), the acoustic part of the signal was transduced by the speaker system and the triggers were interpreted downstream by a microcontroller that was used to activate the rest of the experimental apparatus using transistor–transistor logic (TTL) pulses.

7.2.4.b Protocols

Well-defined acoustic stimuli were generated by custom-made synthesizing algorithms running on Matlab. Stimuli consisted of broadband sounds (5–80-kHz bandwidth; 5-ms rise and fall) covering most of the hearing range of mice[125–127]. For each animal, three protocols of acoustic stimulation were applied (Fig. 7.3). The first protocol (full description in Fig. 5.6E) was used on the first, third and seventh days of experimentation, during the test sessions of the behavioural experiment. It comprised stimulation with 0.5-s exponential chirps (i.e. sinusoidal waves whose frequency increases or decays exponentially over time; Fig. 5.6B): one of increasing acoustic frequency (up-chirp) and another with the reverse frequency modulation (down-chirp). The protocol consisted of 4 epochs of stimulation with the down-chirp followed by 20 epochs with the up-chirp. Epochs were evenly spaced by 5.5 s and each one would include 30 repetitions of the stimulus at 1 Hz (0.5 s inter-repetition interval). The second protocol was applied only on the first day of experimentation, after the first protocol, and consisted of the only non-behavioural experimental session. This protocol involved 5 experimental conditions (3 non-silent plus 2 silent conditions; see Sect. 7.2.6.c); each non-silent condition would comprise stimulation with three 50-ms stimuli (with flat power spectral density and equal RMS amplitude). Most of the data reported from this non-behavioural experiment were obtained during stimulation with Gaussian white noise (0.2 RMS amplitude on a dimensionless scale from -1 to 1; clipped for values above this range; Fig. 5.2B); in addition, linear up- and down-chirps (linear change of frequency with time) were delivered. Conditions and stimuli were applied in a pseudorandom order and every stimulus was repeated 20 times for each non-silent condition (inter-stimulus/condition interval drawn from a continuous uniform distribution from 9 to 11 s). The third protocol (fully described in Fig. 5.6A,D) was employed on the second and sixth days of experimentation, during the fear-conditioning sessions of the behavioural experiment. It consisted in providing the two stimuli from the first protocol alternately in the following way: each 30-repetition epoch of stimulation with the up-chirp would be followed by an epoch with the down-chirp (inter-epoch interval drawn from a continuous uniform distribution from 60 to 140 s).

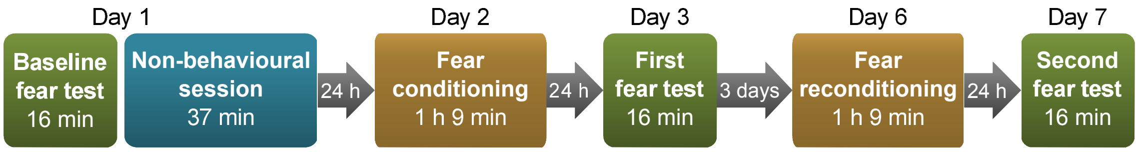

Figure 7.3 | Mice were submitted to several distinct sessions of experimentation. The full experimental protocol comprised a week of data acquisition serving both a behavioural experiment involving auditory fear conditioning and a non-behavioural experiment involving solely acoustic and light stimulation.

In all experiments, stimuli were delivered in a free-field acoustic environment[240] according to the following equation:

$$d > \frac{1}{4} \times \lambda = \frac{1}{4} \times \frac{v_s}{f}, \tag{7.1}$$

where *d* is the distance between the speaker and the mouse ear, approximately 0.5 m, which is greater than ¼ the wavelength λ of the lowest stimulus frequency *f*, 5 kHz, i.e. *d* is greater than ¼ the velocity of sound v_s (≈ 343 m/s) divided by *f*, which results in 0.017 m. The sound pressure level was set to 51 dB during behavioural sessions and 49 dB during the non-behavioural session.

7.2.5 Electrophysiological recordings

7.2.5.a Implant assembly and set-up

Minimization of brain-tissue damage caused by the intracortical electrode was carried out by employing custom-built minute tetrodes (4 individually insulated, 14-µm diameter tungsten wires). Tetrodes were fabricated according to the method described by Liao, Tsai, Yen, and Cheng (2011) and were contained in polyimide tubing (178-µm inner diameter) that was attached to the optical fibre (see Sect. 7.2.6.a) for improved rigidity. For every tetrode, only 3 wires were connected to a miniature printed circuit board (used to ease soldering these wires to copper wires, in turn used as tiny patch cables). The impedance of these 3 wires was lowered to a range of 0.15–0.35 MΩ by individually gold-plating the tip of them (Ωmega-Tip-Z, WPI). The microelectrode used to record neuronal signals from the MGB consisted of stainless steel wire (125-µm diameter). The microelectrode (and in one mouse also the tetrode) were painted with nail polish to provide an electrical insulation (in the case of the microelectrode) and to virtually eliminate light-induced artefacts (see Sect. 7.2.6.a). Surgical implantation procedures are described in Sect. 7.2.3.b.

7.2.5.b Equipment set-up

To prevent contamination of the electrophysiological signal with electrical noise (especially 50 Hz mains hum), both the sound booth and the operant-conditioning chamber incorporated Faraday cages. For that purpose, the interior of the sound booth was lined with a metallic aviary mesh (below the acoustic foam) and the operant-conditioning chamber, on the outside, was completely covered with aluminium foil (not shown in Fig. 7.1). The Faraday cages and the power source of the electrical equipment (i.e. speaker, camera, light-emitting diodes [LEDs]) was connected to the mains ground.

7.2.5.c Protocols

Extracellular recordings in freely behaving mice were achieved with a light-weighted wireless headstage (3.7 g; gain 100; W4-System, Multi Channel Systems). Neuronal activity was acquired on MC_Rack software (Multi Channel Systems) and digitalized at 20 kHz (with 16-bit resolution). Peristimulus epochs were recorded exclusively during the fear-test and non-behavioural sessions (Fig. 7.3) (corresponding, respectively, to the first and second protocols described in Sect. 7.2.4.b). Recoding epochs covered the periods from -0.4–0.55 and -0.5–1 s (relative to sound onset or to the equivalent moment during a silent optogenetic-stimulation repetition) in the fear-test and non-behavioural sessions, respectively.

7.2.6 Optogenetics

7.2.6.a Implant assembly and set-up

Delivery of light for optogenetic stimulation of eNpHR in PV^+ cells was achieved through optical fibres (200-µm core diameter, 0.39 NA; FT200EMT, Thorlabs). Optical fibres were contained in ceramic ferrules (2.5 mm diameter; CF230-10, Thorlabs) used to connect the implanted optical fibre to the laser light source. The resulting combination of fibre and ferrule constituted the optical part of the optrode and the optical implant contralateral to the optrode (see Sect. 7.2.3.b). After assembly, the optical attenuation of every optical component was tested with a blue laser (473-nm wavelength, DPSS laser; Ike-473-100-OF, IkeCool) and an optical power meter (S140C and PM100D, Thorlabs) to ensure a transmittance greater than or equal to 80%. Light-induced artefacts in recorded electrophysiological signals[195] were virtually eliminated by painting the electrodes with black opaque nail polish.

7.2.6.b Equipment set-up

Precisely timed and modulated light stimulation was delivered through custom-made laser controllers. The blue laser (473-nm wavelength, laser diode; LDM laser series, LASOS) was directly turned on by a TTL pulse generated by a fast microcontroller (see Sect. 7.2.4.a); its light intensity was modulated by an analogue signal generated by an electrical circuit especially devised for this purpose. This analogue signal was created in two steps: first, the amplitude of the signal would be encoded in a digital signal via pulse-width-modulation (980-Hz duty cycle); second, this pulsing signal would pass through a low-pass filter (with a series resistor–capacitor circuit) conceived to smooth the signal amplitude. The green laser (561-nm wavelength, DPSS laser; YLK 6175 TFM01, LASOS) was activated (1-ms turn-on time, 10-ms turn-off time) and modulated by a single analogue signal (also generated from a low-pass filtered pulse-width-modulated signal), created by a controller activated by TTL pulses.

7.2.6.c Protocols

To study the effect of optogenetically inhibiting PV$^+$ interneurons on both auditory-induced and ongoing gamma activity (non-behavioural experiment), five stimulation conditions were tested (Figs. 5.2 and 5.3): without light stimulation and with only acoustic stimulation (*acou* condition); with acoustic stimulation and either control blue-light (*acou + optog*$^-$ condition) or green-light stimulation (*acou + optog*$^+$ condition); without acoustic stimulation and with only either control blue-light (*optog*$^-$ condition) or green-light (*optog*$^+$ condition) stimulation. Each of these conditions was tested 20 times (for conditions with acoustic stimulation, each sound was tested 20 times; see Sect. 7.2.4.b). Stimulation was shuffled such that the distinct conditions and sounds were presented in pseudorandom order. Every repetition of light stimulation (ipsilateral to optrode) lasted 0.5 s (when delivered together with a sound, it started 50 ms before sound onset). In fear-conditioning and fear-reconditioning sessions, 6 s of bilateral light stimulation would be provided commencing 25 ms before foot shock (Fig. 5.6A). Stimulation intensity was set to approximately 9 mW (radiant power measured at the tip of the patch cable used to connect the optical components of the implants to light source), corresponding to irradiances greater than 60 and 7 mW/mm^2, respectively, at the optical-fibre–brain interface and close to the LFP recording site (corrected for attenuation by optical implant and according to predicted irradiance value; http://web.stanford.edu/group/dlab/cgi-bin/graph/chart.php). Connection of optical patch cables to implants required to briefly (< 1 min) anaesthetize the animal with isoflurane and to wait 15 min for it to recover before resuming experimentation. Excessive tension in the patch cable and mouse was released through an optical rotatory joint (FRJ_1×1_FC-FC and HRJ-OE_FCFC_12_HARW, Doric) connected to the patch cable above the operant-conditioning chamber.

7.2.7 Behaviour

7.2.7.a Equipment set-up

Well-regulated foot shocks were automatically delivered to mice, during fear conditioning, using a custom-built shock controller (shocker; Fig. 7.4A) activated by TTL pulses (generated by a fast microcontroller; see Sect. 7.2.4.a). The shocker was designed to provide reproducible shocks of 0.65 mA of current (up to 320 kΩ of body resistance as measured with a multimeter; Fig. 7.4B) regardless of the way how the animal touches the electrified metallic bars. For that purpose, the shocker incorporated a current source (controlled by a bipolar junction transistor [BF421], stabilized by a Zener diode [BZX79C12] and powered by a 240-V AC-to-DC unregu-

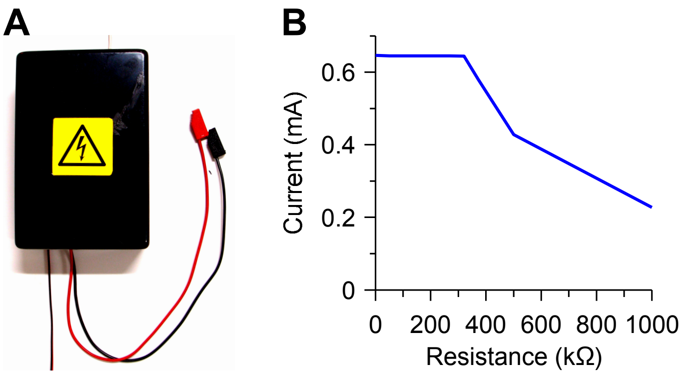

Figure 7.4 | Reproducible foot shock delivery. A | Custom-built controller used to provide scrambled foot shocks to mice during fear conditioning. **B** | The internal current source provided constant current up to 320 kΩ of body resistance.

lated power supply [custom-made]). Shocks consisted of bipolar scrambled waves (40-Hz wave with three-state return-to-zero binary coding) originated by combining two pulse waves (8.3-ms pulse width), one positive and other negative, out-of-phase by half a period.

Videos of the mouse arena (at the bottom of the operant-conditioning chamber) were streamed on VLC media player (VideoLAN) and recorded in the MP4 format (H.264 standard). To provide time stamps for measuring the mouse movement from video recordings (see Sect. 7.2.10.e), infrared (IR) LEDs were installed inside the operant-conditioning chamber (Fig. 7.1), within the field of view of a camera able to detect light in the IR range (TL-SC3130, TP-Link). IR LEDs were turned on simultaneously with stimulation devices (speaker, laser and shocker) and their light was invisible to the experimenter, and by extension, to mice[134,135]. The operant-conditioning chamber was built with a detachable, washable base that was painted white to enhance the contrast to the dark fur of mice, thus facilitating automated motion detection. This chamber was also equipped with two sources of white light of different intensity to accentuate the perceptual difference between experimental contexts (see next section). Illumination could either be diffused light (provided by an LED strip placed at the top) or direct light (delivered by 4 individual LEDs placed at the bottom, close to the animal, pointed at the centre of the arena).

7.2.7.b Protocol

A differential auditory fear conditioning experiment was devised to study the role of PV^+ interneurons in behaviour. Two acoustic stimuli (see Sect. 7.2.4.b for specifications of the stimuli and acoustic protocols) were differently conditioned to a foot shock (Fig. 5.6A): in parallel with the last of 30 repetitions of one of these conditioned stimuli (CS^+), a foot shock was delivered (for 1 s); subsequently, with variable delay, 30 repetitions of other conditioned stimulus (CS^-) would be presented without being paired to any shock. Together with the foot shock, light stimulation was delivered bilaterally (for 6 s) to optogenetically inhibit PV^+ cells in the ACx and control the pairing of CS^+ with US. Mice were submitted two 5 sessions of experimentation in accordance with the following protocol (Fig. 5.6C): (a) on the first day, mice were pretested for native fear responses to acoustic stimulation; (b) on the following day (after 24 ± 5 h) mice were conditioned to fear; (c) one day later (after 24 ± 5 h) the fear response to the each CS was tested; (d) three days later the experiment was resumed and mice were reconditioned to fear; (e) lastly, one day later (after 24 ± 5 h), the CS fear response was once more retrieved. The experiment followed a counterbalanced design whereby half of the mice were stimulated with green ($optog^+$) and blue light ($optog^-$), respectively during the fear conditioning and reconditioning sessions, whereas the remainder mice (cage mates) were stimulated in the reversed order (first $optog^-$ and then $optog^+$). During fear conditioning and reconditioning sessions, each epoch of 30 repetitions of CS^+ and CS^- was presented 15 times alternately (Fig. 5.6D). Fear test sessions comprised 4 silent epochs for measuring baseline freezing levels, followed by 4 CS^- epochs and 20 CS^+ epochs (Fig. 5.6E).

To reduce fear generalization to the context, two contexts were used (Fig. 5.6C): fear test sessions were performed in context A and fear conditioning and reconditioning sessions were carried out in context B. Context A comprised a round arena, with smooth floor, illuminated by diffused light and was always washed with tap water and cleaned with 1% acetic acid; context B consisted of a square arena, with a floor made of metallic bars, illuminated by direct light and was always washed with deionized water (to reduce short circuits) and scented with 70% ethanol. During an experimental sessions, mice would not be put back in contact with their cage mates to avoid communication of stress across mice.

7.2.8 Fixation and staining

Standard tissue fixation and staining techniques were employed for preparing the brain of mice for microscopic examination. Mice were deeply anaesthetized by brief exposure to isoflurane followed by intraperitoneal injection of urethane (as 10% m/v urethane in ACSF; 0.2 mL per body 10 g of weight). Prior to initiating the surgery, pain reflexes were confirmed to have been abolished by the anaesthesia. After performing an incision in the abdomen and thorax, the heart was exposed and a needle, connected to a peristaltic pump (2115 multiperpex, LKB), was inserted in the left heart. Next, the animal underwent transcardial perfusion with 2 solutions (8-mL/min volumetric flow rate): first, the blood was drained from the circulatory system with PBS (for 1 min) through large cuts made in the liver; second, the whole body was perfused (for 13 min) with fixative (4% depolymerized PFA). Subsequently, the animal was decapitated, the skull was opened and the brain resected and stored in fixative overnight. Afterwards, the brain was transferred to PBS and coronal slices (50-μm thick) were taken from the MGB and ACx with a vibratome (DTK-1000, D.S.K.). On the same day, slices were treated with various PBS-based solutions according to the following protocol: (a) slices were permeabilized in 0.4% TritonX-100 (for 30 min, at room temperature [RT]), (b) then blocked in 0.2% TritonX-100 and 4% normal goat serum (NGS, for 30 min, at RT) and (c) incubated in 0.1% TritonX-100 and 2% NGS together with the primary antibodies (overnight, at 4°C). On the next day, slices were again treated with several PBS-based solutions according to the following protocol: (a) slices were washed in 1% NGS (3 times for 10 min each), (b) then incubated in 1.5% NGS together with the secondary antibodies (for 2–2.5 h, at RT), (c) washed yet again with 1% NGS (2 times for 10 min each), (d) incubated with DAPI (for 5 min), (e) washed in PBS alone (2 times, for 10 min each) and, finally, (f) mounted in Mowiol solution (composition in Table 7.6). All antibodies and DAPI were applied using a dilution of 1:1000.

7.2.9 Confocal microscopy

Numerous microscopic analyses of the fluorescent signal of processed brain slices were performed with a confocal laser-scanning microscope (LSM710 and Axio Examiner.Z1, Zeiss) on Zen imaging software (Zeiss). Laser wavelength and spectral filter settings were selected according to the fluorophores present in the sample (Table 7.5). To reduce fluorophore bleaching, laser intensity was typically set close to the minimum value that would still be able to saturate the image (with detector gain set to maximum). Subsequently, the dynamic range of image acquisition was optimized by lowering the detector gain (if necessary) until close to the maximum value that would saturate the image; ensuing adjustments were made to the digital offset and gain. Images were acquired without immersion and objective magnification was chosen according to requirements: whole-slice single-channel (DAPI) reconstructions were obtained employing a epifluorescent configuration and a 5× objective (N-Achroplan, numerical aperture [NA] 0.13); multichannel acquisitions for examination of the extent of virus expression and tracer spread were performed in epifluorescent configuration, with a 10× objective (Fluar, NA 0.5); analysis of signal colocalization required collection of confocal z-stacks with a 20× objective (Plan-Apochromat, NA 0.8). The pinhole of the microscope was fully opened for epifluorescent acquisitions. In confocal acquisitions, the pinhole size was set to 1 Airy unit for the channel of longest wavelength; for the other channels, the pinhole size was set such that the optical slice thickness (i.e. the diameter of the Airy disk) in metric units would match the one of the longest-wavelength channel. Acquisition of confocal image stacks (z-stacks) was carried out in steps of 2 µm, from the bottom of the slice to the top. Images were acquired with varying resolution (in pixels): 512×512 in whole-slice reconstructions; 1024×1024 in retrograde-tracing experiments; 2048×2048 for analysis of virus-expression spread and colocalization. Digitization of images was usually performed with a colour depth of 16 bit.

7.2.10 Data analysis

Acquired data consisted of electrophysiological, video and cell-imaging data. These data were processed, analysed and statistically tested using custom-made algorithms running offline on Matlab. Electrophysiological data were converted with MC_DataTool (Multi Channel Systems) from their native format to text files (TXT) prior to importing them on Matlab. Cell-imaging data were preprocessed on ImageJ. Synthetized acoustic stimuli were analysed on Matlab. The original figures here reported were prepared and visualized on Matlab, ImageJ and Inkscape (software versions on Table 7.2).

Mice showed (post mortem) an acceptable spread of expression (diameter > 0.5 mm) in the ACx contralateral to the optrode; however, ipsilaterally that hold true only for 8 out of 10 eNpHR-expressing mice. Accordingly, only these mice were considered for analysis of LFPs recorded during the non-behavioural session, as this was the only session in which mice received optogenetic stimulation during LFP acquisition. Also, for this session, electrophysiological and cell-imaging data here presented from a single subject (i.e. non-pooled data) were all taken from the same mouse.

Throughout this section the term ‘sample’ will be used to refer to individual data points. The total number of samples of a given vector with data is here denoted by ‘N_S’. The sampling frequency is here represented by ‘F_S’. The image resolution of a given quantity (e.g. image temporal resolution) concerns the number of pixels of the image in the dimension along the axis of that quantity (e.g. the number of pixel columns [width] for a quantity plotted along the x-axis).

7.2.10.a Acoustic analysis

Spectrograms of acoustic stimuli were computed using the ‘spectrogram’ function of Matlab. The size (in number of samples) of the Hamming window (N_{SW}) used to compute the spectrogram was equivalent to a temporal resolution (R_T) of 1 ms (Eq. (7.2)).

$$N_{SW} = R_T \times F_S \tag{7.2}$$

The number of overlapping samples between 2 consecutive Hamming windows (N_{SO}) was equivalent to an image temporal resolution (R_{TI}) of approximately 100 pixels (Eq. (7.3)), i.e. a N_{SO} was determined such that 100 windows were employed. Power was computed for a vector of linearly spaced frequencies, from 1–96 kHz, of size identical to an image frequency resolution of 100 pixels.

$$N_{SO} = N_{SW} - (N_S - N_{SW})/R_{TI} \tag{7.3}$$

7.2.10.b Temporal analysis of local field potentials

Broadband and gamma-band signals were derived from LFP signals band-pass filtered from 10–200 and 30–80 Hz respectively. Band-pass filtering was executed with a 2nd-order elliptic infinite-impulse-response (IIR) non-causal filter using the Matlab function ‘filtfilt'. Representative voltage traces correspond to the 5th and 23rd repetitions of a given condition in non-behavioural and fear-test sessions respectively. Average traces consisted of the arithmetic mean of traces from all 20 repetitions of a condition, in the non-behavioural session, and from the first 90 repetitions of a CS in fear-test sessions. Normalized average broadband traces resulted from dividing the average broadband trace of every condition by the average trace of the acou + optog$^-$ condition. The criterion for detection of the N15 AEP in normalized average broadband traces was the minimum voltage from 10–20 ms. N15 amplitude and latency corresponded, respectively, to the absolute value of the minimum normalized voltage and to the duration of the period between this minimum and the sound onset. The shape of the cortical AEPs were compared to those reported in the literature; together with the histological evaluation (see Sect. 7.2.10.f), this comparison conferred additional evidence for the location of the recording sites at the initially targeted brain regions, namely in the ACx[124], precisely in layers IV and V[122,123].

7.2.10.c Spectral analysis of local field potentials

Spectral density estimation of LFP signals was preceded by preprocessing the LFP signals with a band-pass filter (2nd-order elliptic IIR non-causal filter) from 10–200 Hz using the Matlab function ‘filtfilt'. Spectrograms of the LFP signal were computed similarly to spectrograms of acoustic stimuli (see Sect. 7.2.10.a). Here, the size of the Hamming window was equivalent to a temporal resolution of 1 ms and the number of overlapping samples between windows was equivalent to an image temporal resolution of approximately 300 pixels. The spectrogram was computed for a vector of logarithmically spaced frequencies, from 10–200 kHz, of size identical to an image frequency resolution of 100 pixels. Average spectrograms resulted from the arithmetic mean of spectrograms (after converting power density to its base 10 logarithm) of all 20 repetitions of a condition, in the non-behavioural session, and from the first 90 repetitions of a CS in fear-test sessions. Spectrogram normalization was performed by dividing the average spectrogram by the average baseline power, i.e. the power $P(T,F)$ of a pixel at time T and frequency F, was divided by the mean power of the pixels, at that same frequency, lying within the baseline. The differential spectrogram resulted from subtracting the average spectrogram of the acou + optog$^-$ condition to the one of the acou + optog$^+$ condition. Normalized average power spectral density (PSD) was calculated with the ‘pmtm’ function of Matlab by dividing the average PSD of the post-stimulus-onset period (after sound onset or equivalent moment) by the average baseline PSD. Average PSDs resulted from the arithmetic mean of PSDs (after converting power density to its base 10 logarithm) across repetitions of a given condition. The post-stimulus-onset period in the non-behavioural and fear-test sessions ranged from 150–400 ms and from 150–450 ms, respectively. Baseline ranged from −450 to −200 ms, in the non-behavioural session, and −350 to −50 ms, in fear-test sessions. The time–half-bandwidth product (TW) was selected such that the resolution bandwidth ($2W$, i.e. a small multiple of the frequency resolution) would be equal to 20 Hz. The PSD was computed for a vector of logarithmically spaced frequencies, from 10–200 kHz, of size identical to an image frequency resolution of 100 pixels. Normalized average gamma-band power corresponded to the mean values, from 30–80 Hz, of the normalized average PSD.

7.2.10.d Analysis of synchronization of local field potentials

Synchronization of gamma rhythms between the ACx and MGB was evaluated, with two different measures, in the same preprocessed data used for spectral density estimation (see previous section). Cross-correlation of the instantaneous amplitudes of gamma-band LFP signals (filtering specifications in 7.2.10.b) from the ACx and MGB was performed according to the method devised by Adhikari, Sigurdsson, Topiwala and Gordon (2010). The instantaneous amplitude of gamma-band traces was computed by extracting the absolute value of the Hilbert transform of the trace using Matlab function ‘hilbert’. Normalized cross-correlograms of amplitudes were obtained with the function ‘xcorr’ for a maximum lag of 70 ms. The representative, average and group normalized cross-correlograms resulted from data drawn from the acou condition. The first of these cross-correlograms corresponded to the 5th repetition of that condition; the average and group cross-correlograms corresponded to the arithmetic mean of cross-correlograms (across repetitions) from one subject and from all eNpHR-expressing subjects respectively. Correlation coefficient difference was calculated by subtracting the baseline (−450 to −200 ms) correlation coefficient to the correlation coefficient relative to the post-stimulus period (150–400 ms after sound onset or equivalent moment). Correlation coefficients consisted of the arithmetic mean (across repetitions) of the maxima of normalized cross-correlograms.

Gamma-band coherence difference resulted from subtracting the baseline gamma-band coherence to the post-stimulus gamma-band coherence of the LFP signals from the ACx and MGB. Gamma-band coherence (C) consisted of the arithmetic mean of the values, from 30–80 Hz, of the coherence (spectrum). Coherence was calculated according to Drongelen (2007) from the squared absolute values of the arithmetic mean (across repetitions) of the cross-PSD ($xpsd$) and from the mean (across repetitions) of the PSDs (psd_{ACx} and psd_{MGB}) of the 2 signals (Eq. (7.4)). The cross-PSD and PSD were computed for a 32-element vector of linearly spaced frequencies, from 30–80 Hz, using Matlab functions ‘cpsd’ and ‘pwelch’ respectively. The size of the Hamming window was equivalent to a temporal resolution of 100 ms (Eq. (7.2)) and the number of overlapping samples between windows was half the window size.

$$C = \operatorname{mean}\left(\frac{\operatorname{abs}\left(\operatorname{mean}(xpsd)_{\text{reps.}}\right)^2}{\operatorname{mean}(psd_{ACx})_{\text{reps.}} \times \operatorname{mean}(psd_{MGB})_{\text{reps.}}}\right)_{30-80\ \text{Hz}} \quad (7.4)$$

7.2.10.e Behavioural analysis

Accurate, automated measurement of mouse movement and ensuing detection of video-recorded freezing responses was performed with custom-designed algorithm running on Matlab. Freezing analysis was carried out in 4 stages: (a) first, regions of interest (ROIs) covering the arena with the mouse and the IR LEDs (see Sect. 7.2.7.a) would be manually defined on the first frame of each video; (b) next, a frame-by-frame analysis would measure the mouse movement and the state of every IR LED; (c) subsequently, the state of the IR LEDs would be used to assign frames to the corresponding epoch (see Sect. 7.2.7.b); (d) lastly, freezing during each epoch would be computed. Delineation of ROIs was in part done with the Matlab function ‘roitool’[244]. Movement detection and quantification was based on a modification to the measure of significant motion pixel (SMP) described by Kopec et al. (2007): instead of the definition presented by these authors, here a SMP consists of a pixel whose absolute difference of 8-bit greyscale-value (i.e. luminance) between two consecutive frames is equal or greater than 30 (movement threshold). Each IR LED was interpreted as being on whenever its 8-bit greyscale-value was equal or greater than 250. Mice were considered to be freezing whenever the number of SMP would be less than 50 (freezing threshold) for at least 2 s (Fig. 5.6F). The movement and freezing thresholds were calibrated by visual inspection of one video and comparison with the outcome of the corresponding freezing analysis. Validation of freezing detection was performed by visual inspection of videos from 3 mice, which yielded an accuracy of detection of 100%. Plots with results pooled from several mice display concern to data exclusively from test sessions, so comparisons between optogenetic conditions relate to the optogenetic manipulations executed on the previous day. Results in summary plots with comparisons between test phases (baseline, CS^- and CS^+), optogenetic manipulations and conditioning and reconditioning were obtained from the arithmetic mean of the first 4 corresponding epochs.

7.2.10.f Image processing

Virus-transduction efficacy (70 ± 11%, *n* = 7, $CL_{95\%}$ = 10%) and specificity (69 ± 17%, *n* = 7, $CL_{95\%}$ = 16%, Fig. 5.1B) were estimated from counts of fluorescent somata and assessments of fluorophore colocalization in two-dimensional projections of coronal z-stacks taken in mice expressing eNpHR (see Sect. 7.2.9 for raw-image specifications). The analysed data were sampled in both hemispheres of 3 out of 4 animals (and solely in the left hemisphere of one animal). Virus transduction (i.e. eNpHR expression) was evaluated based on fluorescent signals from EYFP fused to eNpHR (2/4 mice) and from Alexa Fluor 647 indirectly conjugated to an anti-GFP antibody (2/4 mice). PV^+ cells were detected from the fluorescent signal of Cy3 indirectly conjugated to an anti-PV antibody. Cell counting was manually performed with the assistance of

ImageJ plugin ‘Cell Counter’. Transduction efficacy was calculated as the fraction of PV^+ cells colocalized with eNpHR-expressing cells; transduction specificity was measured as the fraction of eNpHR-expressing cells colocalized with PV^+ cells. End values were comparable to those previously reported in a similar study[66].

Whole-slice reconstructions (Figs. 5.1D and 5.5D) were obtained with ImageJ stitching plugins ‘MosaicJ’ and ‘Grid/Collection stitching’ (see Sect. 7.2.9 for raw-image specifications). The ACx and MGB were identified by overlaying reconstructions with schematic figures, taken from a mouse brain atlas[238], that would adequately fit them. Eventually, the reconstructions allowed to confirm that the electrophysiological recordings were performed from the initially targeted brain areas (in the dorsal ACx, explicitly from layers IV and V, 2.6–2.8 mm posterior of bregma; in the dorsal MGB, 3–3.2 mm posterior of bregma). Sites of retrograde tracer uptake and transport terminus were likewise confirmed to correspond to targeted brain regions (in the dorsal ACx, 2.6–2.8 mm posterior of bregma; in the dorsal MGB, 3.1–3.3 mm posterior of bregma).

7.2.10.g Statistical analysis

Statistical analysis was entirely performed on Matlab using its native functions. Descriptive statistics is reported, for normally distributed samples, in terms of the arithmetic mean directly followed by the standard deviation and sample size. Samples deviating from normality are reported through the corresponding median followed by the interquartile range (IQR) and sample size. Inferential statistics are reported either in the form of a confidence limit (CL, i.e. half the confidence interval range, for a confidence level of 95%, based on Student’s *t*-distribution) or by a hypothesis test statistic followed by the corresponding *p*-value. Hypothesis testing specifications, such as the specific statistical test and multiple comparisons adjustment employed as well as the direction of testing, are always mentioned in text. Validation measures to which these tests were submitted are listed on Table 7.8. All tests were submitted to a significance level (α) of 5%. The *p*-values of pairwise comparisons were adjusted for multiple comparisons with Šidák correction (the number of comparisons, m, is always stated in text), with the exception of post-hoc pairwise Tukey’s tests as this type of test does not require further correction). When the normality assumption of parametric tests was violated, an equivalent non-parametric test was used instead. Whenever the sphericity assumption of repeated measures ANOVA was not satisfied, repeated measures parametric testing was realized by paired Student’s *t*-tests corrected for multiple comparisons. The intrinsic non-normality of N15 amplitude ratios reported on Fig. 5.4B for the condition acou + optog^- precluded the use of repeated measures ANOVA and ensuing post-hoc pairwise Tukey’s tests.

Table 7.8 | Validation measures applied in statistical hypothesis testing. Validation tests were: Anderson-Darling test (AD), Mauchly's test (M) and two-sample *F*-test (F). Anderson-Darling test statistic, *AD*, and *p*-value is reported solely for the sample with the smallest *p*-value.

Fig.	Assumption tested and results	Test	Statistic	*p*-value
5.2F	No deviation from normality was identified in any of the differences among conditions nor within any condition	AD	$AD = 0.60$	$p = 0.214$ after Šidák corr., $m = 3$
	Sphericity assumption of repeated measures ANOVA was validated for sham-injected and eNpHR-expressing mice	M	$X^2_{(2)} = 4.46$ and $X^2_{(2)} = 0.91$	$p = 0.107$ and $p = 0.636$
5.3D	No deviation from normality was identified in any of the differences among conditions nor within any condition	AD	$AD = 0.59$	$p = 0.084$ after Šidák corr., $m = 3$
5.4B	No deviation from normality was detected in any of the differences among conditions	AD	$AD = 0.40$	$p = 0.48$ after Šidák corr., $m = 3$
5.5H and 5.5I	No deviation from normality was identified within any condition	AD	$AD = 0.43$ and $AD = 0.55$	$p = 0.68$ and $p = 0.37$ after Šidák corr., $m = 4$
	Sphericity assumption of repeated measures ANOVA was validated	M	$X^2_{(5)} = 1.09$ and $X^2_{(5)} = 9.89$	$p = 0.955$ and $p = 0.078$
5.7D	A test phase was not normally distributed, precluding the use of repeated measures ANOVA and ensuing pairwise Tukey's tests	AD	$AD = 1.11$	$p = 0.010$ after Šidák corr., $m = 3$
5.7E	No deviation from normality was detected in the difference between optog$^+$ and recond and within manipulations of each test phase	AD	$AD = 0.54$	$p = 0.085$ after Šidák corr., $m = 3$
	Equal variances validated independent-samples *t*-tests between optog$^+$ and optog$^-$ and between recond and optog$^-$	F	$F_{(4,4)} = 0.88$ and $F_{(4,4)} = 0.38$	$p = 0.990$ and $p = 0.603$ both after Šidák corr., $m = 2$
5.8C	No deviation from normality was detected in the difference between optog$^+$ and recond and within manipulations of the test phase CS$^+$	AD	$AD = 0.47$	$p = 0.374$ after Šidák corr., $m = 3$
	Equal variances validated independent-samples *t*-tests between optog$^+$ and optog$^-$ and between recond and optog$^-$	F	$F_{(4,4)} = 1.42$ and $F_{(4,4)} = 2.73$	$p = 0.934$ and $p = 0.583$ both after Šidák corr., $m = 2$
5.8E	No deviation from normality was detected in the difference between optog$^+$ and recond and within manipulations of each test phase	AD	$AD = 0.45$	$p = 0.160$ after Šidák corr., $m = 3$
	Equal variances validated independent-samples *t*-tests between optog$^+$ and optog$^-$ and between recond and optog$^-$	F	$F_{(4,4)} = 3.60$ and $F_{(4,4)} = 1.55$	$p = 0.426$ and $p = 0.897$ both after Šidák corr., $m = 2$

8 List of abbreviations

In alphabetical order:

acou	acoustic
ACSF	artificial cerebrospinal fluid
ACx	auditory cortex
AEP	auditory-evoked potential
ANOVA	analysis of variance
$CL_{95\%}$	confidence limit for a confidence level of 95%
cond	fear-conditioned
CS	conditioned stimulus
DAC	digital-to-analogue converter
DAPI	4',6-diamidino-2-phenylindole
DPSS	diode-pumped solid-state laser
eNpHR	enhanced halorhodopsin
E/I	excitation–inhibition
FRB	fast rhythmic bursting
GABA	γ-amino butyric acid
GFP	green fluorescent protein
GWN	Gaussian white noise
IIR	infinite-impulse-response
IHC	immunohistochemistry
ING	interneuron gamma
IQR	interquartile range
IR	infrared
LD	laser diode
LED	light-emitting diode
LFP	local field potential
MGB	medial geniculate body
N15	negative at a 15 ms latency
NA	numerical aperture

NMDA	N-methyl-D-aspartate
NGS	normal goat serum
optog	optogenetic
PBS	phosphate-buffered saline
PC	pyramidal cell
PFA	paraformaldehyde
PII	perisoma-inhibiting interneuron
PING	pyramidal-interneuron gamma
PSD	power spectral density
PV	parvalbumin
rAAV	recombinant adeno-associated virus
recond	fear-reconditioned
RMS	root mean square
ROI	region of interest
RT	room temperature
SMP	significant motion pixel
TTL	transistor–transistor logic
US	unconditioned stimulus

9 References

1. McBain, C. J. & Fisahn, A. Interneurons unbound. *Nat. Rev. Neurosci.* **2,** 11–23 (2001).
2. Markram, H. *et al.* Interneurons of the neocortical inhibitory system. *Nat. Rev. Neurosci.* **5,** 793–807 (2004).
3. Ascoli, G. a *et al.* Petilla terminology: nomenclature of features of GABAergic interneurons of the cerebral cortex. *Nat. Rev. Neurosci.* **9,** 557–68 (2008).
4. DeFelipe, J. *et al.* New insights into the classification and nomenclature of cortical GABAergic interneurons. *Nat. Rev. Neurosci.* **14,** 202–16 (2013).
5. Sahara, S., Yanagawa, Y., O'Leary, D. D. M. & Stevens, C. F. The fraction of cortical GABAergic neurons is constant from near the start of cortical neurogenesis to adulthood. *J. Neurosci.* **32,** 4755–61 (2012).
6. Isaacson, J. S. & Scanziani, M. How inhibition shapes cortical activity. *Neuron* **72,** 231–43 (2011).
7. Dichter, M. A. & Ayala, G. F. Cellular mechanisms of epilepsy: a status report. *Science* **237,** 157–64 (1987).
8. Sillito, A. M. The contribution of inhibitory mechanisms to the receptive field properties of neurones in the striate cortex of the cat. *J. Physiol.* **250,** 305–29 (1975).
9. Yizhar, O. *et al.* Neocortical excitation/inhibition balance in information processing and social dysfunction. *Nature* **477,** 171–178 (2011).
10. Pfeffer, C. K., Xue, M., He, M., Huang, Z. J. & Scanziani, M. Inhibition of inhibition in visual cortex: the logic of connections between molecularly distinct interneurons. *Nat. Neurosci.* **16,** 1068–76 (2013).
11. Letzkus, J. J. *et al.* A disinhibitory microcircuit for associative fear learning in the auditory cortex. *Nature* **480,** 331–5 (2011).
12. Pi, H.-J. *et al.* Cortical interneurons that specialize in disinhibitory control. *Nature* **503,** 521–4 (2013).
13. Lee, S., Kruglikov, I., Huang, Z. J., Fishell, G. & Rudy, B. A disinhibitory circuit mediates motor integration in the somatosensory cortex. *Nat. Neurosci.* **16,** 1662–70 (2013).
14. Letzkus, J. J., Wolff, S. B. E. & Lüthi, A. Disinhibition, a Circuit Mechanism for Associative Learning and Memory. *Neuron* **88,** 264–276 (2015).
15. Adesnik, H., Bruns, W., Taniguchi, H., Huang, Z. J. & Scanziani, M. A neural circuit for spatial summation in visual cortex. *Nature* **490,** 226–31 (2012).
16. Harris, K. D. & Mrsic-Flogel, T. D. Cortical connectivity and sensory coding. *Nature* **503,** 51–8 (2013).

17. Li, L.-Y. *et al.* Differential Receptive Field Properties of Parvalbumin and Somatostatin Inhibitory Neurons in Mouse Auditory Cortex. *Cereb. Cortex* **14,** 2–3 (2014).

18. Kvitsiani, D. *et al.* Distinct behavioural and network correlates of two interneuron types in prefrontal cortex. *Nature* **498,** 363–6 (2013).

19. Kepecs, A. & Fishell, G. Interneuron cell types are fit to function. *Nature* **505,** 318–26 (2014).

20. Fino, E., Packer, A. M. & Yuste, R. The logic of inhibitory connectivity in the neocortex. *Neuroscientist* **19,** 228–37 (2013).

21. Gulledge, A. T. & Stuart, G. J. Excitatory actions of GABA in the cortex. *Neuron* **37,** 299–309 (2003).

22. Martina, M., Royer, S. & Paré, D. Cell-type-specific GABA responses and chloride homeostasis in the cortex and amygdala. *J. Neurophysiol.* **86,** 2887–2895 (2001).

23. Vu, E. T. & Krasne, F. B. Evidence for a Computational Distinction Between Proximal and Distal Neuronal Inhibition. *Science (80-.).* **255,** 1710–1712 (1992).

24. Silver, R. A. Neuronal arithmetic. *Nat. Rev. Neurosci.* **11,** 474–489 (2010).

25. Carandini, M. & Heeger, D. Normalization as a canonical neural computation. *Nat. Rev. Neurosci.* 1–12 (2012). doi:10.1038/nrn3136

26. Rose, D. & Blakemore, C. Effects of bicuculline on functions of inhibition in visual cortex. *Nature* **249,** 375–377 (1974).

27. Lee, S.-H., Kwan, A. C. & Dan, Y. Interneuron subtypes and orientation tuning. *Nature* **508,** E1–2 (2014).

28. Wehr, M. & Zador, A. M. Balanced inhibition underlies tuning and sharpens spike timing in auditory cortex. *Nature* **426,** 442–6 (2003).

29. Tan, A. Y., Zhang, L. I., Merzenich, M. M. & Schreiner, C. E. Tone-evoked excitatory and inhibitory synaptic conductances of primary auditory cortex neurons. *J Neurophysiol* **92,** 630–643 (2004).

30. Zhang, L. I., Zhou, Y. & Tao, H. W. Perspectives on: information and coding in mammalian sensory physiology: inhibitory synaptic mechanisms underlying functional diversity in auditory cortex. *J. Gen. Physiol.* **138,** 311–20 (2011).

31. Hamilton, L. S. *et al.* Optogenetic activation of an inhibitory network enhances feedforward functional connectivity in auditory cortex. *Neuron* **80,** 1066–76 (2013).

32. Kraushaar, U. & Jonas, P. Efficacy and Stability of Quantal GABA Release at a Hippocampal Interneuron-Principal Neuron Synapse. *J. Neurosci.* **20,** 5594–5607 (2000).

33. Bartos, M. *et al.* Fast synaptic inhibition promotes synchronized gamma oscillations in hippocampal interneuron networks. *Proc. Natl. Acad. Sci. U. S. A.* **99,** 13222–13227

(2002).

34. Hu, H., Gan, J. & Jonas, P. Interneurons. Fast-spiking, parvalbumin$^+$ GABAergic interneurons: from cellular design to microcircuit function. *Science* **345,** 1255263 (2014).

35. Pouille, F. & Scanziani, M. Enforcement of temporal fidelity in pyramidal cells by somatic feed-forward inhibition. *Science* **293,** 1159–63 (2001).

36. Huang, Z. J., Di Cristo, G. & Ango, F. Development of GABA innervation in the cerebral and cerebellar cortices. *Nat. Rev. Neurosci.* **8,** 673–86 (2007).

37. Rudy, B., Fishell, G., Lee, S. & Hjerling-Leffler, J. Three groups of interneurons account for nearly 100% of neocortical GABAergic neurons. *Dev. Neurobiol.* **71,** 45–61 (2011).

38. Liu, X. & Tonegawa, S. Optogenetics 3.0. *Cell* **141,** 22–24 (2010).

39. Madisen, L. *et al.* A toolbox of Cre-dependent optogenetic transgenic mice for light-induced activation and silencing. *Nat. Neurosci.* **15,** 793–802 (2012).

40. Karnani, M. M. *et al.* Cooperative Subnetworks of Molecularly Similar Interneurons in Mouse Neocortex. *Neuron* **90,** 1–15 (2016).

41. Caillard, O. *et al.* Role of the calcium-binding protein parvalbumin in short-term synaptic plasticity. *Proc. Natl. Acad. Sci. U. S. A.* **97,** 13372–13377 (2000).

42. Vreugdenhil, M., Jefferys, J. G. R., Celio, M. R. & Schwaller, B. Parvalbumin-deficiency facilitates repetitive IPSCs and gamma oscillations in the hippocampus. *J. Neurophysiol.* **89,** 1414–1422 (2003).

43. Eggermann, E. & Jonas, P. How the 'slow' Ca2+ buffer parvalbumin affects transmitter release in nanodomain-coupling regimes. *Nat. Neurosci.* **15,** 20–22 (2011).

44. Reyes, A. *et al.* Target-cell-specific facilitation and depression in neocortical circuits. *Nat. Neurosci.* **1,** 279–285 (1998).

45. Beierlein, M., Gibson, J. R. & Connors, B. W. Two dynamically distinct inhibitory networks in layer 4 of the neocortex. *J. Neurophysiol.* **90,** 2987–3000 (2003).

46. Tan, Z., Hu, H., Huang, Z. J. & Agmon, A. Robust but delayed thalamocortical activation of dendritic-targeting inhibitory interneurons. *Proc. Natl. Acad. Sci. U. S. A.* **105,** 2187–92 (2008).

47. Cobb, S. R., Buhl, E. H., Halasy, K., Paulsen, O. & Somogyi, P. Synchronization of neuronal activity in hippocampus by individual GABAergic interneurons. *Nature* **378,** 75–8 (1995).

48. Tamás, G., Buhl, E. H., Lörincz, A. & Somogyi, P. Proximally targeted GABAergic synapses and gap junctions synchronize cortical interneurons. *Nat. Neurosci.* **3,** 366–371 (2000).

49. Bartos, M., Vida, I. & Jonas, P. Synaptic mechanisms of synchronized gamma oscillations

in inhibitory interneuron networks. *Nat. Rev. Neurosci.* **8,** 45–56 (2007).

50. Buzsáki, G. & Wang, X.-J. Mechanisms of gamma oscillations. *Annu. Rev. Neurosci.* **35,** 203–25 (2012).

51. Tiesinga, P. & Sejnowski, T. J. Cortical enlightenment: are attentional gamma oscillations driven by ING or PING? *Neuron* **63,** 727–32 (2009).

52. Geiger, J. R. P., Lübke, J., Roth, A., Frotscher, M. & Jonas, P. Submillisecond AMPA receptor-mediated signaling at a principal neuron- interneuron synapse. *Neuron* **18,** 1009–1023 (1997).

53. Kawaguchi, Y., Katsumaru, H., Kosaka, T., Heizmann, C. W. & Hama, K. Fast spiking cells in rat hippocampus (CA1 region) contain the calcium-binding protein parvalbumin. *Brain Res.* **416,** 369–74 (1987).

54. Moore, A. K. & Wehr, M. Parvalbumin-expressing inhibitory interneurons in auditory cortex are well-tuned for frequency. *J. Neurosci.* **33,** 13713–23 (2013).

55. McCormick, D. a, Connors, B. W., Lighthall, J. W. & Prince, D. a. Comparative electrophysiology of pyramidal and sparsely spiny stellate neurons of the neocortex. *J. Neurophysiol.* **54,** 782–806 (1985).

56. Pike, F. G. *et al.* Distinct frequency preferences of different types of rat hippocampal neurones in response to oscillatory input currents. *J. Physiol.* **529 Pt 1,** 205–13 (2000).

57. Hasenstaub, A. *et al.* Inhibitory postsynaptic potentials carry synchronized frequency information in active cortical networks. *Neuron* **47,** 423–35 (2005).

58. Li, X. G., Somogyi, P., Tepper, J. M. & Buzsáki, G. Axonal and dendritic arborization of an intracellularly labeled chandelier cell in the CA1 region of rat hippocampus. *Exp. brain Res.* **90,** 519–25 (1992).

59. Sik, A., Penttonen, M., Ylinen, A. & Buzsáki, G. Hippocampal CA1 interneurons: an in vivo intracellular labeling study. *J. Neurosci.* **15,** 6651–65 (1995).

60. Cardin, J. A. *et al.* Driving fast-spiking cells induces gamma rhythm and controls sensory responses. *Nature* **459,** 663–7 (2009).

61. Bragin, a *et al.* Gamma (40-100 Hz) oscillation in the hippocampus of the behaving rat. *J. Neurosci.* **15,** 47–60 (1995).

62. Csicsvari, J., Jamieson, B., Wise, K. D. & Buzsáki, G. Mechanisms of gamma oscillations in the hippocampus of the behaving rat. *Neuron* **37,** 311–322 (2003).

63. Mann, E. O., Suckling, J. M., Hajos, N., Greenfield, S. A. & Paulsen, O. Perisomatic feedback inhibition underlies cholinergically induced fast network oscillations in the rat hippocampus in vitro. *Neuron* **45,** 105–117 (2005).

64. Hájos, N. *et al.* Spike timing of distinct types of GABAergic interneuron during hippocampal

gamma oscillations in vitro. *J. Neurosci.* **24,** 9127–37 (2004).

65. Gloveli, T. *et al.* Differential involvement of oriens/pyramidale interneurones in hippocampal network oscillations in vitro. *J. Physiol.* **562,** 131–47 (2005).

66. Sohal, V. S., Zhang, F., Yizhar, O. & Deisseroth, K. Parvalbumin neurons and gamma rhythms enhance cortical circuit performance. *Nature* **459,** 698–702 (2009).

67. Carlén, M. *et al.* A critical role for NMDA receptors in parvalbumin interneurons for gamma rhythm induction and behavior. *Mol. Psychiatry* **17,** 537–48 (2012).

68. Siegle, J. H., Pritchett, D. L. & Moore, C. I. Gamma-range synchronization of fast-spiking interneurons can enhance detection of tactile stimuli. *Nat. Neurosci.* **17,** 1371–1379 (2014).

69. Tiesinga, P., Fellous, J. M. & Sejnowski, T. J. Regulation of spike timing in visual cortical circuits. *Nat. Rev. Neurosci.* **9,** 97–107 (2008).

70. Minlebaev, M., Colonnese, M., Tsintsadze, T., Sirota, A. & Khazipov, R. Early γ oscillations synchronize developing thalamus and cortex. *Science* **334,** 226–9 (2011).

71. Whittington, M. A., Traub, R. D., Kopell, N., Ermentrout, B. & Buhl, E. H. Inhibition-based rhythms: experimental and mathematical observations on network dynamics. *Int. J. Psychophysiol.* **38,** 315–36 (2000).

72. Galarreta, M. & Hestrin, S. A network of fast-spiking cells in the neocortex connected by electrical synapses. *Nature* **402,** 72–5 (1999).

73. Börgers, C. & Kopell, N. Synchronization in networks of excitatory and inhibitory neurons with sparse, random connectivity. *Neural Comput.* **15,** 509–538 (2003).

74. Traub, R. D., Jefferys, J. G. & Whittington, M. A. Simulation of gamma rhythms in networks of interneurons and pyramidal cells. *J. Comput. Neurosci.* **4,** 141–50 (1997).

75. Lisman, J. E. & Idiart, M. A. Storage of 7 +/- 2 short-term memories in oscillatory subcycles. *Science* **267,** 1512–5 (1995).

76. Lisman, J. E. Relating hippocampal circuitry to function: recall of memory sequences by reciprocal dentate-CA3 interactions. *Neuron* **22,** 233–242 (1999).

77. Hopfield, J. J. Pattern recognition computation using action potential timing for stimulus representation. *Nature* **376,** 33–6 (1995).

78. Buzsáki, G. & Chrobak, J. J. Temporal structure in spatially organized neuronal ensembles: a role for interneuronal networks. *Curr. Opin. Neurobiol.* **5,** 504–10 (1995).

79. Ray, S. & Maunsell, J. H. R. Do gamma oscillations play a role in cerebral cortex? *Trends Cogn. Sci.* **19,** 78–85 (2015).

80. Fries, P. A mechanism for cognitive dynamics: Neuronal communication through neuronal coherence. *Trends Cogn. Sci.* **9,** 474–480 (2005).

81. Fries, P., Nikolić, D. & Singer, W. The gamma cycle. *Trends Neurosci.* **30,** 309–16 (2007).

82. Lakatos, P. *et al.* An oscillatory hierarchy controlling neuronal excitability and stimulus processing in the auditory cortex. *J. Neurophysiol.* **94,** 1904–11 (2005).

83. Fontolan, L., Morillon, B., Liegeois-Chauvel, C. & Giraud, A.-L. The contribution of frequency-specific activity to hierarchical information processing in the human auditory cortex. *Nat. Commun.* **5,** 4694 (2014).

84. Jensen, O. & Colgin, L. L. Cross-frequency coupling between neuronal oscillations. *Trends Cogn. Sci.* **11,** 267–269 (2007).

85. Lisman, J. E. & Jensen, O. The θ-γ neural code. *Neuron* **77,** 1002–16 (2013).

86. Belluscio, M. a., Mizuseki, K., Schmidt, R., Kempter, R. & Buzsaki, G. Cross-Frequency Phase-Phase Coupling between Theta and Gamma Oscillations in the Hippocampus. *J. Neurosci.* **32,** 423–435 (2012).

87. Wulff, P. *et al.* Hippocampal theta rhythm and its coupling with gamma oscillations require fast inhibition onto parvalbumin-positive interneurons. *Proc. Natl. Acad. Sci. U. S. A.* **106,** 3561–3566 (2009).

88. Ma, W. *et al.* Visual representations by cortical somatostatin inhibitory neurons--selective but with weak and delayed responses. *J. Neurosci.* **30,** 14371–9 (2010).

89. Ribary, U. *et al.* Magnetic field tomography of coherent thalamocortical 40-Hz oscillations in humans. *Proc. Natl. Acad. Sci. U. S. A.* **88,** 11037–11041 (1991).

90. Spencer, K. M. *et al.* Abnormal neural synchrony in schizophrenia. *J. Neurosci.* **23,** 7407–7411 (2003).

91. Lewis, D. a, Hashimoto, T. & Volk, D. W. Cortical inhibitory neurons and schizophrenia. *Nat. Rev. Neurosci.* **6,** 312–24 (2005).

92. Wilson, T. W. *et al.* Cortical gamma generators suggest abnormal auditory circuitry in early-onset psychosis. *Cereb. Cortex* **18,** 371–8 (2008).

93. Spencer, K. M., Niznikiewicz, M. a, Nestor, P. G., Shenton, M. E. & McCarley, R. W. Left auditory cortex gamma synchronization and auditory hallucination symptoms in schizophrenia. *BMC Neurosci.* **10,** 85 (2009).

94. Spencer, K. M. Baseline gamma power during auditory steady-state stimulation in schizophrenia. *Front. Hum. Neurosci.* **5,** 190 (2011).

95. Billingslea, E. N. *et al.* Parvalbumin Cell Ablation of NMDA-R1 Causes Increased Resting Network Excitability with Associated Social and Self-Care Deficits. *Neuropsychopharmacology* **39,** 1603–13 (2014).

96. Hakami, T. *et al.* NMDA receptor hypofunction leads to generalized and persistent aberrant gamma oscillations independent of hyperlocomotion and the state of

consciousness. *PLoS One* **4,** e6755 (2009).

97. Molina, L. a, Skelin, I. & Gruber, A. J. Acute NMDA receptor antagonism disrupts synchronization of action potential firing in rat prefrontal cortex. *PLoS One* **9,** e85842 (2014).

98. Anderson, P. M., Jones, N. C., O'Brien, T. J. & Pinault, D. The N -Methyl d-Aspartate Glutamate Receptor Antagonist Ketamine Disrupts the Functional State of the Corticothalamic Pathway. *Cereb. Cortex* bhw168 (2016). doi:10.1093/cercor/bhw168

99. Koek, W., Woods, J. H. & Winger, G. D. MK-801, a proposed non-competitive antagonist of excitatory amino acid neurotransmission, produces phencyclidine-like behavioural effects in pigeons, rats and rhesus monkeys. *J. Pharmacol. Exp. Ther.* **245,** 969–974 (1988).

100. Malhotra, A. K. *et al.* Ketamine-induced exacerbation of psychotic symptoms and cognitive impairment in neuroleptic-free schizophrenics. *Neuropsychopharmacology* **17,** 141–150 (1997).

101. Andiné, P. *et al.* Characterization of MK-801-induced behavior as a putative rat model of psychosis. *J. Pharmacol. Exp. Ther.* **290,** 1393–1408 (1999).

102. Hetem, L. A. B., Danion, J. M., Diemunsch, P. & Brandt, C. Effect of a subanesthetic dose of ketamine on memory and conscious awareness healthy volunteers. *Psychopharmacology (Berl).* **152,** 283–288 (2000).

103. Coyle, J. T., Tsai, G. & Goff, D. Converging Evidence of NMDA Receptor Hypofunction in the Pathophysiology of Schizophrenia. *Ann. N. Y. Acad. Sci.* **1003,** 318–327 (2003).

104. Corlett, P. R., Honey, G. D. & Fletcher, P. C. From prediction error to psychosis: ketamine as a pharmacological model of delusions. *J. Psychopharmacol.* **21,** 238–252 (2007).

105. Homayoun, H. & Moghaddam, B. NMDA receptor hypofunction produces opposite effects on prefrontal cortex interneurons and pyramidal neurons. *J. Neurosci.* **27,** 11496–11500 (2007).

106. Zhang, Y., Behrens, M. M. & Lisman, J. E. Prolonged exposure to NMDAR antagonist suppresses inhibitory synaptic transmission in prefrontal cortex. *J. Neurophysiol.* **100,** 959–965 (2008).

107. Behrens, M. M. *et al.* Ketamine-induced loss of phenotype of fast-spiking interneurons is mediated by NADPH-oxidase. *Science* **318,** 1645–7 (2007).

108. Santarnecchi, E. *et al.* Frequency-dependent enhancement of fluid intelligence induced by transcranial oscillatory potentials. *Curr. Biol.* **23,** 1449–1453 (2013).

109. Sohal, V. S. Insights into cortical oscillations arising from optogenetic studies. *Biol. Psychiatry* **71,** 1039–45 (2012).

110. Beasley, C. L. & Reynolds, G. P. Parvalbumin-immunoreactive neurons are reduced in

the prefrontal cortex of schizophrenics. *Schizophr. Res.* **24,** 349–355 (1997).

111. Woo, T. U., Whitehead, R. E., Melchitzky, D. S. & Lewis, D. A. A subclass of prefrontal gamma-aminobutyric acid axon terminals are selectively altered in schizophrenia. *Proc. Natl. Acad. Sci. U. S. A.* **95,** 5341–6 (1998).

112. Hashimoto, T. *et al.* Gene expression deficits in a subclass of GABA neurons in the prefrontal cortex of subjects with schizophrenia. *J. Neurosci.* **23,** 6315–6326 (2003).

113. Gray, C. M. & Singer, W. Stimulus-specific neuronal oscillations in orientation columns of cat visual cortex. *Proc. Natl. Acad. Sci. U. S. A.* **86,** 1698–702 (1989).

114. Tiesinga, P. H., Fellous, J. M., Salinas, E., José, J. V. & Sejnowski, T. J. Inhibitory synchrony as a mechanism for attentional gain modulation. *J. Physiol. Paris* **98,** 296–314 (2004).

115. Börgers, C. & Kopell, N. J. Gamma oscillations and stimulus selection. *Neural Comput.* **20,** 383–414 (2008).

116. Moore, C. I., Carlen, M., Knoblich, U. & Cardin, J. A. Neocortical Interneurons: From Diversity, Strength. *Cell* **142,** 189–193 (2010).

117. Knoblich, U., Siegle, J. H., Pritchett, D. L. & Moore, C. I. What do we gain from gamma? Local dynamic gain modulation drives enhanced efficacy and efficiency of signal transmission. *Front. Hum. Neurosci.* **4,** 185 (2010).

118. Gradinaru, V., Thompson, K. R. & Deisseroth, K. eNpHR: a Natronomonas halorhodopsin enhanced for optogenetic applications. *Brain Cell Biol.* **36,** 129–39 (2008).

119. Gradinaru, V. *et al.* Targeting and readout strategies for fast optical neural control in vitro and in vivo. *J. Neurosci.* **27,** 14231–14238 (2007).

120. Raimondo, J. V, Kay, L., Ellender, T. J. & Akerman, C. J. Optogenetic silencing strategies differ in their effects on inhibitory synaptic transmission. *Nat. Neurosci.* **15,** 1102–1104 (2012).

121. Elgueta, C., Kohler, J. & Bartos, M. Persistent Discharges in Dentate Gyrus Perisoma-Inhibiting Interneurons Require Hyperpolarization-Activated Cyclic Nucleotide-Gated Channel Activation. *J. Neurosci.* **35,** 4131–4139 (2015).

122. Barth, D. S. & Di, S. Three-dimensional analysis of auditory-evoked potentials in rat neocortex. *J. Neurophysiol.* **64,** 1527–36 (1990).

123. Metherate, R. & Cruikshank, S. J. Thalamocortical inputs trigger a propagating envelope of gamma-band activity in auditory cortex in vitro. *Exp. brain Res.* **126,** 160–74 (1999).

124. Vianney-Rodrigues, P., Iancu, O. D. & Welsh, J. P. Gamma oscillations in the auditory cortex of awake rats. *Eur. J. Neurosci.* **33,** 119–29 (2011).

125. Bandyopadhyay, S., Shamma, S. a & Kanold, P. O. Dichotomy of functional organization

in the mouse auditory cortex. *Nat. Neurosci.* **13,** 361–8 (2010).

126. Hackett, T. a, Barkat, T. R., O'Brien, B. M. J., Hensch, T. K. & Polley, D. B. Linking topography to tonotopy in the mouse auditory thalamocortical circuit. *J. Neurosci.* **31,** 2983–95 (2011).

127. Guo, W. *et al.* Robustness of cortical topography across fields, laminae, anesthetic states, and neurophysiological signal types. *J. Neurosci.* **32,** 9159–72 (2012).

128. Carlsen, A. N. A broadband acoustic stimulus is more likely than a pure tone to elicit a startle reflex and prepared movements. *Physiol. Rep.* **3,** e12509 (2015).

129. Crone, N. E., Boatman, D., Gordon, B. & Hao, L. Induced electrocorticographic gamma activity during auditory perception. Brazier Award-winning article, 2001. *Clin. Neurophysiol.* **112,** 565–582 (2001).

130. Bar-Yosef, O. The effects of background noise on the neural responses to natural sounds in cat primary auditory cortex. *Front. Comput. Neurosci.* **1,** 1–11 (2007).

131. Zhang, F. *et al.* Optogenetic interrogation of neural circuits: technology for probing mammalian brain structures. *Nat. Protoc.* **5,** 439–56 (2010).

132. Gradinaru, V. *et al.* Molecular and cellular approaches for diversifying and extending optogenetics. *Cell* **141,** 154–65 (2010).

133. Mattis, J. *et al.* Principles for applying optogenetic tools derived from direct comparative analysis of microbial opsins. *Nat. Methods* **9,** 159–72 (2012).

134. Jacobs, G. H., Fenwick, J. C., Calderone, J. B. & Deeb, S. S. Human cone pigment expressed in transgenic mice yields altered vision. *J. Neurosci.* **19,** 3258–3265 (1999).

135. Jacobs, G. H., Williams, G. a, Cahill, H. & Nathans, J. Emergence of Novel Color. *Science (80-.).* **315,** 1723–25 (2007).

136. Walmsley, L. *et al.* Colour As a Signal for Entraining the Mammalian Circadian Clock. *PLoS Biol.* **13,** e1002127 (2015).

137. Tan, Z., Sun, W., Chen, T.-W., Kim, D. & Ji, N. Neuronal Representation of Ultraviolet Visual Stimuli in Mouse Primary Visual Cortex. *Sci. Rep.* **5,** 12597 (2015).

138. Yizhar, O., Fenno, L. E., Davidson, T. J., Mogri, M. & Deisseroth, K. Optogenetics in neural systems. *Neuron* **71,** 9–34 (2011).

139. Brosch, M., Budinger, E. & Scheich, H. Stimulus-related gamma oscillations in primate auditory cortex. *J. Neurophysiol.* **87,** 2715–25 (2002).

140. Bullock, T. H. & Achimowicz, J. Z. in *Oscillatory Event-Related Brain Dynamics* (eds. Pantev, C., Elbert, T. & Lütkenhöner, B.) 11–26 (Springer US, 1994). doi:10.1007/978-1-4899-1307-4_3

141. Pantev, C. Evoked and induced gamma-band activity of the human cortex. *Brain Topogr.*

7, 321–330 (1995).

142. Steinschneider, M., Fishman, Y. I. & Arezzo, J. C. Spectrotemporal analysis of evoked and induced electroencephalographic responses in primary auditory cortex (A1) of the awake monkey. *Cereb. Cortex* **18,** 610–625 (2008).

143. Mathalon, D. H. & Sohal, V. S. Neural Oscillations and Synchrony in Brain Dysfunction and Neuropsychiatric Disorders: It's About Time. *JAMA psychiatry* **72,** 840–4 (2015).

144. Franowicz, M. N. & Barth, D. S. Comparison of evoked potentials and high-frequency (gamma-band) oscillating potentials in rat auditory cortex. *J Neurophysiol* **74,** 96–112 (1995).

145. Jia, J. *et al.* Mechanisms of drug combinations: interaction and network perspectives. *Nat. Rev. Drug Discov.* **8,** 111–28 (2009).

146. Kayser, C., Petkov, C. I. & Logothetis, N. K. Tuning to sound frequency in auditory field potentials. *J. Neurophysiol.* **98,** 1806–9 (2007).

147. Kajikawa, Y. & Schroeder, C. E. How local is the local field potential? *Neuron* **72,** 847–58 (2011).

148. Luczak, A., Bartho, P. & Harris, K. D. Gating of sensory input by spontaneous cortical activity. *J. Neurosci.* **33,** 1684–95 (2013).

149. Adesnik, H. & Scanziani, M. Lateral competition for cortical space by layer-specific horizontal circuits. *Nature* **464,** 1155–60 (2010).

150. Talwar, S. K., Musial, P. G. & Gerstein, G. L. Role of mammalian auditory cortex in the perception of elementary sound properties. *J. Neurophysiol.* **85,** 2350–8 (2001).

151. Yaron, A., Hershenhoren, I. & Nelken, I. Sensitivity to complex statistical regularities in rat auditory cortex. *Neuron* **76,** 603–15 (2012).

152. Shaw, N. A. The auditory evoked potential in the rat-a review. *Prog. Neurobiol.* **31,** 19–45 (1988).

153. Di, S. & Barth, D. S. The functional anatomy of middle-latency auditory evoked potentials: thalamocortical connections. *J. Neurophysiol.* **68,** 425–31 (1992).

154. Kraus, N. & Nicol, T. in *Electroencephalography and Clinical Neurophysiology* (2009).

155. Barth, D. S. & Di, S. The functional anatomy of middle latency auditory evoked potentials. *Brain Res.* **565,** 109–15 (1991).

156. Liégeois-Chauvel, C., Musolino, A., Badier, J. M., Marquis, P. & Chauvel, P. Evoked potentials recorded from the auditory cortex in man: evaluation and topography of the middle latency components. *Electroencephalogr. Clin. Neurophysiol. Potentials Sect.* **92,** 204–214 (1994).

157. Howard, M. A. *et al.* Auditory Cortex on the Human Posterior Superior Temporal Gyrus.

92, 79–92 (2000).

158. Yvert, B., Crouzeix, A. & Bertrand, O. Multiple Supratemporal Sources of Magnetic and Electric Auditory Evoked Middle Latency Components in Humans. 411–423 (2001).

159. Sukov, W. & Barth, D. S. Cellular mechanisms of thalamically evoked gamma oscillations in auditory cortex. *J. Neurophysiol.* **85,** 1235–45 (2001).

160. Barth, D. S. & MacDonald, K. D. Thalamic modulation of high-frequency oscillating potentials in auditory cortex. *Nature* **383,** 78–81 (1996).

161. Jones, E. G. The thalamic matrix and thalamocortical synchrony. *Trends Neurosci.* **24,** 595–601 (2001).

162. Jones, E. G. Synchrony in the interconnected circuitry of the thalamus and cerebral cortex. *Ann. N. Y. Acad. Sci.* **1157,** 10–23 (2009).

163. Tovote, P., Fadok, J. P. & Lüthi, A. Neuronal circuits for fear and anxiety. *Nat. Rev. Neurosci.* **16,** 317–331 (2015).

164. LeDoux, J. E. Emotion Circuits in the Brain. *Annu. Rev. Neurosci.* **23,** 155–184 (2000).

165. Bang, S. J., Allen, T. A., Jones, L. K., Boguszewski, P. & Brown, T. H. Asymmetrical stimulus generalization following differential fear conditioning. *Neurobiol. Learn. Mem.* **90,** 200–216 (2008).

166. Antunes, R. & Moita, M. a. Discriminative auditory fear learning requires both tuned and nontuned auditory pathways to the amygdala. *J. Neurosci.* **30,** 9782–9787 (2010).

167. Romanski, L. M. & LeDoux, J. E. Bilateral destruction of neocortical and perirhinal projection targets of the acoustic thalamus does not disrupt auditory fear conditioning. *Neurosci. Lett.* **142,** 228–232 (1992).

168. Romanski, L. M. & LeDoux, J. E. Equipotentiality of thalamo-amygdala and thalamo-cortico-amygdala circuits in auditory fear conditioning. *J. Neurosci.* **12,** 4501–4509 (1992).

169. Rogan, M. T. & LeDoux, J. E. LTP is accompanied by commensurate enhancement of auditory-evoked responses in a fear conditioning circuit. *Neuron* **15,** 127–136 (1995).

170. Ohl, F. W., Wetzel, W., Wagner, T., Rech, A. & Scheich, H. Bilateral Ablation of Auditory Cortex in Mongolian Gerbil Affects Discrimination of Frequency Modulated Tones but not of Pure Tones. *Learn. Mem.* **6,** 347–362 (1999).

171. Yaniv, D., Desmedt, A., Jaffard, R. & Richter-Levin, G. The amygdala and appraisal processes: Stimulus and response complexity as an organizing factor. *Brain Res. Rev.* **44,** 179–186 (2004).

172. Peter, M. *et al.* Induction of immediate early genes in the mouse auditory cortex after auditory cued fear conditioning to complex sounds. *Genes, Brain Behav.* **11,** 314–324 (2012).

173. Weible, A. P. *et al.* Perceptual gap detection is mediated by gap termination responses in auditory cortex. *Curr. Biol.* **24,** 1447–1455 (2014).

174. Weible, A. P., Liu, C., Niell, C. M. & Wehr, M. Auditory Cortex Is Required for Fear Potentiation of Gap Detection. **34,** 15437–15445 (2014).

175. Aizenberg, M., Mwilambwe-Tshilobo, L., Briguglio, J. J., Natan, R. G. & Geffen, M. N. Bidirectional Regulation of Innate and Learned Behaviors That Rely on Frequency Discrimination by Cortical Inhibitory Neurons. *PLoS Biol.* **13,** 1–32 (2015).

176. Headley, D. B. & Weinberger, N. M. Gamma-band activation predicts both associative memory and cortical plasticity. *J. Neurosci.* **31,** 12748–58 (2011).

177. Headley, D. B. & Weinberger, N. M. Fear conditioning enhances γ oscillations and their entrainment of neurons representing the conditioned stimulus. *J. Neurosci.* **33,** 5705–17 (2013).

178. Li, L., Li, Y., Zhou, M., Tao, H. W. & Zhang, L. I. Intracortical multiplication of thalamocortical signals in mouse auditory cortex. *Nat. Neurosci.* **16,** 1179–81 (2013).

179. Li, Y., Ibrahim, L. a, Liu, B., Zhang, L. I. & Tao, H. W. Linear transformation of thalamocortical input by intracortical excitation. *Nat. Neurosci.* **16,** 1324–30 (2013).

180. Lien, A. D. & Scanziani, M. Tuned thalamic excitation is amplified by visual cortical circuits. *Nat. Neurosci.* **16,** 1315–23 (2013).

181. Rauschecker, J. P., Tian, B. & Hauser, M. Processing of complex sounds in the macaque nonprimary auditory cortex. *Science* **268,** 111–4 (1995).

182. Haider, B., Duque, A., Hasenstaub, A. R. & McCormick, D. A. Neocortical Network Activity In Vivo Is Generated through a Dynamic Balance of Excitation and Inhibition. **26,** 4535–4545 (2006).

183. Atallah, B. V. & Scanziani, M. Instantaneous Modulation of Gamma Oscillation Frequency by Balancing Excitation with Inhibition. *Neuron* **62,** 566–577 (2009).

184. Atallah, B. V., Bruns, W., Carandini, M. & Scanziani, M. Parvalbumin-Expressing Interneurons Linearly Transform Cortical Responses to Visual Stimuli. *Neuron* **73,** 159–170 (2012).

185. Lee, S.-H. *et al.* Activation of specific interneurons improves V1 feature selectivity and visual perception. *Nature* **488,** 379–83 (2012).

186. Wilson, N. R., Runyan, C. a, Wang, F. L. & Sur, M. Division and subtraction by distinct cortical inhibitory networks in vivo. *Nature* **488,** 343–8 (2012).

187. Ainsworth, M. *et al.* GABA B receptor-mediated, layer-specific synaptic plasticity reorganizes gamma-frequency neocortical response to stimulation. *Proc. Natl. Acad. Sci.* 201605243 (2016). doi:10.1073/pnas.1605243113

188. Waldert, S., Lemon, R. N. & Kraskov, A. Influence of spiking activity on cortical local field potentials. *J Physiol* **591,** 5291–303 (2013).

189. Cape, E. G., Manns, I. D., Alonso, A., Beaudet, A. & Jones, B. E. Neurotensin-induced bursting of cholinergic basal forebrain neurons promotes gamma and theta cortical activity together with waking and paradoxical sleep. *J. Neurosci.* **20,** 8452–8461 (2000).

190. Rodriguez, R., Kallenbach, U., Singer, W. & Munk, M. H. J. Short- and long-term effects of cholinergic modulation on gamma oscillations and response synchronization in the visual cortex. *J. Neurosci.* **24,** 10369–78 (2004).

191. Llinás, R., Ribary, U., Contreras, D. & Pedroarena, C. The neuronal basis for consciousness. *Philos. Trans. R. Soc. Lond. B. Biol. Sci.* **353,** 1841–9 (1998).

192. Destexhe, a, Contreras, D. & Steriade, M. Cortically-induced coherence of a thalamic-generated oscillation. *Neuroscience* **92,** 427–43 (1999).

193. Andolina, I. M., Jones, H. E., Wang, W. & Sillito, A. M. Corticothalamic feedback enhances stimulus response precision in the visual system. **2006,** 1–6 (2006).

194. Groh, A. *et al.* Convergence of Cortical and Sensory Driver Inputs on Single Thalamocortical Cells. *Cereb. Cortex* 3167–3179 (2013). doi:10.1093/cercor/bht173

195. Cardin, J. a *et al.* Targeted optogenetic stimulation and recording of neurons in vivo using cell-type-specific expression of Channelrhodopsin-2. *Nat. Protoc.* **5,** 247–54 (2010).

196. Buzsáki, G., Anastassiou, C. a & Koch, C. The origin of extracellular fields and currents--EEG, ECoG, LFP and spikes. *Nat. Rev. Neurosci.* **13,** 407–20 (2012).

197. Einevoll, G. T., Kayser, C., Logothetis, N. K. & Panzeri, S. Modelling and analysis of local field potentials for studying the function of cortical circuits. *Nat. Rev. Neurosci.* **14,** 770–85 (2013).

198. Gray, C. M. & McCormick, D. A. Chattering cells: superficial pyramidal neurons contributing to the generation of synchronous oscillations in the visual cortex. *Science* **274,** 109–13 (1996).

199. Steriade, M., Timofeev, I., Dürmüller, N. & Grenier, F. Dynamic properties of corticothalamic neurons and local cortical interneurons generating fast rhythmic (30-40 Hz) spike bursts. *J. Neurophysiol.* **79,** 483–490 (1998).

200. Brumberg, J. C., Nowak, L. G. & McCormick, D. a. Ionic mechanisms underlying repetitive high-frequency burst firing in supragranular cortical neurons. *J. Neurosci.* **20,** 4829–4843 (2000).

201. Cunningham, M. O. *et al.* A role for fast rhythmic bursting neurons in cortical gamma oscillations in vitro. *Proc. Natl. Acad. Sci. U. S. A.* **101,** 7152–7 (2004).

202. Cardin, J. A., Palmer, L. A. & Contreras, D. Stimulus-dependent gamma (30-50 Hz) oscillations in simple and complex fast rhythmic bursting cells in primary visual cortex. *J.*

Neurosci. **25,** 5339–50 (2005).

203. Urban-Ciecko, J. & Barth, A. L. Somatostatin-expressing neurons in cortical networks. *Nat. Rev. Neurosci.* **17,** 401–409 (2016).

204. de la Rocha, J., Marchetti, C., Schiff, M. & Reyes, A. D. Linking the response properties of cells in auditory cortex with network architecture: cotuning versus lateral inhibition. *J. Neurosci.* **28,** 9151–63 (2008).

205. Levy, R. B. & Reyes, A. D. Coexistence of lateral and co-tuned inhibitory configurations in cortical networks. *PLoS Comput. Biol.* **7,** e1002161 (2011).

206. Kapfer, C., Glickfeld, L. L., Atallah, B. V & Scanziani, M. Supralinear increase of recurrent inhibition during sparse activity in the somatosensory cortex. *Nat. Neurosci.* **10,** 743–53 (2007).

207. Silberberg, G. & Markram, H. Disynaptic Inhibition between Neocortical Pyramidal Cells Mediated by Martinotti Cells. *Neuron* **53,** 735–746 (2007).

208. Tsodyks, M. V & Markram, H. The neural code between neocortical pyramidal neurons depends on neurotransmitter release probability. *Proc. Natl. Acad. Sci. U. S. A.* **94,** 719–23 (1997).

209. Campeau, S. & Davis, M. Involvement of subcortical and cortical afferents to the lateral nucleus of the amygdala in fear conditioning measured with fear-potentiated startle in rats trained concurrently with auditory and visual conditioned stimuli. *J. Neurosci.* **15,** 2312–2327 (1995).

210. Boatman, J. A. & Kim, J. J. A thalamo-cortico-amygdala pathway mediates auditory fear conditioning in the intact brain. *Eur. J. Neurosci.* **24,** 894–900 (2006).

211. Ito, W., Pan, B.-X., Yang, C., Thakur, S. & Morozov, A. Enhanced generalization of auditory conditioned fear in juvenile mice. *Learn. Mem.* **16,** 187–192 (2009).

212. Ghosh, S. & Chattarji, S. Neuronal encoding of the switch from specific to generalized fear. *Nat. Neurosci.* **18,** 112–120 (2014).

213. Pietersen, C. Y., Bosker, F. J., Postema, F. & den Boer, J. a. Fear conditioning and shock intensity: the choice between minimizing the stress induced and reducing the number of animals used. *Lab. Anim.* **40,** 180–185 (2006).

214. Tsunada, J., Lee, J. H. & Cohen, Y. E. Differential representation of auditory categories between cell classes in primate auditory cortex. *J. Physiol.* **590,** 3129–39 (2012).

215. Tsunada, J., Liu, A. S. K., Gold, J. I. & Cohen, Y. E. Causal contribution of primate auditory cortex to auditory perceptual decision-making. *Nat. Neurosci.* **19,** 135–42 (2016).

216. Ohl, F. W., Scheich, H. & Freeman, W. J. Change in pattern of ongoing cortical activity with auditory category learning. *Nature* **412,** 733–6 (2001).

217. Nelken, I., Fishbach, A., Las, L., Ulanovsky, N. & Farkas, D. Primary auditory cortex of cats: Feature detection or something else? *Biol. Cybern.* **89,** 397–406 (2003).

218. Russ, B. E., Lee, Y. S. & Cohen, Y. E. Neural and behavioral correlates of auditory categorization. *Hear. Res.* **229,** 204–212 (2007).

219. Bathellier, B., Ushakova, L. & Rumpel, S. Discrete neocortical dynamics predict behavioral categorization of sounds. *Neuron* **76,** 435–49 (2012).

220. Harris, K. D. & Thiele, A. Cortical state and attention. *Nat. Rev. Neurosci.* **12,** 509–23 (2011).

221. Bizley, J. K. & Cohen, Y. E. The what, where and how of auditory-object perception. *Nat. Rev. Neurosci.* **14,** 693–707 (2013).

222. David H. Hubel, Calvin O. Henson, Rupert, A. & Galambos, R. Attention units in the auditory cortex. *Science* **129,** 1279–80 (1959).

223. Alain, C. Breaking the wave: Effects of attention and learning on concurrent sound perception. *Hear. Res.* **229,** 225–236 (2007).

224. Tiitinen, H. *et al.* Selective attention enhances the auditory 40-Hz transient response in humans. *Nature* **364,** 59–60 (1993).

225. Bickel, S., Lipp, H. P. & Umbricht, D. Impaired attentional modulation of auditory evoked potentials in N-methyl-D-aspartate NR1 hypomorphic mice. *Genes. Brain. Behav.* **6,** 558–68 (2007).

226. Buia, C. & Tiesinga, P. Attentional modulation of firing rate and synchrony in a model cortical network. *J. Comput. Neurosci.* **20,** 247–264 (2006).

227. Gregoriou, G. G., Gotts, S. J., Zhou, H. & Desimone, R. High-Frequency, Long-Range Coupling Between Prefrontal and Visual Cortex During Attention. *Science (80-.).* **324,** 1207–1210 (2009).

228. Buffalo, E. A., Fries, P., Landman, R., Buschman, T. J. & Desimone, R. Laminar differences in gamma and alpha coherence in the ventral stream. *Proc. Natl. Acad. Sci. U. S. A.* **108,** 11262–7 (2011).

229. Baldauf, D. & Desimone, R. Neural mechanisms of object-based attention. *Science* **344,** 424–7 (2014).

230. Alho, K. Selective Attention in Auditory Processing as Reflected by Event-Related Brain Potentials. *Psychophysiology* **29,** 247–263 (1992).

231. Moore, T. & Armstrong, K. M. Selective gating of visual signals by microstimulation of frontal cortex. *Nature* **421,** 370–3 (2003).

232. Molnár, M., Karmos, G., Csépe, V. & Winkler, I. Intracortical auditory evoked potentials during classical aversive conditioning in cats. *Biol. Psychol.* **26,** 339–50 (1988).

233. Tang, J. *et al.* Potentiated amygdaloid auditory-evoked potentials and freezing behavior after fear conditioning in mice. *Brain Res.* **919,** 232–41 (2001).

234. Murray, A. J. *et al.* Parvalbumin-positive CA1 interneurons are required for spatial working but not for reference memory. *Nat. Neurosci.* **14,** 297–9 (2011).

235. Morgan, M. a & Pfaff, D. W. Effects of estrogen on activity and fear-related behaviors in mice. *Horm. Behav.* **40,** 472–482 (2001).

236. Kwak, C., Lee, S. H. & Kaang, B. K. Social isolation selectively increases anxiety in mice without affecting depression-like behavior. *Korean J. Physiol. Pharmacol.* **13,** 357–360 (2009).

237. Koike, H. *et al.* Behavioral abnormality and pharmacologic response in social isolation-reared mice. *Behav. Brain Res.* **202,** 114–121 (2009).

238. Franklin, K. B. J. & Paxinos, G. *The Mouse Brain in Stereotaxic Coordinates*. (Academic Press, 2007).

239. Mastakov, M. Y., Baer, K., Xu, R., Fitzsimons, H. & During, M. J. Combined injection of rAAV with mannitol enhances gene expression in the rat brain. *Mol. Ther.* **3,** 225–232 (2001).

240. in *Springer Handbook of Acoustics* (ed. Rossing, T. D.) pp 387–425 (Springer New York, 2007). doi:10.1007/978-0-387-30425-0

241. Liao, Y.-F., Tsai, M.-L., Yen, C.-T. & Cheng, C.-H. A simple method for fabricating microwire tetrode with sufficient rigidity and integrity without a heat-fusing process. *J. Neurosci. Methods* **195,** 211–5 (2011).

242. Adhikari, A., Sigurdsson, T., Topiwala, M. a & Gordon, J. a. Cross-correlation of instantaneous amplitudes of field potential oscillations: a straightforward method to estimate the directionality and lag between brain areas. *J. Neurosci. Methods* **191,** 191–200 (2010).

243. Drongelen, W. van. *Signal Processing for Neuroscientists*. (Academic Press, 2007).

244. Balkay, L. roitool. *File Exchange - MATLAB Central* (2008). at <http://de.mathworks.com/matlabcentral/fileexchange/9183-roitool>

245. Kopec, C. D. *et al.* A robust automated method to analyze rodent motion during fear conditioning. *Neuropharmacology* **52,** 228–233 (2007).

10 Acknowledgments

Every new answer raises many more questions. How liberating is that? It implies that even when the answers are not the expected ones we have gained new questions to elaborate on. And the past four years have surely brought me my share of answers.

I would like to thank Prof. Marlene Bartos for giving me the opportunity to carry my PhD work in her lab.

I further thank Prof. Ad Aertsen for his availability to meet me and talk about my project, Prof. Didier Pinault for his interest in my project and for having me in his lab on different occasions, Damaris Cornec for the excellent and fun training in the preparation of rodents for head restraints, Prof. Andreas Lüthi for his availability on a number of occasions to discuss work-related issues and for providing for my training in fear conditioning at his lab, Dr. Philip Tovote for the very useful training in fear conditioning, Dr. Philippe Isope for the feedback on my work and Dr. Johannes Letzkus for the advice on fear conditioning and for the important feedback on the analysis of behavioural data.

Special thanks go to Dr. José (Pepe) Alcami whose critical comments on my work and thesis were of paramount importance and who kindly helped me with a number of pressing issues, to Dr. Claudio Elgueta who introduced me to patch clamping and consistently showed interest in my project, to Dr. Jonas Sauer who introduced me to several techniques and software and who shared with me his own Arduino and AutoIt scripts and to Thomas Hainmüller who clarified various issues whenever I needed a quick answer.

I am also grateful to Christian Paun for the prompt and exceedingly helpful IT support, to Hans-Joachim Weber and his workshop team for the insightful suggestions and valuable assistance with several technical issues, to Barbara Hillers, Dagmar Sonntag and Carmen Herr for the wonderful administrative support, to Kerstin Semmler and Karin Winterhalter for the excellent technical assistance, to Dr. Janina Kirsch and Dr. Birgit Ahrens for assisting me with my graduate studies and for giving me constructive advice on my presentations and to Dieter Möbius for the assistance with animal husbandry.

I would like to extend my gratitude to Dr. Shakuntala Savanthrapadian and Mei Yuan for the nice and frequent chats about many matters usually dealt with by doctoral candidates and to Dr. Michael Strüber, Dorthe Kaufhold, Johannes Köhler, Thomas Maulhardt, Christoph Benkowitz and Jonatan Biskamp for the many bits of serendipity.

Finally, I would like to express my deepest gratitude to my loyal friends who have never ceased to motivate me to enjoy the ‘ups’ and overcome the ‘downs’, to my caring family whose resolute support shaped my willpower and, above all, to my loving wife whose constant care extended my will beyond my own limits and who teaches me every day a new, precious way to see things. *Obrigado*, *Meu Bem*.

11 Curriculum vitae

Tiago Manuel Rocha Félix

tiago.felix@bcf.uni-freiburg.de

Tel.: +49 (0)761 203 67309

Personal details

Nationality: Portuguese

Date of birth: 3rd August 1985

Scientific and general education

2012–2016	PhD project ‘Perisomatic Inhibition in Gamma Oscillations and Auditory Learning’; Institute of Physiology and Bernstein Center Freiburg, University of Freiburg; Friedrich Miescher Institute, University of Basel; Inserm U1114, University of Strasbourg
2011	Research internship on brain–computer interfaces at the Human Media Interaction research group, University of Twente, the Netherlands
2009–2011	MSc in Biological Engineering, Instituto Superior Técnico, Portugal
2004–2010	BSc in Biological Engineering, Instituto Superior Técnico, Portugal

Fellowships

2013	Burroughs Wellcome Fund, Biophysics and Computation in Neurons and Networks extended conference, Neuroscience Institute at Princeton University, USA
2012-2015	PhD scholarship NeuroTime Erasmus Mundus Joint Doctorate programme
2011	MSc scholarship Erasmus Programme

List of oral communications at scientific meetings

2016	PhD- and Postdoc-Seminar, Bernstein Center Freiburg, Germany
2016	NeuroTime Annual Meeting 2016, Strasbourg, France
2015	NeuroTime Annual Meeting, Basel, Switzerland
2014	NeuroTime 3rd Annual Meeting, Amsterdam, the Netherlands
2013	PhD- and Postdoc-Seminar, Bernstein Center Freiburg, Germany
2013	Joint EuroSPIN / NeuroTime Meeting 2013, Schloss Beuggen, Germany

12 Appendix — Original report

Automatic recognition of interneuron type in the mouse auditory cortex via classification of electrophysiological signals

Tiago M. R. Félix *

Bernstein Center Freiburg, Laboratory of Information Processing in Neural Networks, Faculty of Biology, Freiburg im Breisgau, Germany

February 2013

Abstract

Interneurons constitute an exceptionally diverse cell population in the neocortex and present complex features. This work bears evidence of the existence of bidirectional relationships between different categories of features of interneurons. In particular, it is here demonstrated that the parameters derived from the leaky integrate-and-fire model may be used with appreciable reliability to build devices that could allow the automatic identification of the morphology and molecular profile of interneurons based merely on electrophysiological signals. This could provide a faster way to identify interneuron types and, in turn, may prove helpful in making neurophysiological experiments more flexible and less dependent upon molecular markers.

Keywords: interneuron; somatostatin; parvalbumin; leaky integrate-and-fire model; hierarchical clustering; classification; mouse auditory cortex.

---

1. Introduction

Neocortical interneurons are remarkably diverse with regard to their physiological, morphological, molecular and synaptic attributes (Fig. 1). Within this large and heterogeneous population of neurons, two groups of cells are recurrently considered in neurophysiological studies for both their high occurrence in the neocortex and functional significance: those cells expressing the neuropeptide somatostatin (SOM$^+$ interneurons) and those expressing the calcium-binding protein parvalbumin (PV$^+$ interneurons).

The relevance of somatostatin lies in the fact that it constitutes a reliable marker for the major type of dendrite-inhibiting interneuron, the Martinotti cell; similarly, parvalbumin finds its relevance in its reliability as a marker for perisoma-inhibiting interneurons (Markram et al., 2004).

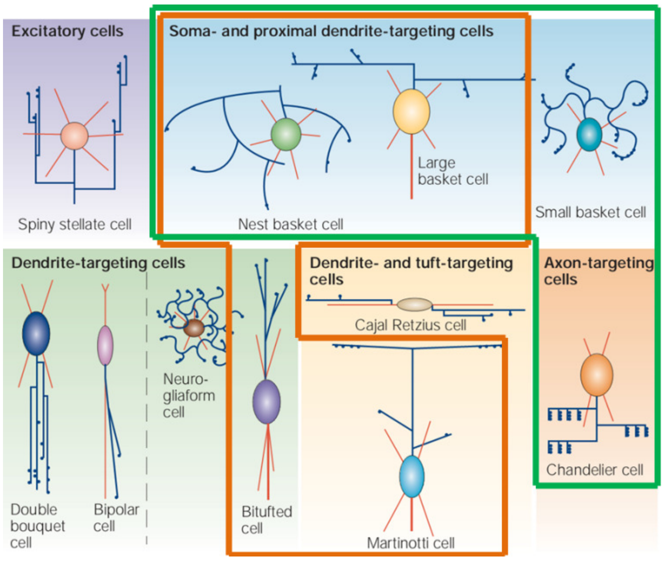

Fig. 1. Neocortical interneuron morphological, molecular and functional diversity. SOM$^+$ and PV$^+$ cell types are demarcated by orange and green lines, respectively. Adapted from Markram et al., 2004.

Neurons have defined morphologies and molecular profiles, which can be used to assign neurons to discrete and non-overlapping classes (Fig. 2).

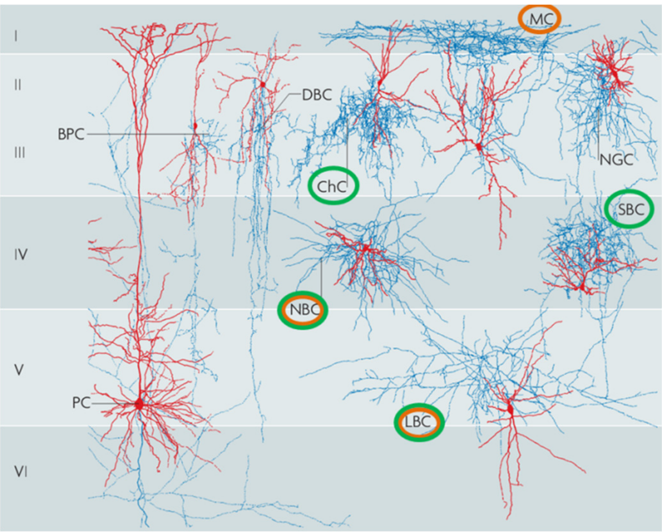

Fig. 2. Neocortical neurons show cell-type-specific morphologies. SOM$^+$ and PV$^+$ cell types have their names demarcated by orange and green ellipses, respectively. Adapted from Huang et al., 2007.

A relevant question is how the physiological, morphological, molecular and synaptic characteristics of neurons relate to each other; particularly, whether the relationships between these features can be exploited to map one set of attributes onto another set of attributes and, thus, to allow the automatic recognition of cell types based on a limited set of features. One pertinent example of this is the prediction of cell morphology and molecular profile based on electrophysiological signals.

One of the most critical aspects in building such an automated predictive system is to choose relevant features to employ in the classification of the signals. It is of especial interest to use features that can be systematically extracted from signals, preferably those for which a mathematical description is available and that, accordingly, are prone to be considered in models of neural networks.

A simple model that has long been used to describe the static electrophysiological behaviour of neurons, namely the

---

*Corresponding author. E-mail: tiago.felix@bcf.uni-freiburg.de

voltage response of neurons (V-V_0) to current injection, is the leaky integrate-and-fire model (Lapicque, 1907, cited by Abbott, 1999) which describes the neuron in terms of an equivalent electrical circuit (Eq. (1) and Fig. 3A) with a capacitance C and a resistance R (corresponding, respectively, to the capacitance and resistance of the cell membrane) whose voltage V (corresponding to the membrane potential) passively changes in response to the injection of a current I, from a resting value V_0 until it reaches a given threshold value V_θ (greater than V_0) and is instantly 'reset' to V_0 (Fig. 3B). This reset is the result of a simplification of the effect of an action potential and is followed by a refractory period t_{ref} during which no current can elicit a change in voltage.

$$C\dot{V} = -\frac{1}{R}(V - V_0) + I \tag{1}$$

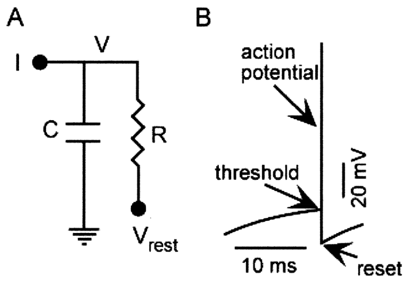

Fig. 3. Leaky integrate-and-fire model. (A) Equivalent circuit with membrane capacitance C and membrane resistance R. V is the membrane potential, V_{rest} is the resting membrane potential, and I is the injected current. (B) Model's simplification of the voltage response of a neuron to a current step. From Abbott, 1999.

For a step current injection, the following equation can be deduced from Eq. (1) to describe the firing frequency f of the neuron:

$$f(I) = \begin{cases} 0 & \text{for } I \le I_{rh} \\ 1\Big/\left[t_{ref} + \tau \ln\left(\dfrac{I}{I - I_{rh}}\right)\right] & \text{for } I > I_{rh} \end{cases} \tag{2}$$

Where τ is the membrane time constant (Eq. (3)) and I_{rh} is the rheobase current (Eq. (4)), i.e. the lower bound of the subset of currents that bring the membrane potential from V_0 to V_θ, which is related with V_θ by the following equation:

$$\tau = R \times C \tag{3}$$

$$I_{rh} = \frac{(V_\theta - V_0)}{R} \tag{4}$$

2. Methods

I performed whole-cell current-clamp recordings of 24 SOM$^+$ and PV$^+$ interneurons in acute slices of the auditory cortex of two recombinant reporter lines of mice expressing the enhanced green fluorescent protein in either SOM$^+$ or PV$^+$ cells. The current injection protocol consisted of 18 evenly spaced and increasing current steps from -100 to 750 pA.

During recording, cells were filled with biocytin and their morphologies were subsequently analysed. Taking into account the morphological and molecular description of neurons and the criteria provided by Huang et al. (2007), Markram et al. (2004) and PING (2008) the recorded interneurons were grouped into six different categories: SOM$^+$ Martinotti cells (MC), SOM$^+$ or PV$^+$ large basket cells (LBC), SOM$^+$ or PV$^+$ nest basket cells (NBC) and PV$^+$ small basket cells (SBC).

The values of the three parameters in Eq. (2), I_{rh}, τ and t_{ref}, were computed for every cell by fitting a trend line to the data points. The fitting was carried out using Eq. (2) as the template equation and the Solver add-in from Microsoft Excel as the iterative equation solver (Fig. 4).

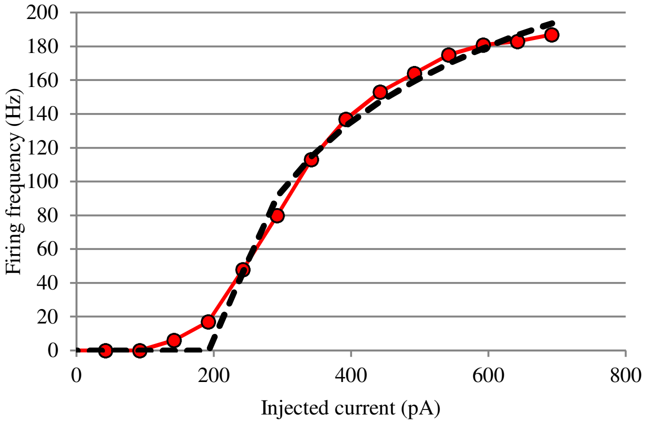

Fig. 4. Firing frequency of a layer-V Martinotti cell during step-current injection (dotted line in red). Trend line fitted to the data points using the leaky integrate-and-fire model (dashed line in black).

2.1. Cluster analysis

Using I_{rh}, τ and t_{ref} as features, I determined the hierarchical clusters of the recorded cells using MATLAB's function 'linkage' and choosing the unweighted average distance as the algorithm for computing the distance between clusters and the standardized Euclidean distance as the distance metric.

2.2. Classification

Six classification tasks were designed, each of them considering a different number of classes and, concomitantly, different assortments of cells (Table 1). For each classification task, several classification subtasks were equally considered according to all the possible combinations of the features I_{rh}, τ and t_{ref}.

Table 1
Classes considered in each of the different classification tasks performed.

Classification task description	Cell-type classes considered
2 class (SOM$^+$ vs. PV$^+$)	SOM$^+$ cells, PV$^+$ cells
2 class (MC vs. BC)	MC, BC
3 class (MC vs. BC-SOM$^+$ BC-PV$^+$)	MC, BC-SOM$^+$, BC-PV$^+$
4 class (LBC/NBC)	MC, LBC/NBC-SOM$^+$, LBC/NBC-PV$^+$, SBC-PV$^+$
4 class (SOM$^+$/PV$^+$)	MC, LBC, NBC, SBC
6 class (all types)	MC, LBC-SOM$^+$, NBC-SOM$^+$, LBC-PV$^+$, NBC-PV$^+$, SBC

Linear discriminant analysis (LDA) was used as the classification method. For this purpose, MATLAB's function 'classify' was used and a linear discriminant function was chosen, i.e. a multivariate normal density was fitted to each group, with a pooled estimate of covariance. Classification results were computed in terms of accuracies (Eq. (5)) and to take into account the different number of classes and random levels across classification tasks, accuracy factors were defined according to Eq. (6). Additionally, confusion matrices were computed to check for class biases.

$$accuracy = \frac{number\ of\ correct\ predictions}{total\ number\ of\ predictions} \tag{5}$$

$$accuracy\ factor = \frac{accuracy}{random\ level} \tag{6}$$

3. Results

3.1. Cluster analysis

One of most conspicuous results of the cluster analysis performed (Fig. 5) is that SOM$^+$ and PV$^+$ cells seem to lie almost exclusively (with the exception of a three cells) in two separate clusters. Likewise, within the cluster of PV$^+$ cells, there is a considerably separate assortment of cell types through different subclusters. As to the arrangement of cells within the cluster of SOM$^+$ cells, the number of non-MC is too low to draw any meaningful conclusion.

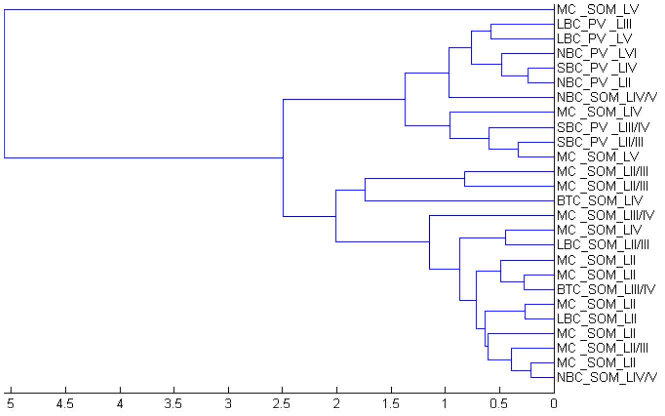

Fig. 5. Dendrogram, depicting the hierarchical clustering of all cells of the available dataset, obtained using I_{rh}, τ and t_{ref} as features.

3.2. Classification

Classification performance in different combinations of features in the two-class classification task of SOM$^+$ vs. PV$^+$ cells shows exceptionally high accuracies, greater than 90% in most cases (Fig. 6). Importantly, no bias towards one of the classes in noticeable in the confusion matrix (Table 2).

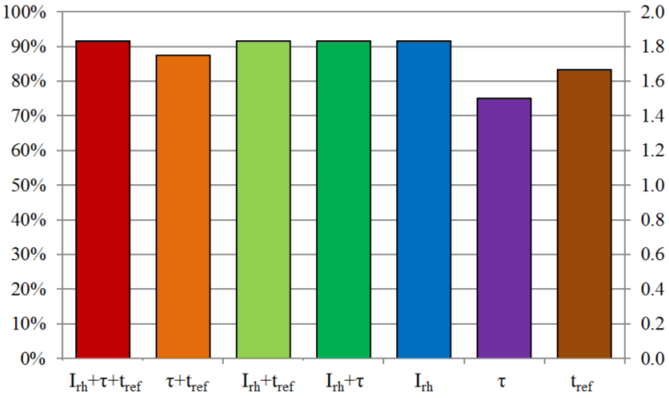

Fig. 6. Classification accuracy (left axis) and accuracy factor (right axis) for different combinations of features in the two-class classification task of SOM$^+$ vs. PV$^+$ cells. Colour codes are preserved throughout the rest of this work.

Table 2
Confusion matrix obtained using I_{rh}, τ and t_{ref} as features for the two-class classification task of SOM$^+$ vs. PV$^+$ cells.

		Prediction	
		SOM$^+$	PV$^+$
Actual	SOM$^+$	16	1
	PV$^+$	1	6

Contrary to the previously discussed classification task, the one comprising six classes led to considerably low accuracies, lower than 50% in every case and as low as 13% in one of the cases (Fig. 7). Nonetheless, accuracy factors indicate significant predictive abilities, as in most cases the accuracy is at least 1.5 times greater than the random level. Similarly, to the previous classification task, no important bias towards one of the classes is found in the confusion matrix (Table 3).

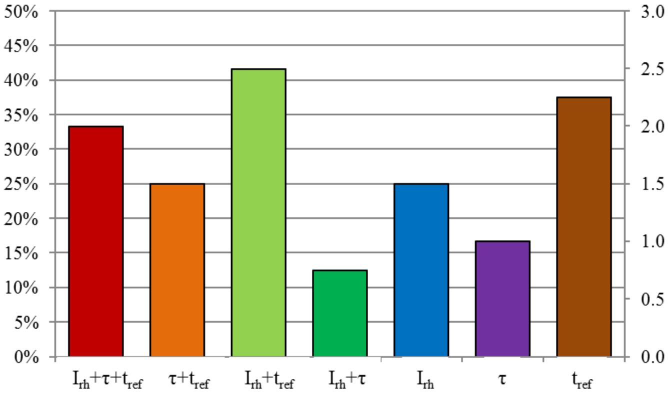

Fig. 7. Classification accuracy (left axis) and accuracy factor (right axis) for different combinations of features in the six-class classification task of all cell types.

Table 3
Confusion matrix obtained using I_{rh}, τ and t_{ref} as features for the six-class classification task of all cell types.

		Prediction					
		MC-SOM$^+$	LBC-SOM$^+$	NBC-SOM$^+$	NBC-PV$^+$	LBC-PV$^+$	SBC-PV$^+$
Actual	MC-SOM$^+$	4	6	3	0	0	0
	LBC-SOM$^+$	2	0	0	0	0	0
	NBC-SOM$^+$	1	0	0	1	0	0
	NBC-PV$^+$	0	0	0	1	0	1
	LBC-PV$^+$	0	0	0	0	2	0
	SBC-PV$^+$	0	0	1	1	0	1

Remarkably, classification performance across the different classification tasks when using I_{rh}, τ and t_{ref} as features (Fig. 8) was identical to that obtained using either I_{rh} and t_{ref} (not shown) or I_{rh} (Fig. 9) as features.

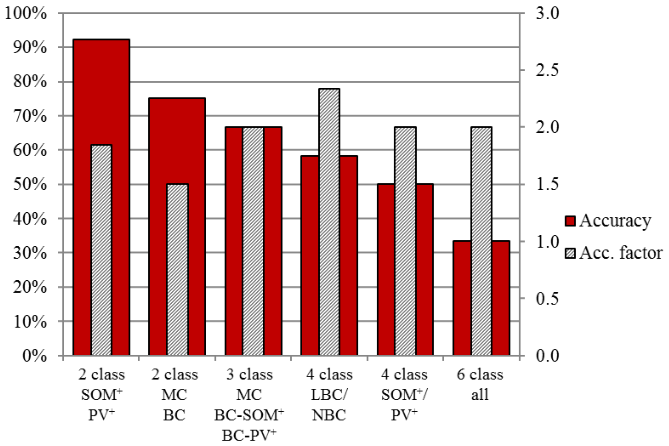

Fig. 8. Classification accuracy (left axis) and accuracy factor (right axis) obtained using I_{rh}, τ and t_{ref} as features for different classification tasks.

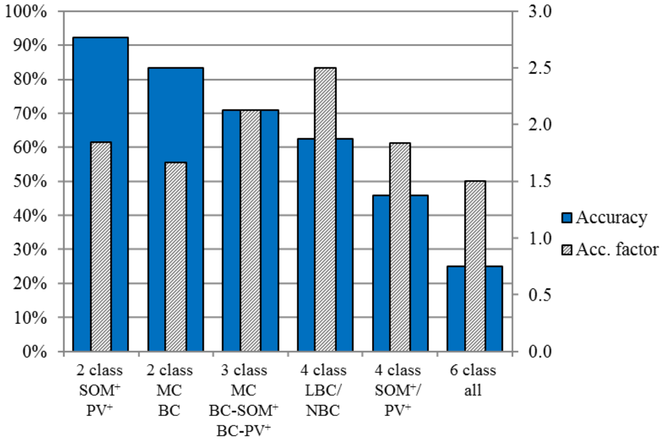

Fig. 9. Classification accuracy (left axis) and accuracy factor (right axis) obtained using I_{rh} as the only feature for different classification tasks.

4. Discussion

The parameters found in Eq. (2) seem to carry relevant information about the morphology, molecular profile and even location of cells. This fact is supported not only by exploratory cluster analysis but also by significantly high predictive abilities obtained in several classification tasks.

Once comparing the classification performance between classification tasks, two remarks are worth mentioning. First, classification performances are much more heterogeneous (across different combinations of features) in tasks with a higher number of classes. This can be easily understood in the light of the fact that the broader the considered groups of cells are the more conspicuous are the differences between cells of different groups; therefore, the easier it is to find differences for any given feature. That is exactly the principle behind cluster analysis.

Secondly, I_{rh} is a very relevant feature as combinations of features that include it usually lead to the best classification performances. Strikingly, even when it is used alone as a feature it yields good classification performances.

At this point, one should mention that the reported performances might have been strongly prejudiced by the small size of the dataset available.

5. Conclusions and future work

Cell morphology, molecular profile and location seem to have a strong implication in electrophysiological behaviour. This relation may be exploited by a device that would allow of the automatic recognition of morphological, molecular and anatomical interneuron types relying solely on electrophysiological signals. This study could pave the way to new and more flexible approaches that would make neurophysiological experiments less dependent upon molecular markers and shorten the process of interneuron identification. Nevertheless, further research should be dedicated to improving classification performance, particularly, to optimizing the classification procedure here described in larger training sets of data.

References

Abbott, L. F. (1999). Lapicque's introduction of the integrate-and-fire model neuron (1907). *Brain Res Bull, 50*(5/6), pp. 303–304.

Huang, Z. J., Cristo, G. D., & Ango, F. (2007). Development of GABA innervation in the cerebral and cerebellar cortices. *Nat Rev Neurosci, 8*, pp. 673–686.

Lapicque, L. (1907). Recherches quantitatives sur l'excitation électrique des nerfs traitée comme une polarization. *J Physiol Pathol Gen, 9*, pp. 620–635.

Markram, H., Toledo-Rodriguez, M., Wang, Y., Gupta, A., Silberberg, G., & Wu, C. (2004). Interneurons of the neocortical inhibitory system. *Nat Rev Neurosci, 5*, pp. 793–807.

PING. (2008). Petilla terminology: nomenclature of features of GABAergic interneurons of the cerebral cortex. *Nat Rev Neurosci, 9*(7), pp. 557–568.

Résumé détaillé

Les interneurones inhibiteurs du néocortex constituent une population cellulaire extrêmement hétérogène caractérisée par une variété de propriétés morphologiques, électriques et moléculaires. Malgré leur petit nombre par rapport aux neurones excitateurs glutamatergiques, qui eux constituent 80% des neurones corticaux, les interneurones inhibiteurs ont un intérêt majeur de part leur diversité, leur fréquence de décharge élevée, et la grande facilitation synaptique décrite à leurs terminaisons. La complexe arborisation axonale des interneurones leur permet de cibler de façon spécifique certaines régions de leurs neurones postsynaptiques. En particulier, les interneurones qui ciblent la région périsomatique des neurones principaux contrôlent avec grande précision la genèse de potentiels d'action ('output') par ceux-ci. La protéine parvalbumine (PV), qui lie le calcium intracellulaire dans la plupart de ce type d'interneurones, est souvent utilisée comme marqueur des interneurones qui inhibent les régions périsynaptiques (perisoma-inhibiting interneurons, PII). Malgré le fait que certaines catégories de PII ne sont pas positives à la PV (PV^+), les cellules PV^+ sont des cellules inhibitrices périsomatiques, et constitue de ce fait un bon modèle d'étude de l'inhibition périsomatique. Les cellules PV^+ sont formées par les cellules en panier et les cellules en chandelier dans le cortex, où elles ciblent respectivement les dendrites proximales et le corps cellulaire, ou les axones des cellules principales.

Le rôle des cellules PV^+ dans le cortex auditif reste encore peu exploré. Je me suis proposé de répondre à deux questions majeures sur leur contribution à l'activité du cortex auditif. J'ai tout d'abord exploré la contribution des cellules PV^+ dans la genèse de rythmes à haute fréquence. J'ai ensuite évalué leur contribution au traitement sensoriel et à l'apprentissage.

Dans la première partie, j'ai examiné la contribution des cellules de type PII à la genèse de certains rythmes du cerveau, tout particulièrement aux oscillations à haute fréquence entre 30 et 80 Hz, les oscillations gamma. Il a été suggéré que ces oscillations qui émergent dans de nombreuses aires du cerveau sont un signal de référence permettant le codage temporel, le liage de différentes informations sensorielles en un seul percept ('sensory binding'), ainsi que les processus de mise en mémoire d'information et leur utilisation ultérieure. Dans le cortex auditif, les altérations des oscillations de type gamma constituent une caractéristique de maladies mentales telle que la schizophrénie. Toutefois la contribution précise des cellules PV^+ dans la genèse des oscillations gamma dans le cortex auditif reste inconnue. Le cortex auditif constitue un excellent modèle d'étude de part la facilité de le stimuler et de par la vaste connaissance de sa neuroanatomie fonctionnelle. J'ai testé le rôle des cellules PV^+ dans l'émergence des rythmes rapides et dans la synchronisation des populations de cellules principales.

Les données recueillies dans le corps de ce travail ont été obtenues grâce à l'aide de souris génétiquement modifiées PV-Cre dont le cortex auditif a été infecté de façon bilatérale par des virus rAAV Cre-recombinants. Cette manipulation a permis d'exprimer de façon spécifique la pompe à ions chlore activable par la lumière, l'halorhodopsine (eNpHR-EYFP) dans les cellules exprimant la PV. Dans ces mêmes souris, une optrode a été implantée dans l'hémisphère gauche, et une fibre optique dans l'hémisphère droit. L'optrode permet de délivrer la stimulation optique pour inhiber spécifiquement les cellules PV$^+$ tout en enregistrant le potentiel de champ local ('local field potential', LFP). La fibre optique éclaire quant à elle l'autre hémisphère. Les expériences ont été menées à terme dans une chambre de conditionnement opérant placée dans une deuxième chambre accoustiquement isolée semi-anechoïque. Les animaux étaient exposés à des stimuli acoustiques de type 'free-field' à large bande avec une densité spectrale uniforme (5-80 kHz) permettant d'activer efficacement le cortex auditif.

Les cellules PV$^+$ ont été inhibées par de la lumière verte qui excite efficacement l'halorhodopsine (à une longueur d'onde 561 nm), augmentant l'amplitude des rythmes gamma induits par la stimulation auditive. Deux contrôles optiques ont été réalisés. Premièrement, nous avons délivré une lumière bleue de longueur d'onde 473 nm qui ne sera, elle, absorbée que légèrement par l'halorhodopsine, et qui en conséquence n'affectera que résiduellement les cellules PV$^+$. Deuxièmement, une nouvelle série d'animaux a été infectée par un virus induisant l'expression de la protéine verte fluorescente EGFP dans les cellules PV$^+$. Ces deux contrôles suggèrent que l'augmentation de gamma était spécifiquement due à l'inactivation des cellules PV$^+$. Nos résultats sont surprenants, puisqu'ils montrent que l'inhibition des cellules PV$^+$, contrairement à l'opinion communément acceptée, peuvent augmentent les rythmes gamma.

Pour confirmer un effet local de la manipulation des cellules PV$^+$ du cortex auditif, nous avons d'abord analysé le potentiel négatif évoqué qui apparaît 15 ms après la présentation d'un son, censé refléter l'excitation de cette région par des fibres en provenance du thalamus et du cortex. Lors de la présentation du stimulus auditif, l'inhibition des cellules PV$^+$ du cortex par la lumière provoque une augmentation de l'amplitude du potentiel N15. Ceci suggère que la population locale enregistrée est dans un état d'excitation plus important après la manipulation spécifique du cortex. Afin d'éliminer la possibilité que l'inhibition des cellules PV$^+$ induit une surexcitation corticale qui permettrait d'amplifier une activité à des fréquences gamma en provenance d'une autre région, j'ai enregistré la synchronie des amplitudes à des fréquences gamma entre le cortex auditif et son noyau présynaptique thalamique, le corps médial géniculé (MGB). La synchronie de l'amplitude de gamma dans le thalamus et dans le cortex auditif reste inchangée lors de l'inhibition des cellules PV$^+$, excluant un rôle du gamma thalamique dans l'augmentation de gamma dans le cortex, suggérant que l'augmentation de l'amplitude de gamma est d'origine corticale.

Dans une deuxième partie, nous avons cherché à définir le rôle des cellules de type PII dans la représentation de stimuli acoustiques et dans leurs conséquences comportementales. A cette fin, nous avons réalisé des expériences de conditionnement à la peur ('fear conditioning') afin d'établir la contribution des PIIs aux réponses corticales et dans le comportement. Ce paradigme consiste à induire une association entre un stimulus non-conditionné (dans ce cas un choc électrique dans le pied) et un stimulus conditionné (dans ce cas un son qui arrive avant ou pendant le choc). La peur du choc électrique, mesurée par l'absence de mouvement, est le paramètre utilisé pour suivre l'apprentissage de l'association, tandis que le potentiel de champ permet de mesurer les fréquences gamma en réponse à la présentation du son après apprentissage. Cet apprentissage a été comparé dans deux conditions pour chaque souris : éclairage bilatéral par la lumière verte ou par la lumière bleue, dans les deux cortex auditifs. Nous avons pris la précaution d'alterner l'ordre de présentation de ces deux longueurs d'onde dans la population de souris afin d'éviter un biais dans l'ordre de présentation du stimulus. Nous avons observé une réduction de l'induction de la peur en réponse à la présentation du son dans le cas où les cellules PV^+ étaient inhibées pendant l'association du son et du choc électrique. Ce résultat constitue à ma connaissance la première démonstration expérimentale d'un effet de l'inhibition de cellules PV^+ dans le cortex auditif pendant l'apprentissage.

En conclusion, cette thèse contribue à comprendre le rôle des cellules PV^+ dans le traitement sensoriel. Une originalité de cette étude consiste à inhiber, et non pas exciter les cellules PV^+, afin de montrer leur contribution négative à la rythmogénèse et positive dans l'apprentissage au niveau du cortex auditif.

UNIVERSITÉ DE STRASBOURG

École Doctorale
des Sciences de la Vie
et de la Santé
STRASBOURG

Tiago Manuel ROCHA FELIX

Inhibition Périsomatique dans les Oscillations Gamma et dans l'Apprentissage Auditif

Résumé

Des preuves convergentes ont attribué aux interneurones de l'inhibition périsomatique (IIPs) un rôle clé dans la production des oscillations gamma (OG). J'ai sondé optogénétiquement l'effet de l'inhibition périsomatique réduite sur les OG et l'apprentissage associatif dans le cortex auditif des souris se comportant librement. Contrairement aux expectatives, je n'ai pas observé une réduction des OG pendant l'inhibition des IIPs, mais plutôt une forte augmentation de l'amplitude dans les OG. L'amplification du potentiel évoqué auditif (PEA) N15, ainsi que l'absence d'une augmentation de la synchronisation entre le cortex et le thalamus, suggèrent que la diminution de l'inhibition périsomatique désinhibe le cortex auditif et favorise la génération intracorticale des OG. Dans une autre expérience, j'ai montré que l'inhibition des IIPs a détérioré l'apprentissage et a produit une réduction liée à l'expérience dans le PEA N15. Enfin, j'ai trouvé que l'abaissement de l'inhibition optogénétique livré à IIP et le réapprentissage des souris ont renforcé les OG auditivement induites.

Mots clés: Parvalbumine, ondes gamma, apprentissage, cortex auditif

Résumé en anglais

Convergent evidence has attributed to perisoma-inhibiting interneurons (PIIs) a key role in the generation of gamma oscillations (GO). I optogenetically probed the effect of reduced perisomatic inhibition on GO and associative learning in the auditory cortex of freely behaving mice. Contrary to expectations, I did not observe a reduction in GO during inhibition of PIIs, but rather a strong increase in the amplitude of GO. The amplification of the auditory-evoked potential (AEP) N15, together with the absence of an increase in synchrony between the cortex and the thalamus, suggest that decreased perisomatic inhibition disinhibits the auditory cortex and promotes the intracortical generation of GO. In a different experiment, I showed that inhibition of PIIs impaired learning and produced an experience-related reduction in the AEP N15. Lastly, I found that lowering the optogenetic inhibition delivered to PIIs and retraining mice enhanced auditory-induced GO.

Keywords: Parvalbumin, gamma wave, learning, auditory cortex